Manipulation of Domain Walls in Anti-perovskite Ferrimagnetic Nitrides

Sambit Ghosh

筑波大学
University of Tsukuba

Université Grenoble Alpes

THÈSE

Pour obtenir le grade de

DOCTEUR DE L'UNIVERSITE GRENOBLE ALPES

préparée dans le cadre d'une cotutelle entre l'*Université Grenoble Alpes* et *University of Tsukuba*

Spécialité : **Nanophysique**

Arrêté ministériel : le 6 janvier 2018 – 25 mai 2016

Présentée par

Sambit GHOSH

Thèse dirigée par **Jean-philippe Attané** et **Laurent Vila**
codirigée par **Takashi Suemasu**

préparée au sein des **Laboratoire Spintronic et Technologie des Composants (SPINTEC)** et **Environmentally Friendly Materials in the Next Generations Lab (University of Tsukuba)**

dans **les Écoles Doctorales de Physique** et **Department of Nano-science and Nanotechnology**

Manipulation of Domain Walls in Anti-perovskite Ferrimagnetic Nitrides

Thèse soutenue publiquement le **4th July 2022,**
devant le jury composé de :

Madame Liliana BUDA-PREJBEANU
Professeur, Université Grenoble Alpes, Président de jury.
Monsieur Yoshichika OTANI
Professeur, Institute of Solid State Phyiscs, University of Tokyo, Rapporteur.
Monsieur Stéphane MANGIN
Professeur, Université de Lorraine, Nancy, Rapporteur.
Monsieur Seiji MITANI
Professeur, National Institute of Material Science, Tsukuba, Examinateur.
Monsieur Hideto YANAGIHARA
Professeur, University of Tsukuba, Examinateur.
Madame Stefania PIZZINI
Directeur de Recherche, Institut Néel, CNRS, Examinateur

Table of Contents

List of Figures

Introduction

> Why cannot we write the entire 24 volumes of the Encyclopedia Brittanica on the head of a pin?
>
> *There's Plenty of Room at the Bottom (1959)*
> *Richard P. Feynman*

Modern electronics has grown rapidly in the last 5 decades, due to the downscaling of CMOS technological nodes to small dimensions, towards 3 nm and beyond[1]. Until now, this downscaling roughly followed Moore's Law, which states that the density of transistors doubles every 18 to 24 months[2]. However, further scaling is reaching physical limits, in particular because of an increase of power leakage as the devices size shrinks[3]. The information and telecommunications industry based on electronics could consume up to $1/5^{\text{th}}$ of the world total energy production by 2025[4]. To lower this power consumption, it is in particular necessary to develop non-volatile devices, without static energy consumption[5].

Spintronics

In this context, Spintronics is an expanding scientific and technological field, which does not only make use of the charge but also of the electron spin. The birth of spintronics is usually considered to be the pioneering work done by Albert Fert and Peter Grünberg on Giant Magnetoresistance (GMR), for which they were jointly awarded the Nobel prize in Physics in 2007[6, 7]. GMR is observed when two magnetic layers are sandwiched between a non magnetic layer. In this case, the total resistance of the stack depends on the relative magnetization directions of the two magnetic layers. The resistance difference between the parallel and anti-parallel states is large. The GMR value can for instance reach up to 40% in Co/Cu multilayers[8]. It was later shown that even higher magnetoresistances could be obtained, up to 1800% at 4K[9] and 604% at room temperature[10], by replacing the non magnetic layer by an insulating layer. This type of magnetoresistance, originally discovered by Jullière in 1975[11], is called Tunneling Magnetoresistance (TMR)[12, 13]. The TMR mechanism involves electrons moving through an insulating barrier between magnetic layers, resulting in a dependance the resistance on the orientation of the magnetization orientations of the electrodes. Beyond the fundamental interest associated to the discovery of spin transport phenomena, this finding allowed the development of new generations of GMR and TMR read-heads for magnetic hard disks drives (HDD), thus enabling to increase the data storage density from 2000 bits/sq.in. (IBM 350 RAMAC disk, 1956) to 1 Terabits/sq.in. (Seagate, 2012)[14, 15]. Spintronics has thus already delivered large scale commercial applications.

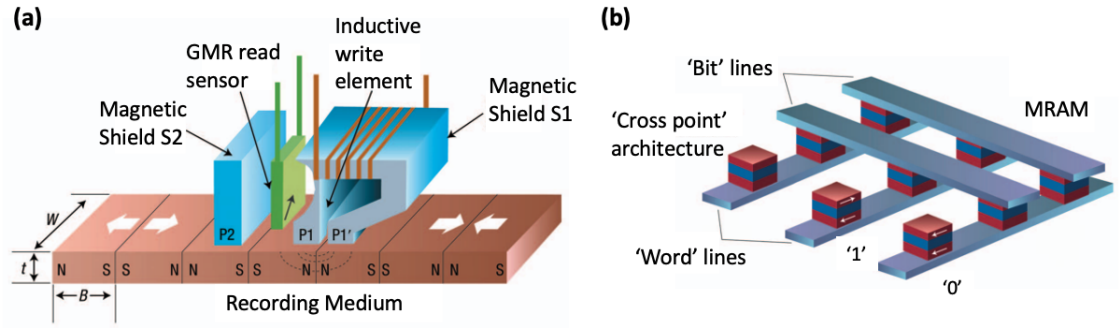

Figure 1: *(a) GMR head for hard disk, consisting of a writing element followed by the GMR read sensor. (b) Principle of the magnetic random access memory in the basic cross point architecture. Taken from Ref[16]*

Spintronics gave birth to several potential memory and logic applications, ranging from Magnetic Random Access Memories (MRAM)[17], Domain wall MRAMs[18], Domain Wall Logic[19–21], to MESO[22] and FESO[23]. Among these concepts, MRAMs have become a commercial memory product[24], while GMR and nowadays TMR are being used for memory and sensor applications[17, 25]. For microelectronics, the advantage of spintronics over the CMOS technology is the non-volatility, i.e., the data retention without any power consumption. Indeed, the data can be stored almost indefinitely within the magnetization states of nanomagnets. Hence, spintronics could lead to the next generation of low power, ultra-fast and high density nanoelectronic devices.

Domain Wall Motion

Ferromagnetic and ferrimagnetic materials are composed of different regions of homogeneous magnetization, called magnetic domains. The boundary between these domains are called magnetic Domain Walls (DWs). A way to manipulate the magnetization of spintronics nanoelements is to control the motion of these DWs.

For instance, in magnetic thin films in which the magnetization is perpendicular to the film plane, the magnetization within the DWs rotates by 180° from on side of the DW to another[26–28]. Such magnetic textures are very interesting features of magnetic materials, as they can be moved with the help of magnetic fields[29–31] and/or currents[32–34]. Current-induced DW motion by spin transfer torque was predicted theoretically by Berger in 1978[35]. It has since been a major focus in spintronics, in particular during the last two decades, for the development of applications such as racetrack memories[36, 37], DW Magnetic Random Access Memories[18] and DW based logic devices[19–21, 38]. While one of the major goals of MRAM is at the moment to replace DRAM thanks to its low-power, high speed and non-volatility[17], the development of racetrack memories might lead to possible replacement candidates for HDDs, while DW based logic could constitute a possible replacement of traditional transistors for logic functions.

Spin transfer Torques (STT)[39, 40] and Spin Orbit Torques (SOT)[41] are the two mechanisms for current-induced DW motion. In the case of the STT acting on a DW, the charge current gets spin polarized by the local magnetization through the s-d interaction[39, 42]. This incoming spin-polarized current then transfers its angular momentum onto the local magnetic moments of the DW, thus leading to the DW motion[40, 43]. On the other hand, SOTs require a heavy metal layer adjacent to the ferromagnetic layer, to generate a spin polarized current by spin-hall effect[44–46] and by Rashba effect[47, 48]. The spin current generated in the heavy

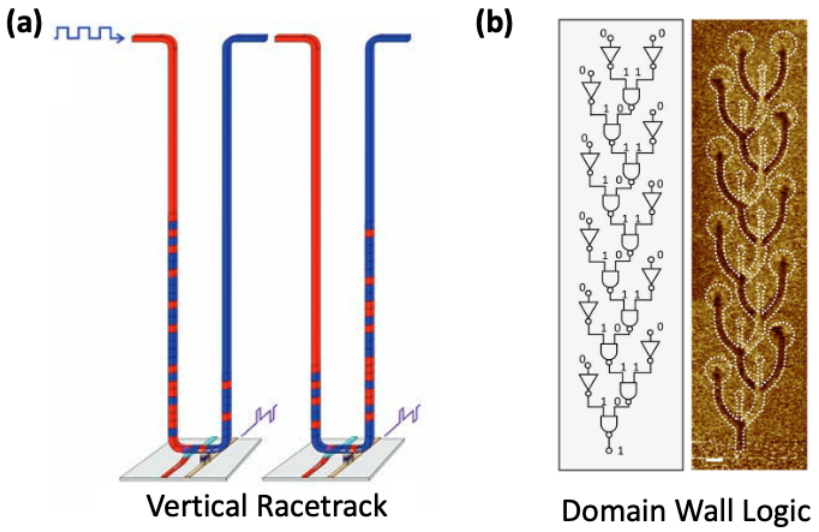

Figure 2: *(a) Concept of the Racetrack memory where the information is coded onto magnetic domains[36] (b) Domain Wall based logic circuit showing cascading with 10 NAND and 11 NOT gates[38]*

metal accumulates and diffuses into the ferromagnetic layer, resulting in the generation of spin orbit torques to drive the DW motion[49–53].

Ferrimagnetic Domain Wall Motion

Although DW motion has been mainly studied in ferromagnetic materials, there has been recently a growing interest towards ferrimagnetic materials for DW motion. A ferrimagnetic material is made up of two sub-lattices with magnetic moments pointing in opposite directions, one of the sublattice possessing a higher magnetization than the other one. This results to a net magnetization which is significantly lower than that of ferromagnets. As the sub-lattices of a ferrimagnet is made up of different elements or atoms, a lower net angular momentum is also present here. The lower magnetization and the angular momentum are key factors to improve the DW velocity. Indeed, the STTs and SOTs become more efficient as they act on a smaller magnetization[40, 43].

In some ferrimagnetic materials, the magnetization and the angular momentum can be controlled and reduced to points where the magnetic moment and/or the angular momentum of the two sub-lattice fully compensate each other, either by changing the temperature of the sample or by tailoring the composition of the material[54]. These points are called the Magnetic Compensation Point (MCP) and the Angular Momentum Compensation Point (ACP)[55, 56]. Such compensated ferrimagnets are very interesting to study as they represent an intermediate case between anti-ferromagnets and ferromagnets. They can be used to study the spin dynamics and transport in anti-ferromagnetically coupled systems which is of interest of Antiferromagnetic spintronics[57]. Indeed, such ferrimagnets offer a significant advantage over anti-ferromagnets, as ferrimagnets have a finite Zeeman coupling which allow them to be more easily manipulated by magnetic fields, like spin textures such as DWs and skyrmions. It also has in principle a finite spin polarization which enables the polarization and detection of spin currents which are crucial for the study of spin dynamics.

Recent works have shown that at the ACP the precessional torque is negligible, resulting in very large DW velocities[58–60] and very fast and efficient magnetization switching[61, 62].

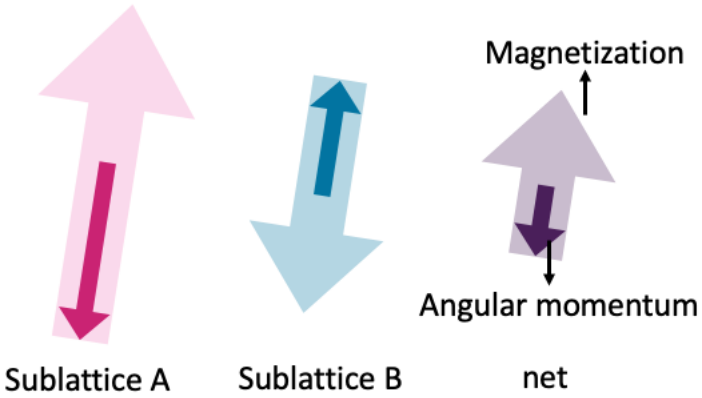

Figure 3: *Schematic illustration of magnetization and angular momentum. The light red (blue) arrow represents the magnetization and dark red (blue) represents the angular momentum of sub-lattice A(B). The light and dark purple arrows represents the net magnetization and angular momentum*

Most experiments up to now have been done using SOTs, which have dominated the scientific activity concerning DWs during the last decade [50, 52], as efficiency of STT were found quite disappointing. Recent experiments relies on rare-earth-based ferrimagnets, such as GdCo [58, 59], TbCo[63, 64], TmYIG[65] and BiYIG[66]. However, the current densities necessary for DW propagation remain high in these systems, or require the assistance of an external in-plane field for DW propagation. Some of these materials are insulating ferrimagnets which complexify the electrical readout. Also, the use of rare-earth materials is both costly from an ecological point of view, and critical from a geo-strategic point of view [67].

In this thesis, I chose to focus on DW manipulation in Rare-earth free ferrimagnetic nitride thin films, an alternative to the present class of Rare-earth based ferrimagnetic materials more widely studied in spintronics. This thesis is divided into five chapters. Chapter 1 is an introduction to ferrimagnetic materials and to the fundamental concepts related to current induced DW motion. Among the rare-earth free ferrimagnetic nitrides, we chose to start with Mn_4N, which is made up of cheap and abundant elements. In chapter 2 we will present the growth and characterization of Mn_4N on MgO and $SrTiO_3$ substrates, which will highlight the unique properties of these materials. It will be followed by the study of current-induced DW motion in Mn_4N. Chapter 3 concerns the growth and characterization of $Mn_{4-x}Ni_xN$ and $Mn_{4-x}Co_xN$. The substitution of Co and Ni leads to the compensation points in the Mn_4N thin films. Chapters 4 focuses on the current driven DW dynamics in these $Mn_{4-x}Ni_xN$ thin films. Lastly, we will examine spin orbit coupling (SOC)-related phenomena in Mn_4N. Chapter 5 features some preliminary works, on SOT switching in Mn_4N and on DW based logic devices.

Chapter

1 Ferrimagnetic materials for Spintronics

In this chapter, we will review the basics of ferrimagnetic materials and nanomagnetism[27, 68–70] which are relevant to the experimental results presented in this thesis. Section 1.1 focuses on ferrimagnetic materials. In section 1.2 we will discuss about different types of magnetic anisotropy in a magnetic material. Section 1.3 we will review the micromagnetic energies in a magnetic system followed by section 1.4 in which we will touch upon look into spin polarization. Lastly, we will discuss the magnetization dynamics in section 1.5.

1.1 Ferrimagnetic Materials

Ferrimagnets are a type of magnetic materials which manifests ferromagnetism and anti-ferromagnetism simultaneously. These materials have two or more sub-lattices which individually behaves ferromagnetically. However, the interaction between these sub-lattices makes them favour an anti-parallel magnetic alignment. This unbalanced anti-parallel magnetic alignment leads to a small net magnetization[71]. Due to their low damping, ferrimagnetic garnets have been used for spin wave[72] and ferrites for microwave applications[73]. Ferrimagnets have been mainly used for for their low magnetization and treated as smaller ferromagnets.

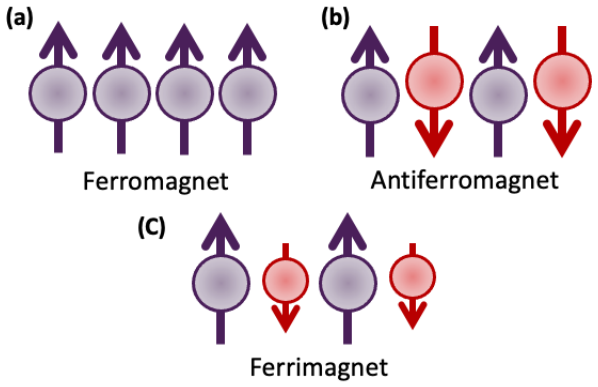

Figure 1.1: *Three types of magnetic alignment. (a) A simple ferromagnet where spins align in the same direction. (b) A simple antiferromagnet with anti-parallel alignment with net zero magnetization (c) Ferrimagnet with anti-parallel alignment with non-zero net magnetization*

1.1.1 Origin of the exchange interaction

Exchange interaction is the interaction between identical particles, in this case neighbouring spins. To understand the origin of the exchange interaction using quantum mechanical considerations, we use a simple two electron system to illustrate the mechanism of the interaction that can take place between the atomic moments and lead to their spacial alignment. We assume that there is no spin orbit coupling or very weak spin orbit coupling and hence the Hamiltonian is spin-independent. As this Hamiltonian is spin independent, the standard quantum mechanical procedure can be used to separate the spacial ψ and the spin χ variables, which is given as:-

$$\Psi(r1, r2, s1, s2) = \psi(r1, r2)\chi(s1, s2) \tag{1.1}$$

The orbital eigen functions are the solutions of the orbital Schrodingers equation.

$$H\psi = -\frac{\hbar}{2m}(\nabla_1^2 + \nabla_2^2) + V(r1, r2)\psi = E\psi \tag{1.2}$$

where, $\hbar$ is the reduced Planck constant, m is the mass of the particle and V is the potential energy respectively. The Hamiltonian being spin-independent leads to the orbital eigenfunctions and the corresponding energy states also being spin independent. However, Pauli's exclusion principle introduces spin dependence into seemingly spin-independent problem in the case of fermions, which in this case is electrons.

For two electrons, the exclusion principle requires the total wavefunction to be anti-symmetric [69]. The wavefunction is divided into two parts, the orbital and the spin parts, which means that if the orbital wavefunction is symmetric then the spin wavefunction must be anti-symmetric. Since spin can have only two possible s_z states, the spin wavefunction is a linear combination of any four two-spin states. Out of the four states, only one is anti-symmetric and has a total spin S = 0. This is known as the singlet state. The other three combinations of the spin states are symmetric and are called triplet states. These states have a total non-zero spin S = 1. Therefore the symmetric spin wavefunctions must be combined with the anti-symmetric wavefunctions for the exclusion principle to be satisfied. Depending on the relative orientation of the two spins of the two particles, the orbital eigenfunctions of our spin-independent Hamiltonian and the associated energies should be different. This is the origin of the exchange interaction - the energy of a system is a function of the mutual orientation of the spins of the two particles. The approximate representation of this effective interaction of the magnetic moments i and j having spins S_i and S_j is given in the following Hamiltonian:

$$\hat{H}^{spin} = -J_{ij}S_i \cdot S_j \tag{1.3}$$

Here, J is the exchange integral or the exchange constant and represents the energy difference between the parallel and the anti-parallel spin states. S_{ij} represents the spin angular momenta of the atoms (or ions) constituting the solid. The effective magnetic field, known as the exchange field, acting on spin i is the sum of the nearest neighbouring terms same as the two particle system.

$$B_E(i) \propto \Sigma J_{ij}S_j \tag{1.4}$$

This interaction is due to the overlap of the neighbouring atomic orbitals and hence it has a very short range and acts as an effective field. This magnetic interaction was first analyzed by Werner Heisenberg and therefore this term and the model is known as the *Heisenberg Hamiltonian* and the *Heisenberg Model* respectively. When the exchange integral is positive for a

given atomic configuration ($J > 0$), the neighbouring spins will tend to align in parallel which leads to a phenomenon called ferromagnetism. When the exchange integral is negative ($J < 0$), the spins will tend to oppose each other and the resulting structure is known as the antiferromagnetic. When the exchange integral is negative and there are two different types of ions in the crystal (for example Fe^{2+} and Fe^{3+} in Fe_3O_4 each having different magnetic moments), the opposing spins do not necessarily cancel each other out as in the anti-ferromagnetic case, but produce a spontaneous moment equal in magnitude to the difference of the two opposing spin sub-lattices. This phenomenon is called ferrimagnetism. Anti-ferromagnetism on the other hand is a case, where the opposing spins are equal in magnitude. This inter-atomic magnetic ordering leads to magnetic substances which are of high significance for many fields of today's technology, including the emerging field of spintronics.

1.1.2 Spin configurations in a Ferrimagnet

The exchange interaction is the cause of magnetic ordering in a solid and this exchange interaction does not necessarily lead to ferromagnetic ordering always as seen above. Moreover, a solid can be composed of different chemical elements which could have different magnetic properties. In principle, adjacent atomic spins of different magnitude can be aligned in different ways to satisfy the local many-spin exchange interactions. Typically such a complex ordering is found in oxides. Here, we will illustrate this phenomenon using a classical ferrimagnet - magnetite.

Fe_3O_4 or $FeO \cdot Fe_2O_3$ is called magnetite which contains two ferric ions, Fe^{3+}, with the spin quantum number s = 5/2 and orbital magnetic moment $L = 0$ and one ferrous ion, Fe^{2+} with s=2. If all of the three moments μ_i were to align, then one would expect a total moment of 14, $\mu = g\mu\Sigma s_i = 2\mu_B(5/2 + 5/2 + 2) = 14\mu_B$, with μ_B the Bohr magneton. However, experimentally it has been found to be $\mu \approx 4\mu_B$. It can be explained if the ferric ions were aligned anti-parallel to the ferrous ion and the total moment is dominated by the ferrous ion. To summarise, in a ferrimagnet there can be two of more sub-lattices with different magnetic strengths which are aligned anti-parallel to each other. In ferrimagnetic oxides, the exchange interaction is mediated by the orbitals of oxygen which is the so called *indirect exchange* or *superexchange* which often leads to the anti-parallel alignment of the spins. The negative exchange integral, $J<0$, represents antiferromagnetic and $J>0$, represents a ferromagnetic coupling. If we assume all the pairwise exchange interactions are, J_{aa}, J_{bb} and $J_{ab} < 0$. The exchange fields acting on the spins in the two sub-lattices are

$$B_a = -\gamma_a M_a - \gamma_{ab} M_b, B_b = -\gamma_b M_b - -\gamma_{ba} M_a \tag{1.5}$$

where all three exchange constants are positive (by reciprocity = $\gamma_{a,b} = \gamma_{b,a}$). The associated total energy is then given by

$$U = -\frac{1}{2}(M_a \cdot B_a + M_b \cdot B_b) = \frac{1}{2}\gamma_a M_b^2 + \frac{1}{2}\gamma_b M_a^2 + \gamma_{ab} M_a \cdot M_b \tag{1.6}$$

Therefore, the energy is minimum for the two sub-lattices when M_a is antiparallel to M_b.

1.1.3 Compensation points

Ferrimagnets like its ferromagnetic counterparts have a Curie temperature where the magnetization originating from the exchange interaction vanishes as a result of strong thermal fluctuations. As the different sub-lattice of a ferrimagnet can be made up of different elements, these sub-lattices could have different temperature evolution of their magnetization. Therefore, in some special cases, the magnetization of sub-lattice can cancel each other with a zero net

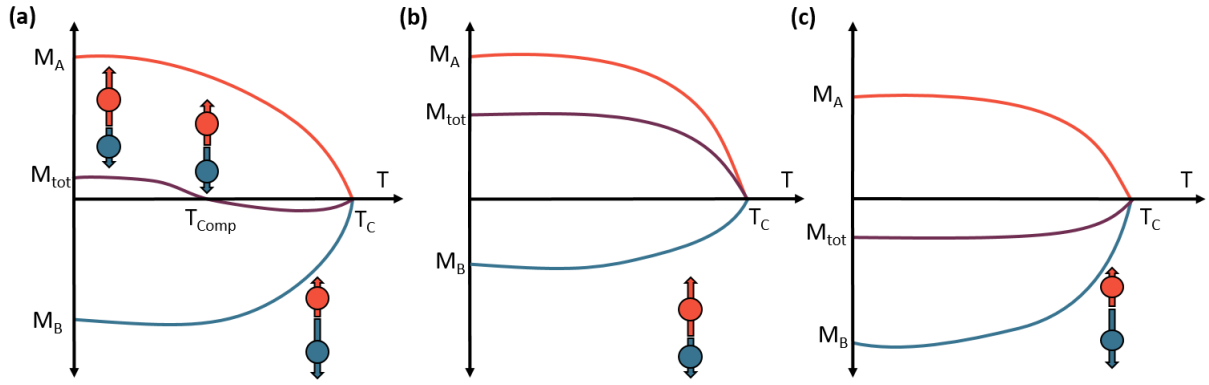

Figure 1.2: *Schematic of three different temperature evolutions of the magnetization on site A and B and of the total magnetization of the ferrimagnet.*

magnetization at a specific temperature. This point before the Curie temperature is known as the compensation temperature. Furthermore, since the gyromagnetic ratios of the sub-lattices are different, there is also a net zero angular momentum temperature. Ferrimagnets can also be manipulated to reach these MCP and ACP by varying the concentration of elements in material at a given temperature as well. Temperature evolution of different types of ferrimagnets have been shown in Fig.1.2 with the red(blue) line showing the magnetization from sub-lattice A(B). The purple lines shows the net magnetization of the ferrimagnets. The magnetization reaches zero before the Curie temperature in Fig.1.2(a) with the magnetization sub-lattice A higher before the MCP and higher magnetization in sub-lattice B after the MCP. The magnetization remains higher in sub-lattice A until the Curie temperature in Fig.1.2 (b) with the net magnetization pointing towards the magnetic moment of sub-lattice A and vice-versa in Fig.1.2 (c). This ability to reach the MCP and ACP makes these special types of ferrimagnets very interesting to study and also useful for spintronics.

1.2 Magnetic Anisotropy

Magnetization in a microscopic ferromagnetic domain usually lie along one easy axis. Due to time reversal symmetry, a certain magnetic distribution M should have the same energy as the state with reversed magnetization along the same axis M(negative direction). This phenomenon is given by the the anisotropy energy Ea which is given by:

$$E_a = Ksin^2\theta \tag{1.7}$$

Where θ is the angle between the direction of M and the easy axis, K is the anisotropy constant. In this context, we shall look into the magnetic state of a ferromagnetic domain. Magnetic anisotropy is at the core of the traditional magnetic memories. Perpendicular magnetic anisotropy(PMA) is an anisotropy where the easy axis of the magnetization lies out of the plane from the thin film.

1.2.1 Crystal Anisotropy

It has been found that the spin in the ferromagnets saturate fully in a certain direction and require a very high external fields to fully saturate in other directions. This happens due to the crystallographic structure of the material, which determines a preferred direction of the magnetization vector out of all directions. When this happens, the material is said to have

magnetic anisotropy. Hence, the anisotropy due to the crystal structure is known as Crystal Anisotropy. The lattice structural anisotropy induces an anisotropy for the magnetization due to the spin-orbit coupling. In the case of the atomic orbitals of spherical symmetry, the orbital angular momentum is zero thus making the spin-orbit coupling to be zero.

$$E_{SO} = \gamma_{SO} L \cdot S = 0 \tag{1.8}$$

In the above case, the electron is free to take any orientation in space. In the case of non-zero L_Z, which means having a non-spherical charge distribution would lead to preferred direction of the orbitals. If the spin magnetic moment is non-zero, it will lead to magnetic anisotropy. In the uniaxial case, the anisotropy energy U_K is at first order:

$$U_K = K(m_x^2 + m_y^2) = K sin^2\theta = -K cos^2\theta + const \tag{1.9}$$

where, θ is the angle made by the magnetization with the z direction. For $K > 0$, the energy of the system is lowered for the magnetization aligned with the z axis. For $K < 0$, the ferromagnet is said to be of *easy plane* type. In the case of ferromagnetic CoFeB, the crystalline anisotropy is very low while in the case of ferrimagnetic Mn_4N thin films, crystal anisotropy is very high.

1.2.2 Shape Anisotropy

A ferromagnetic sample responds to an external magnetic field by getting magnetized much easier along the longer direction than the shorter one. This effect gives rise to shape ansiotropy which is magnetostatic in nature. It can be understood by perceiving that at the sample surface, the magnetic field lines prefer to close up.

$$divB \equiv div(H + 4\pi M) = 0 \tag{1.10}$$

As the M is a finite quantity in the film and zero outside, the divergence is large at the surface if the normal to the surface component of the magnetization is non zero. Magnetic poles are produced due to this divergence, which produces a magnetic field called the *demagnetizing field* H_d.

$$divH = -4\pi divM \tag{1.11}$$

This demagnetizing field acts to oppose the magnetization (hence the name is derived), and is proportional to the strength of the magnetization. It is often expressed through the demagnetizing factor N_d. N_d is a tensor and is function of the geometry of the sample only. N_d is generally represented by a symmetric 3×3 tensor.

In the case of a homogeneous magnetization and taking the system shape of a system as an ellipsoid, the energy of the dipolar interaction can be derived which acts on the magnetization.

$$U_{shape} = -\frac{\mu_0}{2} \cdot M \cdot H_d \tag{1.12}$$

where H_d is given as $-N_d \cdot M$. In the case of ferromagnetic thin films, the demagnetizing energy density is given by:

$$U_{shape} = -\frac{\mu_0}{2} M_s^2 sin^2\theta \tag{1.13}$$

where θ is the angle between z direction and the magnetization. Here, the demagnetizing tensor is a diagonal with only one zero which is equal to 1 along the z direction.

1.2.3 Interfacial Anisotropy

Interfacial anisotropy as the name suggests originates from the interface of the magnetic layer. This form of anisotropy generally provides PMA in the case of CoFeB/MgO system. The main contributors of interfacial ansiotropy are the symmetry breaking of the crystal structure, elastic stress due to lattice distortion and hybridization of the Co(Fe)-3d orbitals with the 0-p_z orbitals[74–76]. Interfacial anisotropy hence, competes with the demagnetizing energy and its contribution is divided by the thickness of the ferromagnetic layer (K_i/t_{FM}). In order to have a stable PMA in ferromagnetic thin films, the interfacial anisotropy has to be higher than the shape anisotropy. Therefore ferromagnetic thin films are made as thin as possible to have PMA.

1.3 Micromagnetic energies and Domain Walls

As seen in the section 1.1.1, the exchange interaction in a ferromagnet or ferrimagnet aligns the spins locally. This makes the material magnetized, however, this macroscopic ferromagnets can also have no net magnetic moment. This state is known as the demagnetized state which was first stated by Weiss as arising from a division of the sample into microscopic regions, or domains which have varying magnetic orientations. It was first described by Landau and Lifshitz[77] in 1935. In order to understand the nature of this phenomenon and length scale involved one must consider the full energy landscape for a given sample case. We will discuss in short about the six different contributions to the total energy. The total energy could be given as:-

$$U = U_{ex} + U_k + U_{me} + U_{ms} + U_i + U_{Zeeman} \tag{1.14}$$

The first term in Eq.1.3 represents the *Exchange* energy which acts to align the neighbouring spins in parallel, with the spin in one direction and for small spin-to-spin rotations. It can be expanded into:-

$$U_{ex} \sim -cos\theta_{ij} \sim \left(\frac{\partial\theta}{\partial x}^2\right) \tag{1.15}$$

The second term comes from the *Magnetocrystalline* anisotropy which acts to align the magnetization along the preferred directions of the material, and in the case of uniaxial anisotropy it is given by:-

$$U_k \sim -cos^2\theta \tag{1.16}$$

The third term is the *Magnetoelastic anisotropy* which affects the magnetization in response to stress present in the material, and in the simplest uniaxial case is given as:

$$U_{me} \sim cos^2\theta \tag{1.17}$$

The fourth term comes from the *Magnetostatic* or *shape* anisotropy which is the interaction of the magnetization with its self-field, or demagnetizing field and it is mainly due to discontinuities in M normal to surfaces or to its volumic charges. It is proportional to M_s^2 and gets minimised when the net magnetization is zero. Hence, this term is the main reason behind the formation of ferromagnetic domains.

$$U_{ms} \sim cos^2\theta \tag{1.18}$$

The fifth term here is *interfacial* anisotropy which has an unidirectional bias from the interface spins. By neglecting energy contributions from canting spins on both sides of the

interface.

$$U_i \sim -cos\theta \tag{1.19}$$

The last term here comes from the *Zeeman* energy which represents the preference of the magnetization to be parallel to an external magnetic field, it given by:-

$$U_{Zeeman} \sim -cos\theta \tag{1.20}$$

Note that θ used in the above mentioned terms is generally different angle for every term except when the anisotropy axes coincides. These qualitative arguments for some limiting cases are used only to illustrate the procedure for finding the microscopic spin distributions. Minimization of the total energy with respect to the magnetization direction (θ) gives the equilibrium spin distribution, which reflects all interactions in the system. Here, we will not attempt to see the non-equilibrium spin distributions and use these arguments to estimate the length scales for the multi-domain states to occur.

Here, we consider a ferromagnet with uniaxial anisotropy where the magnetization vectors of the adjacent domains are anti-parallel to each other. As the magnetization vectors are anti-parallel to each other, there is in fact an a 180° transition from one direction to another. This transition region which separates two domains are called *domain walls*. In the case of strips with PMA, there can be two different kinds of DWs; *Bloch* DWs and *Néel* DWs. Here we will focus more on the Bloch DWs where the spin rotate in the plane parallel to the magnetization inside the domains, it was given in the honour of Bloch who first spoke about this transition[78]. If this transition occurs within one lattice spacing in the material, there would be no increase in the anisotropy energy. However in that case, the change in exchange energy for on spin pair would be

$$\Delta U_{ex} = -2JS^2 cos\theta_{ij} = JS^2 \tag{1.21}$$

In this scenario, if $J = 4\times\ 10^{-21}$ Joules, $\Delta U_{ex}/a^2 \approx 0.25\mathrm{J/m^3}$. In order to minimize this relatively large energy, the rotation has to be shared with a large number of spins with $\theta \approx \pi/N$. Here N is the number of spins in the DW. For a large N, the cosine can be expanded to yield

$$\Delta U_{ex} = -2J^2S^2 cos\theta_{ij} = JS^2\left(\frac{\pi}{N}\right)^2 \tag{1.22}$$

Here, assuming all the N spins are rotated by the same angle, the DW energy density can be hence given by

$$\epsilon_{ex} = H\frac{\Delta U_{ex}}{a^2} = JS^2\frac{\pi}{N}^2 \tag{1.23}$$

where a is the lattice spacing (one spin per lattice unit). It can be clearly seen that the energy is reduced by extending the wall.

The anisotropy energy, on the other hand increases in proportion to N as

$$\epsilon_k \approx NKa \tag{1.24}$$

where $sin^2\theta \approx 1$ is assumed and K is the anistropy energy density (in $\mathrm{J/m^3}$). The combined total exchange and anisotropy energy is then given as

$$\epsilon_{ex} + \epsilon_k \approx JS^2\frac{\pi^2}{Na^2} + NKa \tag{1.25}$$

Minimizing with respect to N yields

$$Na \equiv t_{dw} = \pi\sqrt{\frac{JS^2}{Ka}} = \pi\sqrt{\frac{A}{K}} \tag{1.26}$$

where $A \equiv JS^2/a \approx 10^{-11}$ J/m is the exchange stiffness constant. Hence for a soft ferromagnet with a $K \sim 10^3$ J/m^3 the characteristic DW thickness is $\sim$ 100 nm and for hard ferromagnets, the t_{dw} can be as small as 10 nm.

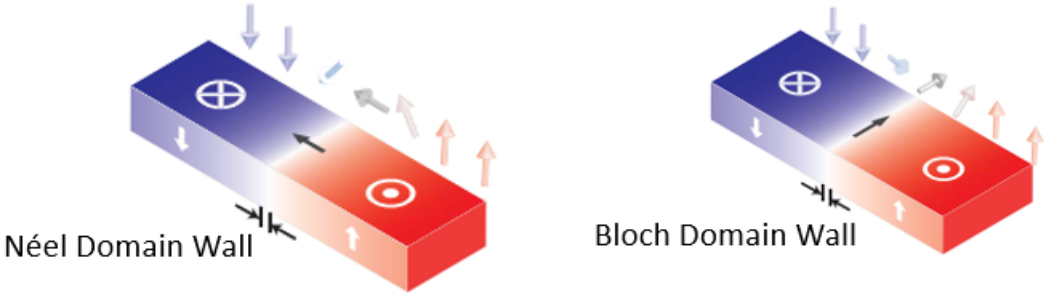

Figure 1.3: *Schematic of the domain wall structures in thin films with PMA (a) Néel domain wall (b) Bloch domain wall. Adapted from [79]*

In the case of thin films, as realized by *Néel* [80], the standard Bloch walls do not hold up if the film thickness becomes comparable to the wall width. Here, the wall has lower energy when the spins of the wall are rotating in the perpendicular plane, using an in-plane rotation instead of the standard Bloch wall. Néel had estimated the transition thickness using a very simple argument where the wall is approximated as an elliptical cylinder of W and height D. The demagnetizing factor for this cylinder with vertical magnetization vector direction is given as $N_{Bloch} = W/(W + D)$. Here, if the W becomes larger than the D, the demagnetising energy increases and hence the wall flips into a Néel wall. The demagnetizing factor for this kind of wall is then given as $N_{Nel} = D/(W + D)$, which is smaller than N_{Bloch} when $W > D$. Hence, in thin films, the DWs are scaled with the exchange length of the stray field $\Delta_d = \sqrt{A/K_d}$ along with the exchange length of the anisotropy energy and the film thickness.

1.4 Spin Polarization

The magnetic effects described until now derives from the complicated band structures of ferromagnetic and ferrimagnetic materials. The band structure of magnetic materials gives rise to its magnetism and spin polarization. When a current flows through a magnetic material, the spins of the flowing electrons (of s character) are aligned to the magnetization due to the exchange interaction between the s orbitals and the d orbitals and interatomic hybridization[70, 81]. This total magnetization depends on the band splitting at the fermi level of the magnetic materials.

In the picture of band theory, the two requirements for spontaneous magnetization are the exchange interaction and the density of states at the Fermi level. A simplified model of a transition metal band is shown in Fig.1.4. Here the Fermi level crosses the d band (3d) in a way that spin up states are fully occupied while the spin down states are only partially filled. The s states (4s) have a negligible splitting in the equilibrium state. This occurs as the exchange splitting not only splits the 3d band but also pushes the spin up state well below the Fermi level. As the d electrons have a higher effective mass, they are considered to be localised and

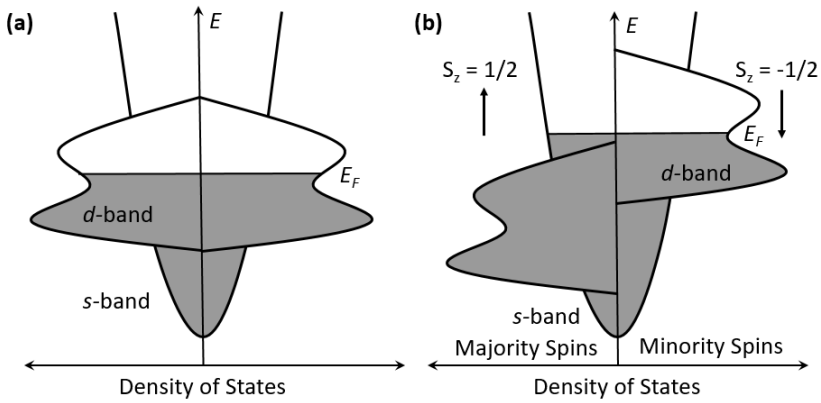

Figure 1.4: *Spin dependence of the density of states for S and d bands in 3d transition metals, for (a) a normal metal and (b) a ferromagnetic metal. S band are quasi parabolic bands, typical of a free electron behaviour, while d bands are more localized at the Fermi level E_F.*

give rise to the spontaneous magnetism while the s electrons having lower effective mass and high mobility are considered to be de-localised, and responsible for carrying the current.

The total magnetization then simply originates from the difference of the spin populations between the up and down states below the Fermi level. The amount of splitting of the d band determines the kind of ferromagnet. Fe has lesser d band splitting than Ni or Co and hence it is considered to be a weak ferromagnet while Ni and Co are strong ferromagnets due to higher d band splitting[70]. The electrical conduction on the other hand depends on the conduction electrons close to the Fermi level E_F. This leads to separate channels for conduction of the two populations of spin states. In the case of ferromagnets, the two populations are unbalanced which leads to conduction mainly through one spin state or the other. From Fig.1.4, as the spin up state is completely filled, conduction occurs through this channel and is considered to be majority carriers whereas the electrons scatter more due to the presence of unfilled state in the spin down state which leads to lower conduction of this spin channel. This unbalanced conduction σ leads to spin polarization which is given as[82]

$$P = \frac{\sigma_\uparrow - \sigma_\downarrow}{\sigma_\uparrow + \sigma_\downarrow} \tag{1.27}$$

where $\sigma_\uparrow$ and $\sigma\downarrow$ are conductivity for spin up and spin down, respectively. The spin polarization for ferromagnetic CoFeB is P=0.65[83] and Fe_4N is P=0.59[84]. For non magnetic materials $P = 0$, whereas for half metallic ferromagnets $P = 1$ where the conduction only takes place purely with one spin state present at the Fermi level[85]. We have also demonstrated a high spin polarization in ferrimagnetic Mn_4N[86] in this thesis which will be discussed later in Chapter 2.

1.5 Magnetization Dynamics

The magnetization dynamics is described by the Landau-Lifshitz Gilbert (LLG) equation which gives the time evolution of the magnetization in a magnetic media[77, 87].

$$\frac{\partial \boldsymbol{m}}{\partial t} = \gamma_0 \boldsymbol{H_{eff}} \times \boldsymbol{m} + \alpha \boldsymbol{m} \times \frac{\partial \boldsymbol{m}}{\partial t} \tag{1.28}$$

Here, $\mathbf{m}$ is the unit vector of the local magnetization(M/M_s), $\gamma_0 = \mu_0\gamma$ where γ is the gyromagnetic ratio, μ_0 is the vacuum permeability and α is the dimensionless damping factor.

H_{eff} is the effective field which includes all the micromagnetic energies and is given by

$$\boldsymbol{H_{eff}} = -\frac{1}{\mu_0 M_s}\frac{\delta E_{total}}{\delta \boldsymbol{m}} \tag{1.29}$$

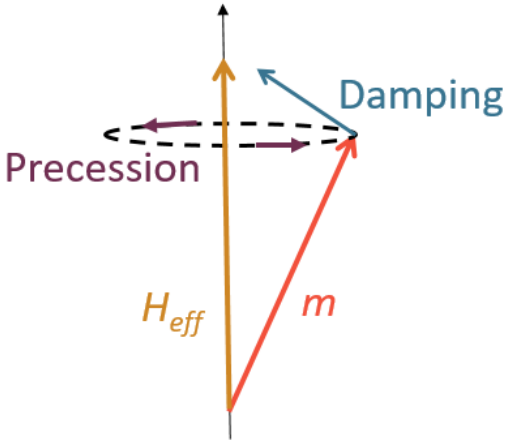

Figure 1.5: *Schematic of the magnetization precession around the effective field.*

The terms in the LLG equation can be considered to be torques when the system is perturbed, meaning when the magnetization and the effective fields are varied. In order to conserve the energy, the first term describes the precession of the magnetization around the effective field. The angular velocity of this precession is proportional to the effective field and the gyromagnetic ratio γ_0. The second represents a torque perpendicular to the precession of the magnetization and forces the magnetization to align with the effective field towards an equilibrium position. This term is dissipative in nature and is proportional to the damping factor α. The LLG equation is extended for modelling the different torques induced by magnetic fields and currents.

1.5.1 Spin Transfer Torques

Berger theoretically predicted that a current induces a drag force to a 180° DW by tilting it[35]. This effect was later explained by Slonczewski[39] as the STT where the exchange interaction between the conduction s electrons and the local d electrons induce an effective field H_{sd}.

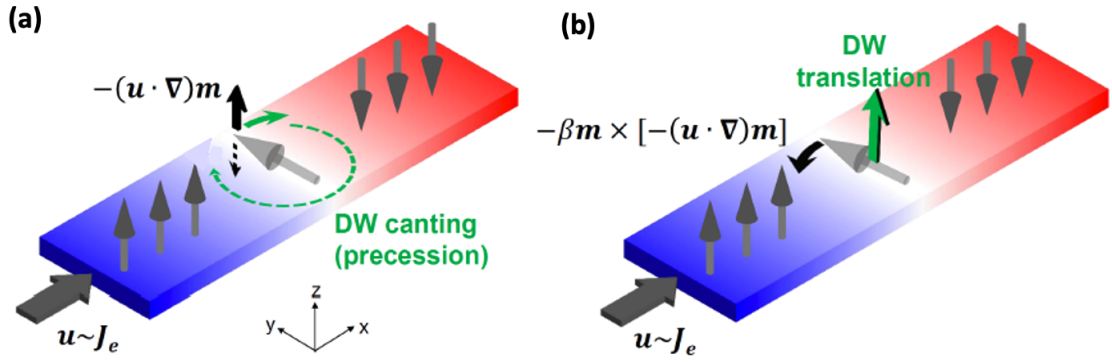

Figure 1.6: *Spin transfer torques on perpendicular anisotropy nanostrips (a) Adiabatic spin transfer torque (b) Non-adiabatic spin transfer torque. Adapted from Ref[88]*

When these electrons move through a magnetic gradient such as a DW, the spin polarization of the conduction electrons becomes misaligned with that of the local magnetic moment. This

misalignment between the local magnetic moment and the spin density causes a torque to the local magnetic moment[40, 43]. The effective field induces two different types of torques; i) the adiabatic torque leading to spin precession around the effective field H_{sd} and a non-adiabatic torque leading to spin relaxation towards the H_{sd} direction. The adiabatic and the non-adiabatic torques are then added into the LLG equation[89, 90] and as per the formalism given by Thiaville et al[40], it is given as

$$\Gamma_{Adiabatic} = -(\mu \cdot \nabla) \cdot \boldsymbol{m} \tag{1.30a}$$

$$\Gamma_{Non-Adiabatic} = \beta \boldsymbol{m} \times (-\mu \cdot \nabla) \cdot \boldsymbol{m} \tag{1.30b}$$

Here β is the non-adiabatic factor and μ is the spin drift velocity which is a vector in the direction of the flow of electron. It is given as

$$\mu = \frac{g\mu_B}{2e} \frac{P}{M_s} \boldsymbol{J} \tag{1.31}$$

with P being the spin polarization, M_s is the saturation magnetization and J is the current density vector.

1.5.2 Spin Orbit Torques

The spin polarization from the magnetic material is responsible for the STT. In the case of SOTs, the spin polarization is generated via a heavy metal layer next to the magnetic layer or through the interface between the heavy metal or an oxide layer and the magnetic layer. Here, the spin current is generated in the heavy metal layer due to the spin Hall effect[44–46] (SHE) and/or at the interface through Rashba-Edelstein[47, 48] effect. These spin polarized current then acts as an effective field and exerts its torques onto the magnetic layer which allows for the motion of the DWs.

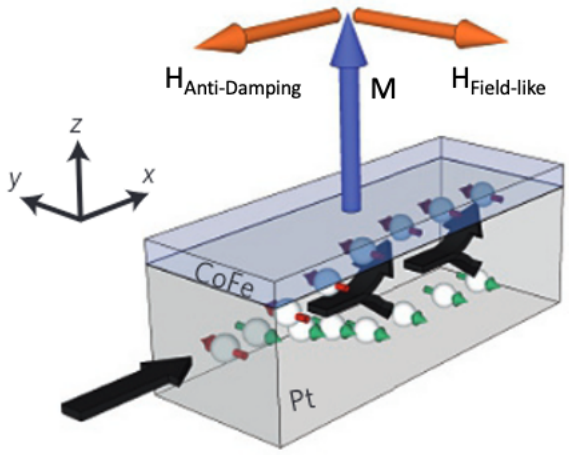

Figure 1.7: *Illustration of the current induced effective fields $H_{Anti-damping}$ and $H_{Field-like}$ acting on the magnetization. Adapted from[52]*

In the case of SHE, a pure charge current is converted into spin current in heavy metals which have a large spin orbit coupling (SOC). This conversion is the result of different relativistic scattering mechanism due to the SOC. In heavy metals such as Pt, W or Ta, the scattering of the electrons is spin dependent which accumulates the electrons with opposite spins at the

opposite edges of the film. The torque generated from the SHE is known as the damping-like torque and has the similar direction as the non adiabatic torque. It can be added into the LLG equation as:

$$\boldsymbol{\Gamma_{ad}} = \gamma_0 \frac{|g|\mu_B}{2e} \frac{\theta_{SHE}}{M_s t} [\boldsymbol{m} \times (\boldsymbol{m} \times \boldsymbol{\sigma})] \tag{1.32}$$

where, t is the thickness of the magnetic material, θ_{SHE} is the spin Hall angle which is the conversion rate of a charge current into a spin current and σ is the polarization direction of the spin current.

Now, moving to the other SOT originating from the Rashba effect which is called field-like torque. It has a similar direction as the adiabatic torque. It is given as

$$\boldsymbol{\Gamma_R} = \gamma_0 \frac{\alpha_R P}{\mu_0 \mu_B M_s e} [\boldsymbol{m} \times \boldsymbol{\sigma}] \tag{1.33}$$

Here, α_R is the Rashba coefficient which is the strength of the Rashba SOC.

1.5.3 Spin Transfer Torque in Ferrimagnets

In the case of materials with multiple sub-lattices, the LLG equation has to be modified considering the magnetic moments and the angular momentum of the different sub-lattices. Here, we shall see how the LLG equation evolves in a two sub-lattice ferrimagnetic system[55, 60, 91]. The magnetic moment of the two sub-lattices will be represented as "1" and "2". Here, we have to also take into account the inter-layer exchange coupling between the sub-lattices J_{ex} whose energy is added to the energy of the effective field of the magnetization H_{eff}[60, 92, 93]. Assuming a strong inter-layer coupling, which means that the magnetic moments of the two sub-lattices m_1 and m_2 are always anti-parallel to each other unless a very high external field of more than a few Tesla is applied, we can have two separate LLG equations for the two sub-lattices which are given as:

$$[LLG_1]\delta_t \vec{m}_1 = -\gamma_{01} \vec{m}_1 \times \vec{H}_1 + \alpha_1 \vec{m}_1 \times \delta_t \vec{m}_1 - (\vec{\mu}_1 \cdot \vec{\nabla}) + \beta_1 \vec{m}_1 \times (\vec{\mu}_1 \cdot \vec{\nabla}) \tag{1.34a}$$

$$[LLG_2]\delta_t \vec{m}_2 = -\gamma_{02} \vec{m}_2 \times \vec{H}_2 + \alpha_2 \vec{m}_2 \times \delta_t \vec{m}_2 - (\vec{\mu}_2 \cdot \vec{\nabla}) + \beta_2 \vec{m}_2 \times (\vec{\mu}_2 \cdot \vec{\nabla}) \tag{1.34b}$$

Here, the $\vec{H}_1$ and $\vec{H}_2$ of the two sub-lattices are similar to Eq.1.29. As we expect a very low disturbance between the magnetic moments of the two sub-lattices due to high inter-layer exchange coupling, we can consider $\vec{m}_1 = \vec{m}_2$. It therefore gives an effective net magnetization of $M_s = M_1$ - M_2. Hence, we can take $m = m_1 = -m_2$ as previously done[60, 91]. By adding the sub-equations in Eq.1.34, we can obtain an LLG equation showing the effective dynamics of the magnetic material.

$$\begin{aligned} \left(\frac{M_1}{\gamma_{01}} - \frac{M_2}{\gamma_{02}}\right) \delta_t \vec{m} = {} & \frac{1}{\mu_0} \vec{m} \times \frac{\delta E}{\delta \vec{m}} + \left(\alpha_1 \frac{M_1}{\gamma_{01}} + \alpha_2 \frac{M_2}{\gamma_{02}}\right) \vec{m} \times \delta_t \vec{m} \\ & - \left(\left(\vec{\mu}_1 \frac{M_1}{\gamma_{01}} - \vec{\mu}_2 \frac{M_2}{\gamma_{02}} \cdot \vec{\nabla}\right) \vec{m}\right) \\ & + \vec{m} \times \left(\left(\beta_1 \vec{\mu}_1 \frac{M_1}{\gamma_{01}} + \beta_2 \vec{\mu}_2 \frac{M_2}{\gamma_{02}}\right) \cdot \vec{\nabla}\right) \vec{m} \end{aligned} \tag{1.35}$$

From Eq.1.35, the effective parameters of the materials could be obtained in order to ease these calculations[94].

$$\begin{aligned}
\vec{H}_{eff} &= -\frac{1}{\mu_0 M_s}\frac{\delta E}{\delta \vec{m}} \\
\gamma_{0eff} &= \frac{M_s}{L_s} \\
a_{eff} &= \frac{L_\alpha}{L_s} \\
\beta_{eff} &= \frac{\beta_1 P_1 + \beta_2 P_2}{P_{eff}} \\
P_{eff} &= P_1 - P_2 \\
\mu_{eff} &= \gamma_{0eff}\frac{\hbar}{2e}\frac{1}{\mu_0 M_s} P_{eff} J
\end{aligned} \tag{1.36}$$

Here, $L_s \equiv \left(\frac{M_1}{\gamma_{01}} - \frac{M_2}{\gamma_{02}}\right)$ is the net angular momentum while $\mathrm{L}_\alpha \equiv \left(\alpha_1\frac{M_1}{\gamma_{01}} + \alpha_2\frac{M_2}{\gamma_{02}}\right)$. Now, we shall rewrite the LLG equation in terms of the angular momentum L_s and taking $L_\alpha \equiv \alpha L_s$:

$$\delta_t \vec{m} = \frac{1}{L_s}(\vec{m} \times \delta_m E + L_\alpha \vec{m} \times \delta_t \vec{m} + \Gamma) \tag{1.37}$$

where, Γ is the STT term. It can then expanded and re-written into:

$$\delta_t \vec{m} = \frac{L_s}{L_s^2 + L_\alpha^2}(\vec{m} \times \delta_m E + \Gamma) + \frac{L_\alpha}{L_s^2 + L_\alpha^2}\vec{m} \times (\vec{m} \times \delta_m E + \Gamma) \tag{1.38}$$

In Eq.1.38, the two components of the dynamics of magnetization are emphasised[60]. Hence using this, the STT term then can be written as:

$$\Gamma_{STT} = -(L_s\mu \cdot \nabla)\vec{m} + \vec{m} \times (\beta L_s\mu \cdot \nabla)\vec{m} \tag{1.39}$$

Where β is the non-adiabatic parameter and $L_s\mu$ is given as:

$$L_s\mu = \frac{P_{eff} J \hbar}{2e} e_J. \tag{1.40}$$

with Je_J is the current density and P_{eff} is the effective spin polarization. Using these equations, the DW velocity in the steady regime can be given as:

$$v = \frac{\beta}{L_\alpha} L_s\mu \tag{1.41}$$

The DW velocity in the precessional regime is given as:

$$v = \frac{L_s + L_\alpha\beta}{L_s^2 + L_\alpha^2} L_s\mu \tag{1.42}$$

According to the above mentioned equations, we can see that α_{eff} diverges close to the angular momentum compensation points which results in an instantaneous alignment of the magnetization to the effective local field[60, 95]. The instantaneous alignment is also the result of the negligible precessional torque applied to the magnetization. The divergence of α_{eff} has

been shown experimentally by ferromagnetic resonance measurement in an all-optical pump and probe technique[55]. In Chapter 4, we will demonstrate how the change of angular momentum and the net magnetization affects the DW velocities in ferrimagnetic $Mn_{4-x}Ni_xN$.

Summary

This chapter has led the foundation for understanding theoretically the following experimental chapters, in particular, the peculiar case of ferrimagnetic materials, the different micromagnetic energy terms involved in defining a magnetic configuration and the different current induced torque. The next chapter focuses on Mn_4N.

Chapter 2

A Brief History of Mn_4N

> If time travel is possible, where are all the tourists from the future?
>
> *Black Holes and Baby Universes and Other Essays (1993)*
> *Stephen Hawking*

In this chapter, we will introduce the magnetic nitrides, and present their main properties and advantages. The first section deals with the classification of the anti-perovskite nitrides. It is then followed by the introduction to the Mn_4N compound in section 2.5, which describes structural and magnetic characterization of Mn_4N samples grown on MgO and $SrTiO_3$ substrates. These results, which have been actually obtained during the PhD work of Dr. Toshiki Gushi, are the basis of my PhD topic. The section 2.6 will focus on the current-induced DW dynamics on Mn_4N grown on $SrTiO_3$ substrate, a study made by Dr. Toshiki Gushi, to which I contributed.

2.1 Nitrides

Nitrides are a class of compounds containing nitrogen with an oxidation state of -3. The nitride ion(N^{3-}) is strongly attracted to metal cations, hence forming metallic nitrides[96]. Nitrides are similar to carbides wherein they come in the category of refractory metals, which have a very high melting point and are chemically stable. This property of nitrides derives from having a high lattice energy, which is the energy required to form a crystal from the gaseous state. It also makes the nitrides very hard materials with cubic Boron Nitride[97], Titanium Nitride[98–100] and Silicon Nitride[101, 102] being used for hard coatings and as cutting materials[99, 100]. Nitride compounds generally have a wide bandgap and are commonly either insulators or semi-conductors. One of the most prominent nitride semi-conductors is GaN, which is used in light emitting diodes to produce blue lights, and which has lead to the Nobel prize in physics in 2014[103]. Nitrides can be formed from a large group of elements from the periodic table. Here, we will look deeper into nitrides formed with transition metals. These compounds have indeed a wide range of properties and applications.

The largest group of nitrides is made using transition metals, which leads to interstitial

nitrides. In such compounds the Nitrogen could either be interstitial, in between the atoms, holes or well placed in the crystal structures. The general formulas for such compounds are given as AN, A_2N or A_4N[1]. Such compounds are generally inert, they have high melting points and are very hard in nature, with a metallic lustre. In these compounds the stability and the properties depend upon the crystal structure and also on the amount of Nitrogen in the system. Transition metals Fe, Co, Mn and Ni forms magnetic nitrides. However, these magnetic nitrides are not very stable, and generally decompose into substitute elements or compounds. One such example is Fe_2N, which decomposes at 200°C[104, 105]. The stability of such nitrides depend on the stoichiometry and the crystal structure. In the next section, we will look into magnetic nitrides having an anti-perovskite crystal structure.

2.2 Ferromagnetic Nitride Family

Let us focus on magnetic nitrides possessing an anti-perovskite crystal structure. A typical anti-perovskite material has a general formula ABX_3, where the A and B are the two anions and X is the cation. In this structure, the cation sits at the body centre of the crystal lattice, the anions being at the corner sites and the face-centered sites. For metallic magnetic nitrides, the chemical formula is M_3AB, with M being either Mn, Ni, Co or Fe, and A being for instance Mn[106, 107], Ni[107, 108], Sn(Tin)[106], Zn(Zinc)[106] or Ga(Galium)[109, 110], among many other elements which could be a part of this crystal structure. Here, B represents the cation which could be either N(Nitrogen) forming nitrides, C(Carbon)[107] forming carbides or B(Boron). It should be noted that bulk Manganese Nitride alloys with Cu (Copper), Zn and Ga[109] have been studied for their high negative thermal expansion, which is due to their non-collinear magnetic structure[111]. In this structure, the face-centered atoms are well coupled to the body centre atom, making it chemically very stable.

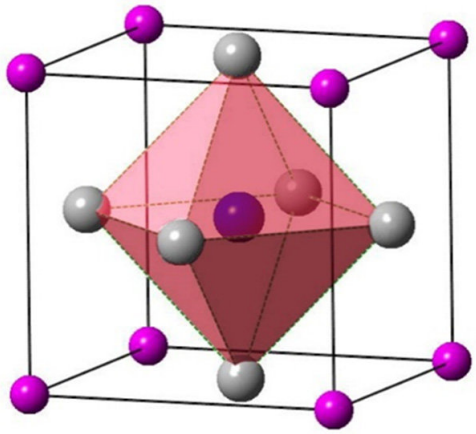

Figure 2.1: *Schematic of the anti-perovskite crystal structure showing the anions at the corner sites and at the face-centered sites, and the cation at the body centre.*

Anti-perovskite magnetic nitrides can either have a single magnetic element (represented as A_4N) as both the anions or alloys with two different elements with different compositions generally represented as $A_{4-x}B_xN$ with A and B representing the two different magnetic elements.

The anti-perovskite magnetic nitride family, which has been previously studied by our group in Tsukuba, mainly consists of Fe_4N[84, 112, 113], Ni_4N[114], Co_4N[115, 116], Mn_4N[117–

[1]A represents a transition metal

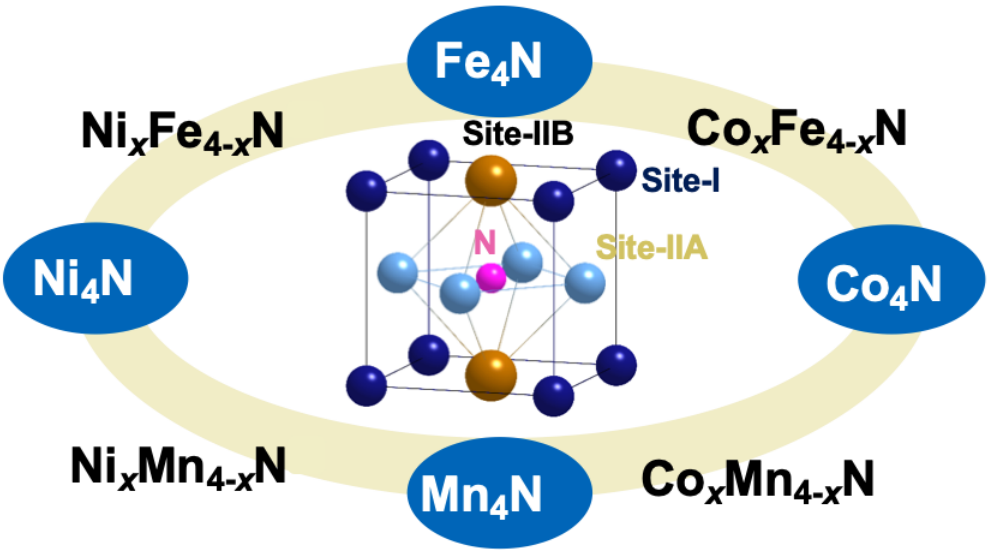

Figure 2.2: *Anti-perovskite magnetic nitride family.*

120] and their alloys[121–124]. Mn_4N is a ferrimagnet, while Ni_4N was found to be paramagnetic[125]. These material family is shown in Fig 2.1. Here, the Fe, Co, Ni and Mn atoms occupy both the corner and the face-centered sites.

We will first discuss the ferromagnetic nitrides in this family. The magnetic moment of the corner and face-centered atoms point in the same direction, thereby making the materials ferromagnetic. The magnetic moment of the corner sites are higher than that of the face-centered sites, as they are more localised. On the contrary the face-centered atoms are well hybridized with the N atom and itinerant in nature. The hybridization between the 2p orbitals of the Nitrogen atom and 3d orbitals of the metal atoms is the source of an electronic transport dominated by the face-centered atoms[113, 126–129]. This anti-perovskite structure with the N atom also enhances the magnetization in such magnetic nitrides. This increase is clearly observed when compared with other nitrides such as Fe_2N[105], FeN[130, 131], Mn_2N[104], and MnN[132], which is anti-ferromagnetic. Overall, the amount of N does not only dictate the crystal structure, but also whether the compound is magnetic or a normal metal, as analysed from the computational data[104]. Also, nitrogen expands the crystal structure in these compounds with respect to similar anti-perovskite carbides[107, 133].

As mentioned earlier, other elements could be substituted in these base compounds to form alloys. At first, we look at the substitution in these base ferromagnetic nitrides with other magnetic elements. Co is substituted in Fe_4N to form $Fe_{4-x}Co_xN$[121]. In this compound, the Co and the Fe atoms occupy randomly corner sites or face-centered sites. The increase of Co leads to a decrease of the net magnetic moment of the system. Similarly to the case of Co substitution, Ni substitution in Fe_4N forms $Fe_{4-x}Ni_xN$, the increase of the Ni concentration leading to a decrease of the saturation magnetization[125]. When Fe is substituted by Mn in Fe_4N, the magnetization decreases as the Mn concentration increases, and eventually a transition from a ferromagnetic to ferrimagnetic[123] material occurs. It was also shown that the spin polarization changes from negative to positive as the Mn concentration is increased[124]. From theoretical calculations it was shown that among Mn, Ni and Co; Mn occupies preferentially the Fe II site, while Ni and Co are rather found in the Fe I site[134]. Recently, we have demonstrated that the substitution of Mn atoms in ferrimagnetic Mn_4N by Indium leads to a ferrimagnetic to ferromagnetic transition in $Mn_{4-x}In_xN$ at room temperature[135].

2.3 Ferrimagnetic Nitrides

Anti-perovskite based ferrimagnetic nitrides basically comes from the anti-ferromagnetic coupling of the magnetic moments between the sub-lattices shown in Fig.2.3. In the case of Mn_4N, the corner sites and the face-centered sites are occupied by Mn atoms, with N at the centre. Using this as the base system, other ferrimagnetic alloys can be derived. Substitution of Mn with Ni, Co and Fe results in the formation of $Mn_{4-x}Ni_xN$[119, 129, 136], $Mn_{4-x}Co_xN$[137, 138], $Mn_xFe_{4-x}N$[123, 124] and $Mn_{4-x}In_xN$[135]. Using these substitutions and by finely tuning the concentration of the substituent, it is possible to reach the magnetic and angular momentum compensation points at room temperature. This ability to reach the compensation points has been demonstrated using $Mn_{4-x}Ni_xN$ and $Mn_{4-x}Co_xN$, which will be discussed in more depth in chapters 3 and 4.

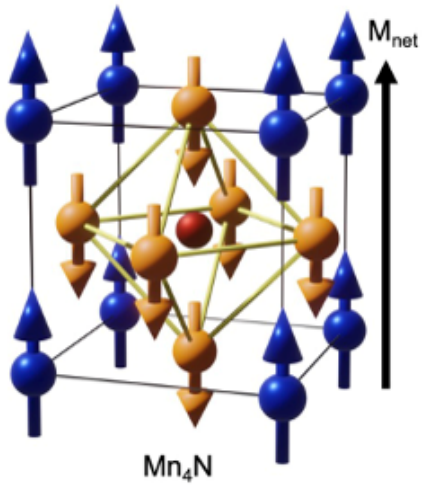

Figure 2.3: *Anti-ferromagnetic structure of Mn_4N, with blue atoms corresponding to Mn site I corner atoms, orange atoms to the Mn site II face-centered atoms, and the red atom to the Nitrogen atom in the centre. The arrows represent the magnetic moment, where Mn I and Mn II atoms are anti-ferromagnetically coupled.*

2.4 Paramagnetic and Anti-ferromagnetic Nitrides

Mn_3NiN is a non-collinear anti-ferromagnetic material with an anti-perovskite crystal structure[139]. In this system, the Ni atoms are occupying the corner sites, while the face-centered sites are occupied by the Mn atoms. This system shows a transition from paramagnetism to anti-ferromagnetism below 260 K[139, 140]. A perfectly cubic crystal structure of Mn_3NiN is antiferromagnetic, however a compressive stress or tensile strain allows this system to have some magnetic moment[141]. Even though this system is ternary, it is often compared to and has similar properties to non-collinear anti-ferromagnetic metallic binary alloys, such as Mn_3Sn[142], Mn_3Pt[143] and Mn_3Si[142]. A giant piezomagnetism has also been demonstrated in Mn_3NiN[144].

Ni_4N is an interesting material in this class of compounds, as there are different reports showing it to be either ferromagnetic or paramagnetic. Ni_4N has two different phases, the Ni_4N-I phase which is magnetic, and the Ni_4N-II phase which is non-magnetic[145]. The existence of such phases have also been confirmed by theoretical calculations[146]. Ni_4N grown

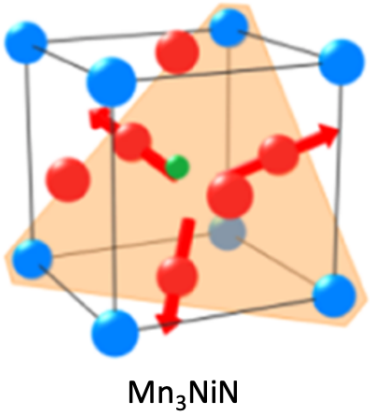

Figure 2.4: *Anti-ferromagnetic cubic Mn_3NiN. The blue atoms are Nickel atoms, the red are Mn atoms and the green are Nitrogen atom. Taken from Boldrin et al.[144]*

epitaxially by our group in Tsukuba has been shown to be paramagnetic[125]. It has however been shown previously that Ni_4N is ferromagnetic at room temperature[147]. Using polar neutron reflectometry it was confirmed in a recent study that Ni_4N is indeed paramagnetic at room temperature and becomes ferromagnetic around 15 K[148]. The presence of two different magnetic phases in Ni_4N particularly depends on the growth parameters and conditions. Mn_3CuN is a material with similar properties. Cu fills the corner sites, the Mn atoms being at the face-centered sites. This material has been shown to have a giant magnetostriction at low temperatures[149, 150] along with having a ferromagnetic transition below 143 K[107, 151]. It has also been predicted to have an anti-ferromagnetic spin ordering.

2.5 Mn_4N

Mn_4N is a metallic ferrimagnet with an anti-perovskite crystal structure, as shown in Fig. 2.3. The two different sub-lattices are anti-ferromagnetically coupled in this system[106, 108, 152]. The magnetic study of Mn_4N was first performed by Guillard and Wyart *et al* in 1946, Wiener and Berger in 1955 [153], Juza *et al*[154] in 1957 , Takei *et al*[152] in 1960 followed by Mekata[106] in 1962 using polarized neutron diffraction. The Mn corner atoms have a magnetic moment of 3.85 μ_B and the Mn face-centered atoms have a very low magnetic moment of -0.9 μ_B[106, 108, 152]. The low magnetic moment of the Mn face-centered atoms are due to their hybridization with the N atom located at the centre. Taking the magnetic moments into account, it was later showed by Fruchart *et al*[108] using group theory that Mn_4N could have three different non-collinear magnetic ordering, two anti-ferromagnetic and one ferrimagnetic mode as shown in Fig. 2.5. Bulk samples of Mn_4N have (111) magnetic anisotropy [108, 152, 155–158], where the crystal structure is cubic. However, in the case of thin films the magnetic orientation changes from (111) to (001), because of the appearance of a perpendicular magnetic anisotropy (PMA)[117, 118, 120, 159–162]. This PMA is the result of the in-plane tensile stress acting on the crystal structure, which changes from a cubic to a tetragonal phase[117, 120]. In a recent study, the correlation between the amount of N and in-plane tensile strain was demonstrated[163]. The PMA in Mn_4N thin films thus simply originates from the crystalline anisotropy.

In these studies, the growth of Mn_4N has been done by diffusing the elements in a solid phase, using grinding and annealing methods which resulted in a powder form of the material[106, 152]. From the 1990s, films of Mn_4N have been grown using several different methods such as

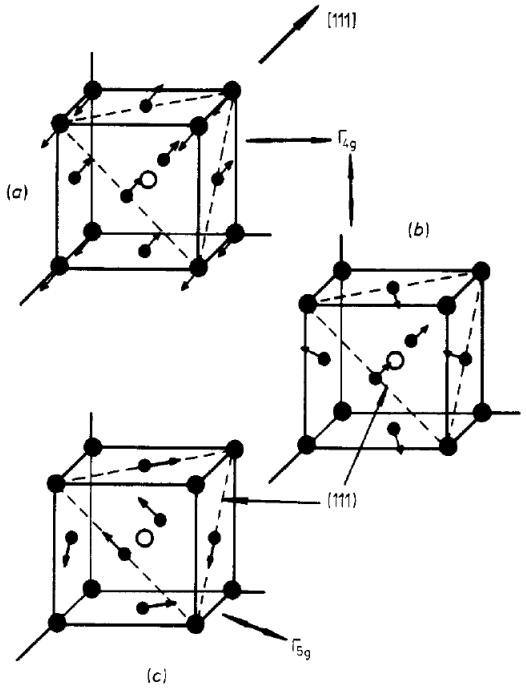

Figure 2.5: *Schematic showing the three different magnetic ordering obtained in Mn_4N from group theory (a) ferrimagnetic mode, (b) and (c) pure Anti-ferromagnetic modes (Taken from Fruchart et al [108])*

dc reactive sputtering[158–161, 163, 164], rf sputtering[165], pulsed lased deposition[166] and MBE[117, 118, 156, 167], on a range of different substrates such as glass[164, 168], MgO[117, 120, 158, 161, 163, 169, 170], $SrTiO_3$(001)[117, 118, 120], $LaAlO_3$ LAO (100)[120], $(LaAlO_3)_{0.3}$ $(Sr_2TaAlO_6)_{0.7}$ LSAT (001)[171], Si[159, 160], SiC[156, 169], GaN[156, 169] and Sapphire[169]. Mn_4N is very stable thermally, with a relatively high Curie temperature around 740K [108, 157].

The saturation magnetization of Mn_4N varies somewhat from 50 kA/m to 200 kA/m, depending on the method of growth, growth parameters, thicknesses and type of substrate used. In general, the value of the magnetization of Mn_4N in a thin film of 10 - 30 nm is around 80-100 kA/m at room temperature[118, 123, 155, 161]. The perpendicular anisotropy values are similar in most of the samples, with a high value of 1.1×10^5 J/m^3 [117, 118, 122]. The anisotropy field and the coercive field varies with different growth mechanisms. The anisotropy field is typically higher than 2.5 T and have been seen to be upto 4 T which comes from the quality of thin films and the coercive field ranges from 0.15 - 0.6 T[117, 118, 122] which depends on the external defects and pinning sites of the thin films.

From the band structure calculations, the electronic properties of Mn_4N were first calculated by Matar *et al*[126], which shed light on its metallic behaviour more thoroughly and demonstrated that the transport occurs through Mn II face-centered atoms[126, 127, 129]. Mn_4N has a high resistivity, around 180 µΩcm at room temperature[118]. A drastic decrease in resistivity has also been observed in Mn_4N with the decrease in the temperature[172, 173]. A high residual resistivity ratio (RRR) of 11 has been obtained in Mn_4N. This value is comparable to that of anti-ferromagnetic Mn_3Sn RRR = 15[174], highligthing an important role of the phonons in these compounds. Mn_4N has also a negative Anomalous Hall angle of around -2% [117, 118, 167, 172, 173]. In the next section, we will focus on the growth and characterization of Mn_4N thin films by molecular beam epitaxy (MBE) on MgO and $SrTiO_3$ substrates.

2.5.1 Growth of Mn_4N on $MgO/SrTiO_3$ Substrates

In this part we will show a comparison between 10 nm thick Mn_4N grown by MBE either on MgO(001) or on $SrTiO_3$(001) substrates. With the help of structural characterizations, magneto-transport measurements, vibrating sample magnetometer (VSM) and magnetic imaging techniques, we will highlight the influence of the substrate on the magnetic properties.

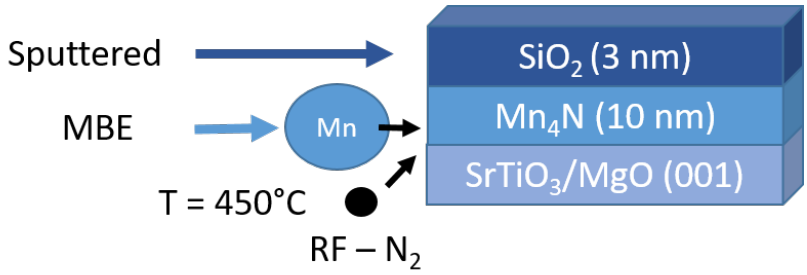

Figure 2.6: *Sketch of the MBE growth of Mn_4N on MgO and $SrTiO_3$ (001) oriented substrates, at 450°C, in a RF N_2 environment, with the sputtering of SiO_2 as capping layer to prevent oxidation*

10 nm thick Mn_4N layers were deposited on MgO and $SrTiO_3$ (001)-oriented substrates at 450°C. The MBE growth chamber used for the deposition is equipped with an ion-pump (10^{-7} Pa), with a Mn Knudsen cell and in presence a radio-frequency (RF) N_2 plasma. In order to prevent oxidation of the thin films, a 3 nm layer of SiO_2 was deposited by sputtering of a SiO_2 target by Ar plasma.

2.5.2 Structural Characterization

20 keV reflection high-energy electron diffraction (RHEED) and X-ray diffraction (XRD) with Cu Kα radiation were used to characterize the crystalline quality of the grown Mn_4N layers. The RHEED was performed in-situ, in the growth chamber, after the deposition of the Mn_4N, while the XRD was performed ex-situ after the deposition of the capping layer.

The results of the XRD characterization are presented in Fig. 2.7. Fig. 2.7 (a) and (b) show the out-of-plane (ω - 2Θ) and (c) and (e) show the in-plane XRD and RHEED patterns, as inset, for deposits on the MgO and $SrTiO_3$ substrates, respectively. XRD peaks of Mn_4N 002 on MgO are well separated and can be easily distinguished in both out-of-plane and in-plane plots. On the other hand, XRD peak of Mn_4N 004 is used to extract the structural information and quality, as the $SrTiO_3$ peaks are very close to the Mn_4N 002 peaks for this substrate. ω - scan rocking curves are shown in Fig.2.7 (e) Mn_4N 002 on MgO and (f) Mn_4N 004 on $SrTiO_3$. Both the Mn_4N 002 on MgO and 004 on $SrTiO_3$ have a very good Lorentzian shapes. The width of these curves differ, indicating a better structural quality of $Mn_4N/SrTiO_3$, with a narrower rocking curve than for Mn_4N/MgO. Importantly the rocking curve of the $Mn_4N/SrTiO_3$ shows a remarkable value of 0.14 degree at FWHM. Similar rocking curves have been observed for thin films of Fe_4N[122]. Streaky RHEED patterns were observed, which is a common aspect on these c oriented Mn_4N 001 and 002 thin films[175]. The 00n peaks in the XRD pattern in addition to the super-lattice RHEED reflections (alternating brighter and darker lines) demonstrate a good long-range ordering and the presence of N atom at the body centre of the fcc-Mn lattice.

Hence, the XRD and RHEED patterns confirm an epitaxial growth of the thin films. The a and c lattice constants were also extracted from the in-plane and the out-of-plane XRD measurements, respectively. Using the lattice constants, the lattice mismatch is given by Eq. 2.1 is calculated for both the Mn_4N/MgO and $Mn_4N/SrTiO_3$. The lattice misfit percentage for

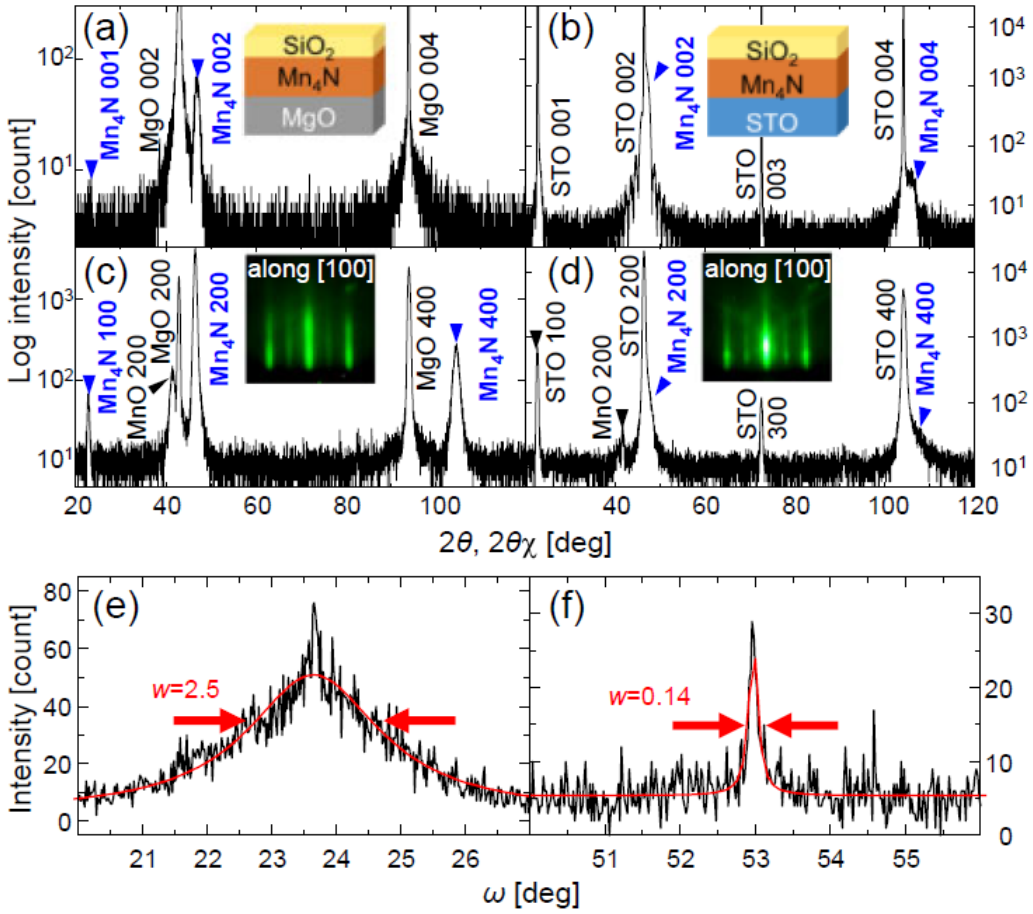

Figure 2.7: *XRD patterns of Mn_4N/MgO (a,c,e) and $Mn_4N/SrTiO_3$ (b,d,f) thin films . (a, b) show the out-of-plane XRD patterns. The blue arrows point to the peaks indicative of (001) oriented Mn_4N. Inset: thin film stack. (c, d) shows the in-plane XRD patterns. The incidence angle for this measurement was set at $\omega = 0.4°$, with the scattering vector along [100]. The insets show the RHEED images taken along the [100] direction of each substrate. (e, f) shows the ω-scan rocking curves for Mn_4n 002 on MgO and Mn_4N 004 on $SrTiO_3$ substrates. The black curve represents the raw data while the red curve shows the Lorentzian fitting.*

MgO is -7.6%, while that of $SrTiO_3$ is -0.4%. This clearly shows that the lattice constant of Mn_4N matches and relaxes very well with the $SrTiO_3$ substrate.

$$f = (a_{film} - a_{sub})/a_{sub} \tag{2.1}$$

Additional X-ray Reflectometry (XRR) measurements were also performed on these samples. From the fitting of the XRR data, the accurate thickness values of these magnetic thin films were extracted, with 8.4 nm for Mn_4N/MgO and 9.4 nm for $Mn_4N/SrTiO_3$ sample.

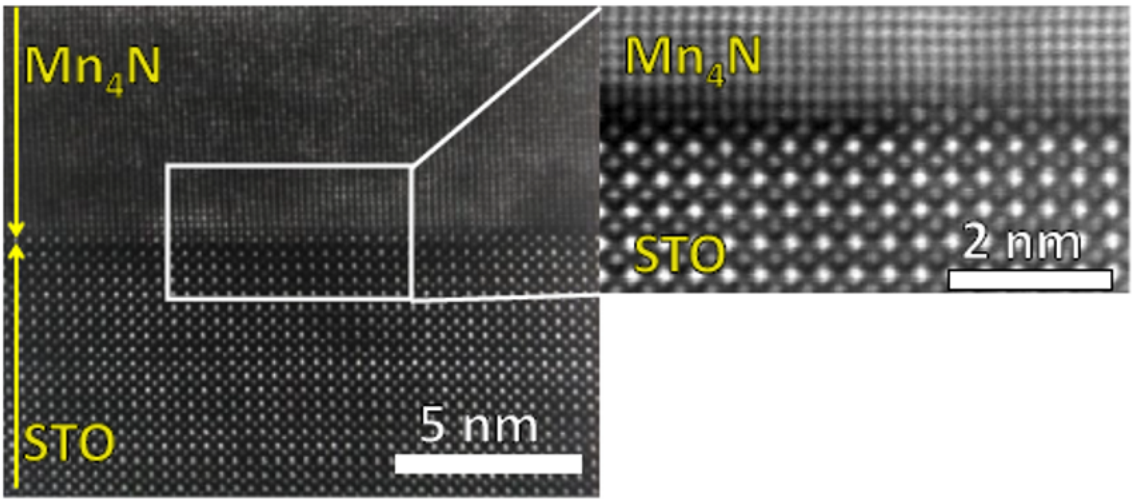

Figure 2.8: *Transmission Electron Microscope micrograph showing the crystal structure and the interface between the Mn_4N layer and the $SrTiO_3$ substrate.*

Transmission electron microscopy (TEM) was performed on the $Mn_4N/SrTiO_3$ is shown in Fig.2.8. The TEM and analysis was performed by Dr. Hanako Okuno of LEMMA group in CEA Grenoble. The TEM micrographs of $Mn_4N/SrTiO_3$ demonstrate a very good epitaxial growth, a very well defined and clean interface with the $SrTiO_3$ substrate. Due to the remarkable lattice matching, the Mn_4N layer possesses no obvious defects, such as twins or dislocations. Nonetheless, the existence of misfit dislocations due to the high lattice mismatch with MgO has been observed by Shen *et al* by TEM images[166].

The XRD profiles demonstrate an epitaxial crystalline growth of Mn_4N/MgO and $Mn_4N/SrTiO_3$, with a much superior quality for $Mn_4N/SrTiO_3$ system. TEM images, confirms these results, where no obvious defect could observed. It is also observed that $Mn_4N/SrTiO_3$ has a much smoother interface, originating from the good lattice matching between Mn_4N and $SrTiO_3$ and the Ti terminated $SrTiO_3$ surface.

2.5.3 Magnetic reversal under field

In order to compare the magnetic reversal and magneto-transport properties of Mn_4N/MgO and $Mn_4N/SrTiO_3$, VSM-SQUID, Anomalous Hall Effect (AHE) and transport measurements were performed on these thin films.

As seen in Fig.2.9 (a) and (b), magneto-transport measurements were performed on these films in the Van der Pauw configuration. These curves exhibit a Magnon-magnetoresistance (MMR) signal, corresponding to the contribution of magnons to the resistivity. This magnetoresistance allows the quantitative measurement of magnetization reversal in thin films with perpendicular magnetization[176, 177]. These MMR curves are usually observed on samples which have a high coercivity, as the signal is usually too small in low coercivity materials. The

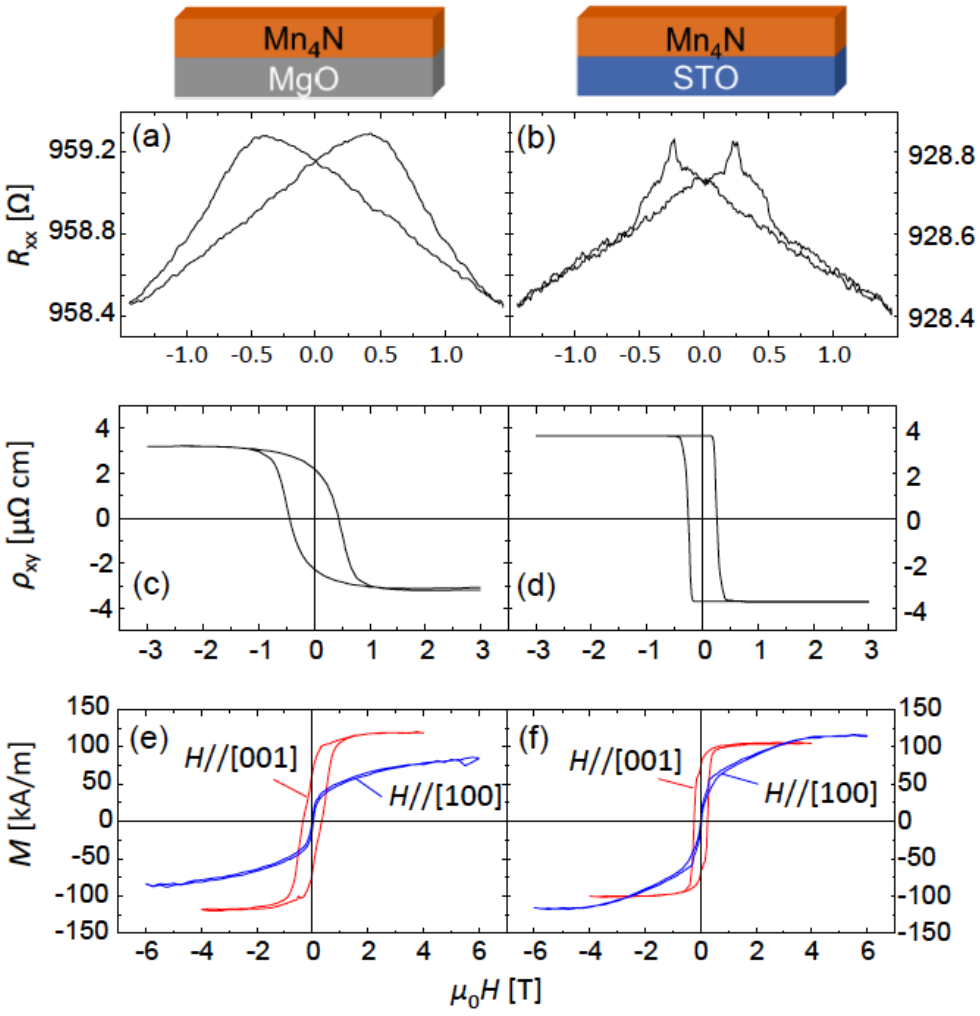

Figure 2.9: *Measurements obtained in thin films of Mn_4N/MgO and $Mn_4N/SrTiO_3$. (a,c,e) corresponds to MgO and (b,d,f) corresponds to $SrTiO_3$, with (a, b) longitudinal resistance vs applied magnetic field, (c, d) AHE hysteresis loops, and (e ,f) out-of-plane (red) and in-plane(blue) magnetization hysteresis curves.*

extracted resistivities of the thin films are 187 $\mu\Omega cm$ for the MgO substrate and 181 $\mu\Omega cm$ for the $SrTiO_3$ substrate at room temperature.

After changing the measurement configuration from the longitudinal configuration to a Hall (i.e., transverse) configuration, AHE measurements have been performed. These AHE plots are shown in Fig.2.9 (c, d). From the hysteresis loops, we observe a much sharper switching in the case of Mn_4N on $SrTiO_3$ than on MgO. Mn_4N on $SrTiO_3$ shows full remanence at zero field. The coercivity for the Mn_4N/MgO loop is 0.44 T, which is slightly higher than that of 0.26 T obtained for $Mn_4N/SrTiO_3$. These coercivities are higher than those found for most classical spintronics ferromagnets based on Co or Fe. This is due to the small saturation magnetization which reduces the Zeeman energy with respect to the anisotropy energy. The AHE measurements confirm the negative Anomalous Hall angle in Mn_4N. The transverse and longitudinal resistivity values obtained from the AHE and the Van der Pauw measurements at saturation allow extracting a very high AHE angle of (-2%), which is similar to previously reported values[167, 172].

The magnetic hysteresis loops of Mn_4N on MgO and $SrTiO_3$ are shown in Fig. 2.9 (e) and (f). Here, the red and blue curves represent the out-of-plane and in-plane measurements. The measurements were performed using a VSM-SQUID setup, with a maximum applicable field of 6 T. The out-of-plane hysteresis curves show a saturation magnetization of 118 kA/m for Mn_4N on MgO and 105 kA/m for Mn_4N on $SrTiO_3$ substrates. From the in-plane measurement, an anisotropy field $\mu_0 H_k$ of 4 T was estimated for $Mn_4N/SrTiO_3$. The uniaxial anisotropy constant K_U of $1.1 \times 10^5 J/m^3$ is calculated from the integration of the area between the in-plane and out-of-plane magnetization curves while taking into account the demagnetization energy. The demagnetization energy is very small in this case, as the saturation magnetization is very small.

The Van der Pauw measurements exhibit loops dominated by the MMR, which is indicative of a strong perpendicular anisotropy. The AHE curve of Mn_4N/MgO shows a smooth reversal under field, while that of $SrTiO_3$ has a sharper switching and full remanence at zero field. The VSM and magneto-transport measurements show that the magnetic properties are almost alike hence indicating that the thin films grown on separate substrate are intrinsically alike. The structural characterizations suggest that the increased disorder in films grown on MgO could be the reason for the higher coercivity and slanted AHE curve.

2.5.4 Macroscopic Magnetic Characterization

In this subsection, the magnetic domain patterns in Mn_4N layers grown on MgO and $SrTiO_3$ are examined using MFM and/or MOKE microscopy. Theoretically, the equilibrium domain width depends on the balance between the dipolar and DW energies ($\sqrt{AK_U}$). The DW width in Mn_4N was calculated to be around 37 nm using Eq. 2.2.

$$DW_{width} = \pi \sqrt{\frac{A}{K_U}} \tag{2.2}$$

where A is the exchange stiffness constant, which can be taken as 15 pJ/m (as estimated from the Curie temperature)[178], and K_U is the anisotropy constant. Using the analytical model described in ref.[179], the theoretical equilibrium domain width for a 10 nm thin Mn_4N layer can be estimated to be in the km range. Due to the small saturation magnetization in Mn_4N, the demagnetizing field is indeed almost negligible, so that creating small domains would lead to a DW energy increase without real gain in terms of demagnetizing field energy. For this reason, in Mn_4N, the real domain width and their shape depend on DW pinning on extrinsic defects, rather than on the competition between DW energy and demagnetizing field [180].

The domain patterns of Mn_4N layer were observed by MFM for Mn_4N/MgO samples, and by MOKE microscopy for $Mn_4N/SrTiO_3$ samples, as shown in Fig.2.10 (a) and (b). These images were obtained in the as-deposited state, before the application of any magnetic field, which can be considered to be close to the equilibrium state.

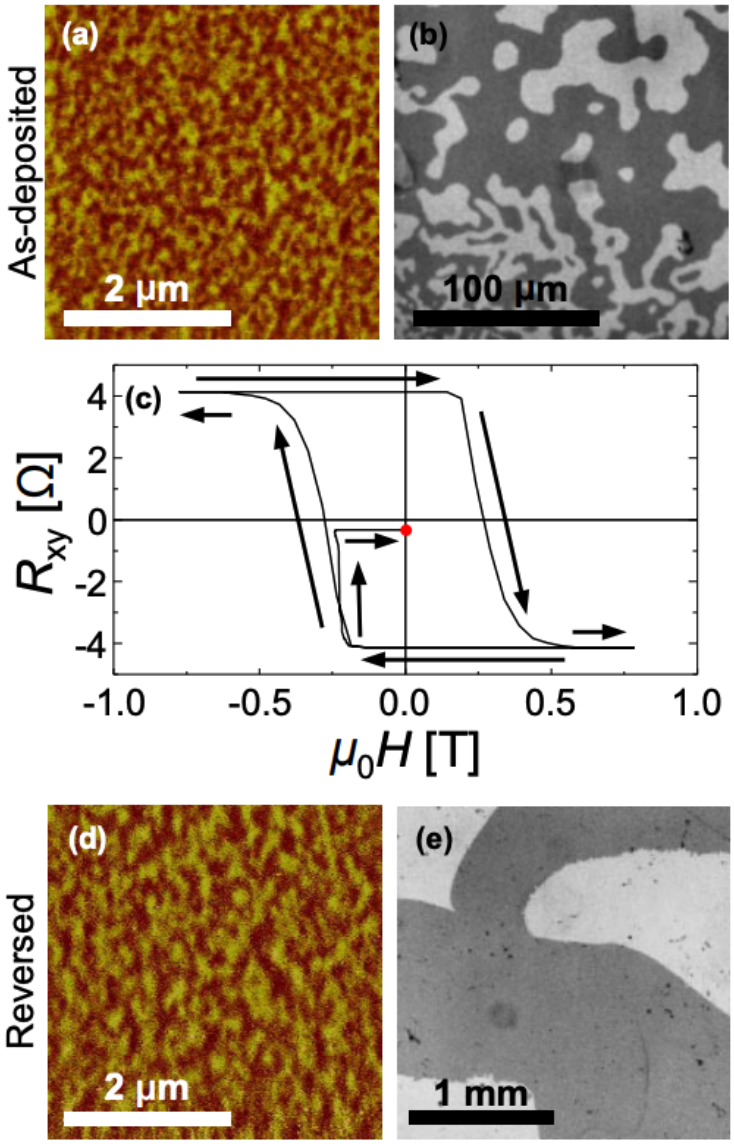

Figure 2.10: *(a) MFM image of a Mn_4N/MgO sample and (b) MOKE image of a $Mn_4N/SrTiO_3$ sample, both in the as-deposited state. (c) Magnetization curve illustrating the partial reversal process, monitored by anomalous Hall effect, in the $Mn_4N/SrTiO_3$ sample. The red dot corresponds to the final magnetization state, used for (e). (d) MFM image of the Mn_4N/MgO sample after partial reversal and (e) MOKE image of the $Mn_4N/SrTiO_3$.*

The mean domain period (D_P) is the total distance between two opposite domains is estimated using the two-dimensional fast Fourier transformation method[181]. The D_P was derived by Kaplan and Gehrier [182] and it is given in following Eq. 2.3.

$$D_p = 1.91\, t\, \exp \frac{\pi D_0}{t} \tag{2.3}$$

where t is the thickness of the thin film, $D_0 = \gamma_w/\mu_0 M^2$ is the characteristic length of the

material determined by the DW energy γ_w, and the saturation magnetization M_s. The domains for Mn_4N/MgO are small with a D_p of 0.28 µm, far from the equilibrium domain width, and with very rough DWs. This is indicative of a strong disorder which has been seen from TEM images in ref[166], and thus of the presence of crystallographic defects. In contrast, $Mn_4N/SrTiO_3$ samples have two orders of magnitude larger domains, with a value of D_p as least as large as 20 µm, and with smooth and rounded DWs. This is coherent with the higher crystalline quality of $Mn_4N/SrTiO_3$ thin films. Note that this is a very high value, even though similar domain sizes have been reported for ultrathin CoFeB(1.1 nm)/MgO(1 nm) and Pt(2.4 nm)/Co(0.27 nm) films with D_p values of 14 and 6 µm obtained after thermal demagnetization[181, 183], these are rather rare values.

MOKE images of Fig.2.10 (d) and (e) confirm the presence of very few nucleation sites during reversal for the $SrTiO_3$ system in contrast to the MgO one, and shows that the magnetization switching occurs by scarce nucleation and easy propagation, which is consistent with the sharp switching seen in the square AHE hysteresis loop, while for MgO magnetization reversal occurs rather by nucleation than propagation.

Overall, the significant differences between the hysteresis loops, domain size and domain widths for the two systems arise from the crystalline quality of the different films. It is clear from above shown structural and magnetic characterizations that $Mn_4N/SrTiO_3$ have much better properties as compared to Mn_4N/MgO. Such a crystallographic ordering in combination with a high perpendicular magnetic anisotropy and a small saturation magnetization makes it a perfect candidate for the study of DW motion.

2.6 Current Induced Domain Wall Dynamics in $Mn_4N/SrTiO_3$

In this section, we now focus on the current-induced DW dynamics in this $Mn_4N/SrTiO_3$. The low saturation magnetization, high PMA and smooth, large domains with low pinning indeed makes it an ideal candidate for current-induced DW motion. The velocity of the DW mainly depends on the saturation magnetization, spin polarization, damping factor (α) and on the non-adiabatic β factor. Let us see how these parameters will play a role in $Mn_4N/SrTiO_3$.

2.6.1 Sample preparation and setup

For the study of current induced DW motion, a new 10 nm $Mn_4N/SrTiO_3$ thin film was grown by MBE as shown in sec.2.5.1. A saturation magnetization of 71 kA/m was measured for this sample. Similar AHE angle of -2% and a longitudinal resistance of 178 µΩcm at room temperature was also measured as shown in section2.5.3. The AHE curve along with the MOKE microscopy image are shown in Fig.2.11.

To perform the DW motion experiments, 1 and 2 µm wide wires were fabricated by electron-beam lithography and Ar ion milling etching (cf. Appendix B). Each device had 20 wires in parallel and were 10 or 20 μm long. At the end of the wires, they converged into square pads on both sides to ease DW nucleation. Using optical lithography, 100 nm of Titanium-Gold-Titanium was deposited on top of the pads for improving electrical contacts to the sample.

Once fabricated, the samples were set in the polar MOKE microscopy setup, in order to perform the imaging of the magnetic domains. Here, the two magnetization directions are seen as either white or black contrast (cf. AppendixA).

A coil is placed under the sample holder, and connected to a power supply (voltage generator). The power supply provides microsecond long, high current pulses ($\sim$ several 100 A)

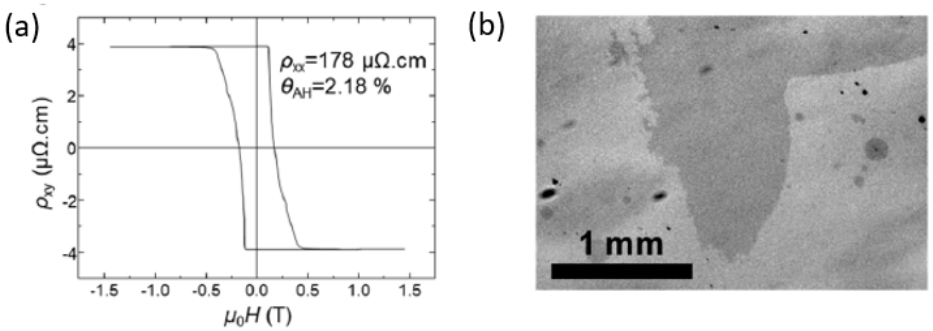

Figure 2.11: *(a) AHE hysteresis curve of a $Mn_4N/SrTiO_3$, showing a smooth reversal and a AHE angle of -2.18 for a resistivity of 178 μΩcm (b) MOKE microscopy image showing the domain pattern of a $Mn_4N/SrTiO_3$ sample, in a partially reversed state, the black contrast indicating the reversed domain.*

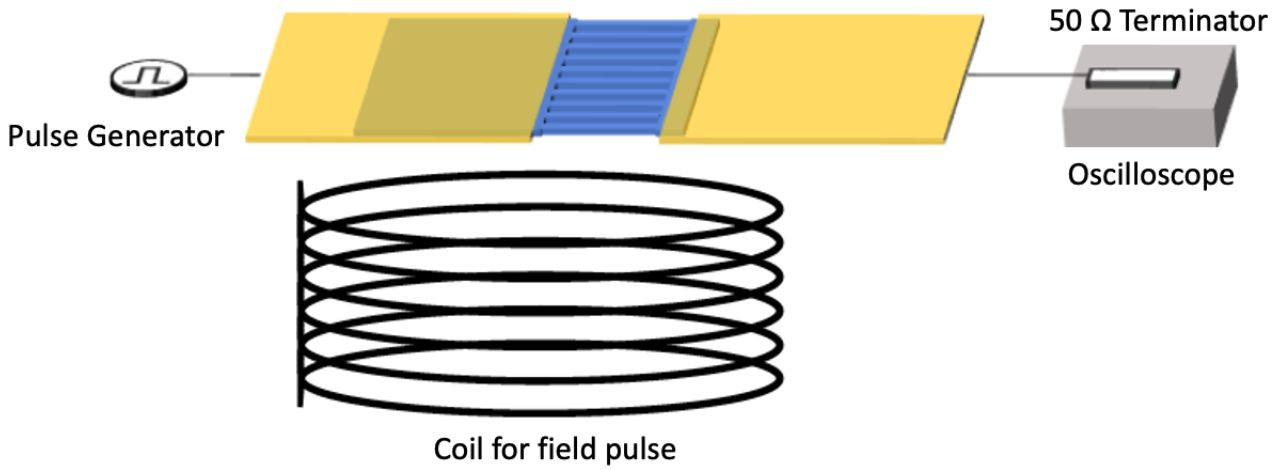

Figure 2.12: *Schematic of the domain wall motion setup, showing the microwires in blue, and in yellow the contact pads connected to the pulse generator and to the oscilloscope.[184]*

allowing to generate magnetic field pulses up-to 1 T. These field pulses are used to saturate the magnetization of the sample in one direction or the other. By varying the size and amplitude of the pulse, it is possible to nucleate the DWs at the edge of the wires. In order to move the DWs using currents, ultra-short (0.5-5 ns) current pulses are injected into the device using voltage source (up-to 80V). The intensity of the current pulse is extracted from the voltage pulse measured across the 50 ohm terminator of the oscilloscope in series with the circuit. The devices are also designed to be around 50 - 100 Ω, in order to match the output impedance of the voltage generator. The sample is glued to the sample holder using wax. The circuit is composed of 4 contact lines and SMA connectors adapted to high frequency signals.

2.6.2 Measurement and Analysis

For the DW motion measurements, the domains are first nucleated at the edges of the wires using the field pulses. The right nucleation regime is found by varying the amplitude and pulse width of the magnetic field pulses at the vicinity of the coercive field. After the nucleation of the domains, the DWs are moved along the wires by the application of current pulses of varying amplitudes and pulse widths. The pulse width was varied between 0.9 - 5 ns. For a given current pulse amplitude, a certain pulse width and a number of pulses are set, so that the DWs remain in the wires. The DWs are then repeatedly moved back and forth multiple times, in order to average the DW velocity. The black contrast in the differential Kerr images shown in Fig.2.13 represent the displacement of the DW during the application of the current pulses. The DWs are repeatedly moved back and forward in order to improve the statistics.

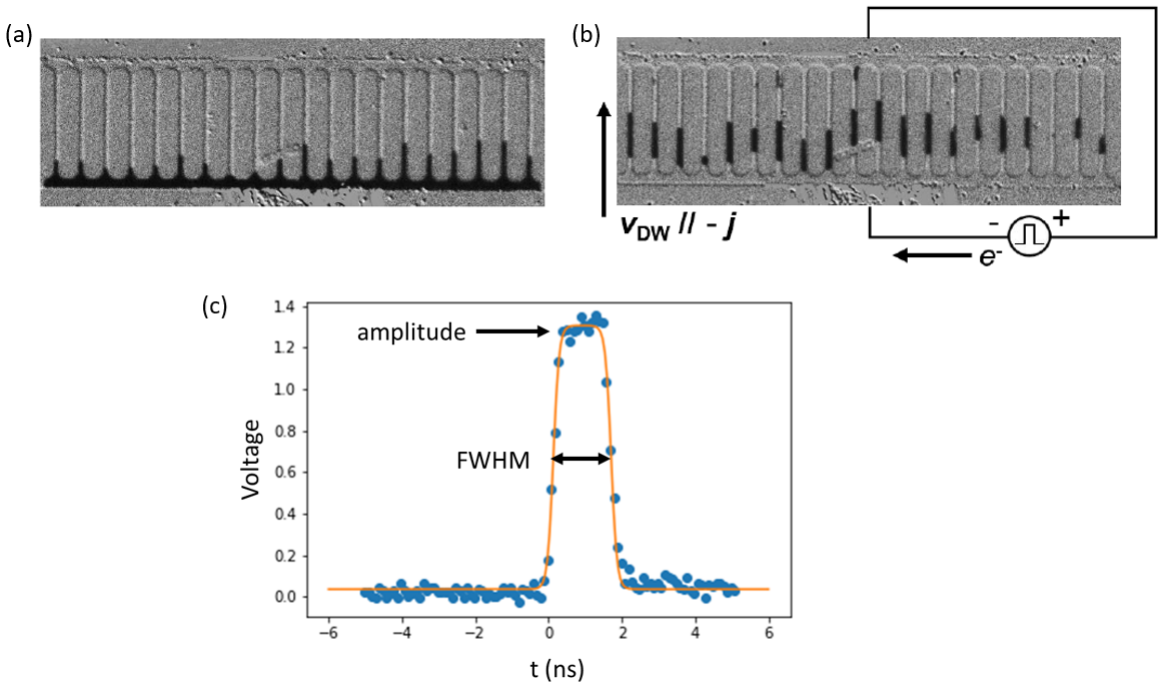

Figure 2.13: *(a) Domain nucleation at the edges of the 1 µm wide wires by application of perpendicular field pulses. (b) Domain wall motion after application of current pulses. (c) Shape of the current pulse measured using the oscilloscope. The blue dots are the raw data points, and the orange line is the fit of the pulse shape. From the fitting the amplitude and FWHM of the pulse are extracted.*

The images are saved and put through imageJ software for analysis[185]. The displacements of the DWs for a given amplitude, pulse width and number of pulses are computed and averaged.

The averaged displacement is then used to calculate the DW velocity at a given current density, by this Eq.2.4,

$$V_{DW} = \frac{\Delta X}{t_{pulse} n} \tag{2.4}$$

where, ΔX is the averaged DW displacement, t_{pulse} is the pulse width and n is the number of applied pulses. The current density is calculated by analyzing the pulse shape stored in the oscilloscope. The pulse amplitude is used for current density calculation whereas the pulse width is used for the calculating the velocity. The applied current is estimated by dividing the voltage amplitude by 50 Ω which is then converted into current density by dividing it by the total section of the microwires. Fig.2.14 shows the extracted DW velocity plotted against the current density, for both the 1 and 2 μm wide wires.

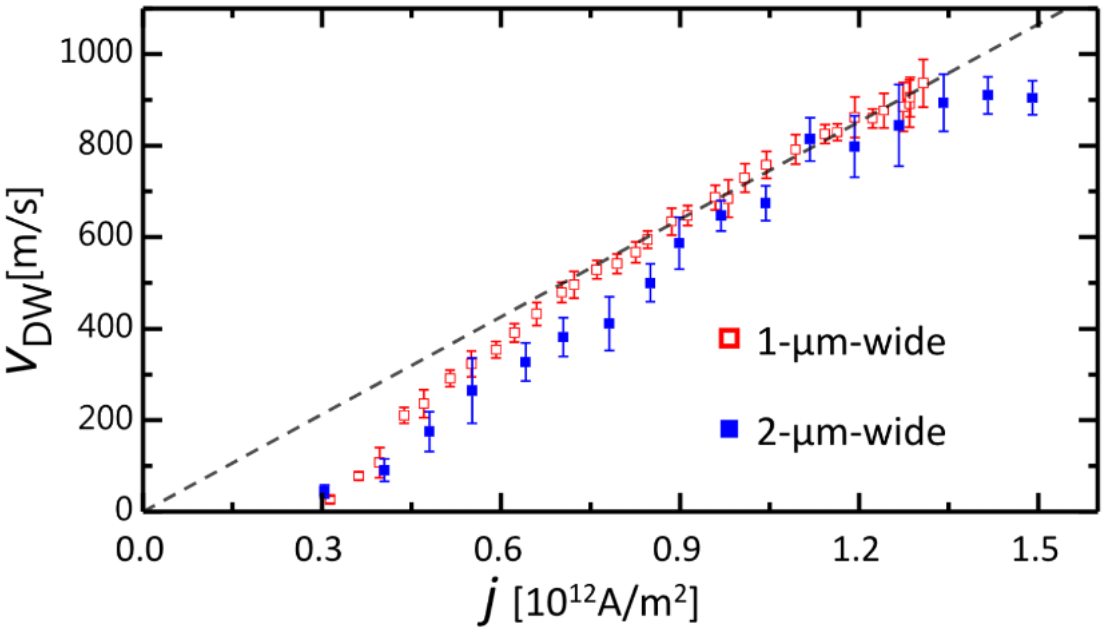

Figure 2.14: *Current density vs DW velocity of 1 (red) and 2 (blue) µm wide wires.*

From the Fig.2.14, we observe a low threshold current density of 3×10^{11} A/m^2 for both 1 and 2 μm for wide wires when applying 1 ns current pulses. This threshold current density is less than that of previously reported values for permalloy nanowires[33, 186–188], Co/Ni nanowires[189] and SOT driven Pt/Co nanowires[190].

At low current densities, as DWs are pinned by defects, the velocities change exponentially with the current density, in the so called creep regime[191]. Above a current density of $J = 0.85 \times 10^{12}$ A/m^2 the DW velocity varies linearly with J. Similar curves are observed for 1 μm and 2 μm wires curves. At the end of the linear regime, we achieve a very high DW velocity around 900 m/s at $J = 1.3 \times 10^{12}$ A/m^2. At this point the velocity of the 2 μm wide wires seems to be saturating. By applying pulses of current density higher than $J = 1.3 \times 10^{12}$ A/m^2, domains were nucleating everywhere in wires. This is a result of heating the nanowire close to its Curie temperature at 740 K or that the thermal energy becomes high enough to overcome the nucleation barrier.

The DWs shown here move in the direction of the flow of electrons which is consistent with the STT driven DW motion. All of the measurements were performed at room temperature without any SOT layer. Hence, we do not expect to have any interfacial DMI[192, 193] or SOTs[190] in $Mn_4N/SrTiO_3$. These results were a milestone for STT driven DW motion in

systems with PMA. These velocities are higher than what has been obtained in ferromagnetic materials with the highest DW velocities, from 400 m/s in Co/Pt system[190] (using SOT) to 750 m/s in anti-ferromagnetically coupled system with SAF[92] (using SOT + Exchange torque). These results are in line with DW motion with other ferrimagnetic materials such as GdFeCo[59](using SOT) showing a velocity of 1250 m/s, but at 260 K (close to the ACP). The exceptionally high DW velocity obtained in Mn_4N with STT and its analytical modelling are explored in the next section.

2.6.3 Dynamics and analytical model

The analytical modelling and subsequent micromagnetic simulations were performed by Dr. Jose Peña Garcia, at the Néel Institute, to understand our experimental observations. The process and results are shown in this section, and in the following one. In order to explore the high current-induced DW velocity achieved in $Mn_4N/SrTiO_3$ thin films, an analytical expression of the STT can be considered in the adiabatic limit. The 1D model describes the main features of the DW velocity under a spin-polarized current, in a perfect nanowire with out-of-plane anisotropy[194, 195]. Following the description given by Thiaville *et al.*[40], the magnetization dynamics is governed by a modified LLG equation in which the effect of the spin-polarized current is taken into account by introducing an additional term.

$$\frac{\partial \boldsymbol{m}}{\partial t} = \gamma_0 \boldsymbol{H_{eff}} \times \boldsymbol{m} + \alpha \boldsymbol{m} \times \frac{\partial \boldsymbol{m}}{\partial t} - (\mu \cdot \nabla)\boldsymbol{m} + \beta \boldsymbol{m} \times [(\mu \cdot \nabla)\boldsymbol{m}] \tag{2.5}$$

Here, $\boldsymbol{m}$ is the unit vector of the local magnetization, $\gamma_0 = \gamma\mu_0$ where γ is the gyromagnetic ratio and μ_0 the vacuum permeability. $\boldsymbol{H_{eff}}$ is the effective micromagnetic field, α is the Gilbert damping parameter, $\boldsymbol{\mu}$ is the spin drift velocity, which is along the flow of electrons and given as $\mu = \frac{g\mu_B}{2eM_s}PJ$, where g is the Landé factor, μ_B is the Bohr magneton, e is the electron charge, and M_s is the saturation magnetization of the thin film. Finally, β is the non-adiabatic term, representing a second-order term of the STT.

In the case of ferrimagnetic materials, the LLG equation has to be modified by taking into account the two different Landé factors of the two sub-lattices. However, as the orbital moment of Mn is close to zero, the Landé factors of both the Mn sub-lattices (close to 2) are very similar in this context. As the variation in the temperature in this system does not lead to compensation in $Mn_4N/SrTiO_3$, we have explained our results by taking an assumption that the DW dynamics is similar to that of a ferromagnetic system near room temperature[119].

In the adiabatic limit ($\beta = 0$) of the current driven DW dynamics, the DWs can move continuously only when their magnetization can start to precess, in order to align itself with the incoming spin-polarized electrons. In order for this to happen, the DW energy has to overcome the anisotropy energy K_D, which is the energy required to change the DWs from the Bloch to the Néel configuration. In the case of a thin film with perpendicular magnetization, K_D is given as $K_D = |K_x - K_y|$. For a thin strip of thickness t and width w, the DW can be modelled as an ellipse, and the two demagnetizing factors can be approximated as $K_x \approx \frac{1}{2}\mu_0 M_s^2(\frac{t}{t+\pi\Delta})$ and $K_y \approx \frac{1}{2}\mu_0 M_s^2(\frac{t}{t+w})$[43]. Using the 1 μm device width and a 10 nm thickness, K_D is calculated to be approximately 1.1×10^3 J/m^3. This value is much lower than that of similar permalloy nanowires, in which $K_D \approx 0.5 \times 10^6$ J/m^3. The DWs can overcome this energy barrier and start to precess only after the application of a certain current density, called the threshold critical current density J_c[52, 191].

$$J_c = \frac{2e}{\hbar P}\Delta(\varphi)K_D \tag{2.6}$$

where, $\hbar$ is the reduced planck's constant, P is the spin polarization of the conduction electrons, $\Delta(\varphi)$ is the DW width as a function of its tilt angle, i.e., the angle between the centre of the DW and the DW plane. The experimental material parameters for $Mn_4N/SrTiO_3$ being M_s = 71 kA/m, $K_u = 0.11 \times 10^6$ J/m^3, and taking A = 10 pJ/m and P = 0.8, the critical current density is expected to be $J_c \approx 1.9 \times 10^{10}$ A/m^2. Here the value of the exchange stiffness (A) was not measured but extrapolated from the Curie temperature of similar nitrides [178]. According to this calculation, J_c for Mn_4N is thus much lower than that of permalloy strips with in-plane magnetization ($J_c \approx 10^{13}$ A/m^2)[52]. It is however, comparable to that of ferrimagnetic TbFeCo strips with out of plane magnetization[196, 197].

In our experiments, the DW motion occurs at current densities much higher than J_c, so that adiabatic torques alone can perfectly explain the observed DW velocity. When $J \gg J_c$, the adiabatic torque-driven velocity is given as:

$$v \approx \frac{1}{1+\alpha^2}\sqrt{\mu^2 - \mu_c^2} \tag{2.7}$$

where, μ_c is the spin drift velocity at the critical current density. In the case of a small J_c in systems with PMA, the velocity can be written:

$$v \approx \frac{1}{1+\alpha^2}|\mu| = \frac{1}{1+\alpha^2}\,\frac{g\mu_B}{2eM_s}\,PJ \tag{2.8}$$

The damping factor of Mn_4N was estimated using time-resolved Kerr spectroscopy by Dr. Shinji Isogami at the National Institute for Material Science, in Tsukuba. It is a technique which is used to measure ultrafast magnetization dynamics in magnetic materials[198]. A damping factor of $\alpha = 0.15$ was obtained from this measurement. Introducing the damping factor in Eq.2.8, we can see that it has a negligible impact on the velocity. The mobility v/J is proportional to the ratio of the spin polarization and of the spontaneous magnetization (P/M_s). The spin polarization then becomes the only free parameter for the linear fitting. Using the proposed fitting in this regime, one obtains a very high polarization value, around P = 0.8 ($\pm$ 0.1), close to the polarization of the density of states obtained using first-principle calculations[199]. This analysis shows that the high DW velocity observed in Mn_4N is due to the low saturation magnetization and high spin polarization, in conjunction of the low DW pinning obtained on $SrTiO_3$ substrates.

2.6.4 Micromagnetic modelling

In order to confirm the results of the 1 D model, micromagnetic simulations were performed using the finite difference Mumax^3 software[200]. A defect free strip of 6000×120×10 nm^3 with a cell size of 2.5×2.5×10 nm^3 was used for zero-temperature simulations. To study the influence of the quality factor $Q = \frac{2K_u}{\mu_0 M_s^2}$ on the DW motion, the M_s was set at 1 kA/m while tuning the K_u. For the simulations, the parameters were set as M_s = 71 kA/m, $Ku = 0.16 \times 10^6$ J/m^3, A = 10 pJ/m, P = 0.7, $\alpha = 0.15$ and $\beta = 0$.

In the first step of the simulation, the DW configuration was set at equilibrium, in absence of spin-polarized current. After this, a current was applied along the positive x-axis, generating an adiabatic torque which resulted in the DW motion. A post-step function was used to make the simulation box "follow" the DW motion. The velocity of the DW was calculated from the DW

position as function of the time. An additional time of 25 ns was computed after the current was switched off to ensure that all transient effects are damped out. Lastly, the influence of the cell size, damping parameter, DW width, non-adiabatic torque and the geometry were also tested. It was concluded from these tests that these parameters do not strongly affect the DW motion in the precessional regime.

Fig. 2.15 shows a comparison between the DW velocities obtained from simulations done on an in-plane system (M_s = 1400 kA/m, $K_u = 9.75 \times 10^5$ J/m^3 and Q = 0.79) and an out-of-plane system(M_s = 1400 kA/m, $K_u = 1.95 \times 10^6$ J/m^3 and Q = 1.51). In the case of Q = 1.51, we see an overall agreement with the 1D model. The critical current density obtained here is around 10 u $\approx 2 \times 10^{10}$ A/m^2. Therefore, the DWs start to move linearly at very low current densities. There are however some slight differences from the 1D model which appear at lower values of μ (inset Fig. 2.15). At this point the DW moves discontinuously due to extrinsic effects, nonetheless the DWs could be displaced by the application of current density higher than J_c.

There are also some deviations from the linear regime which are observed for higher values of J. These deviations are attributed to DW asymmetry. In the case of Q < 1, for in-plane magnetized systems, there is a higher dipolar cost in bringing the magnetization out-of-plane and into precession. This translates into a higher critical current density (300 $u \approx 8 \times 10^{12}$ A/m^2), as expected from Eq.2.6. Hence, the linear regime is expected to occur at much higher current densities.

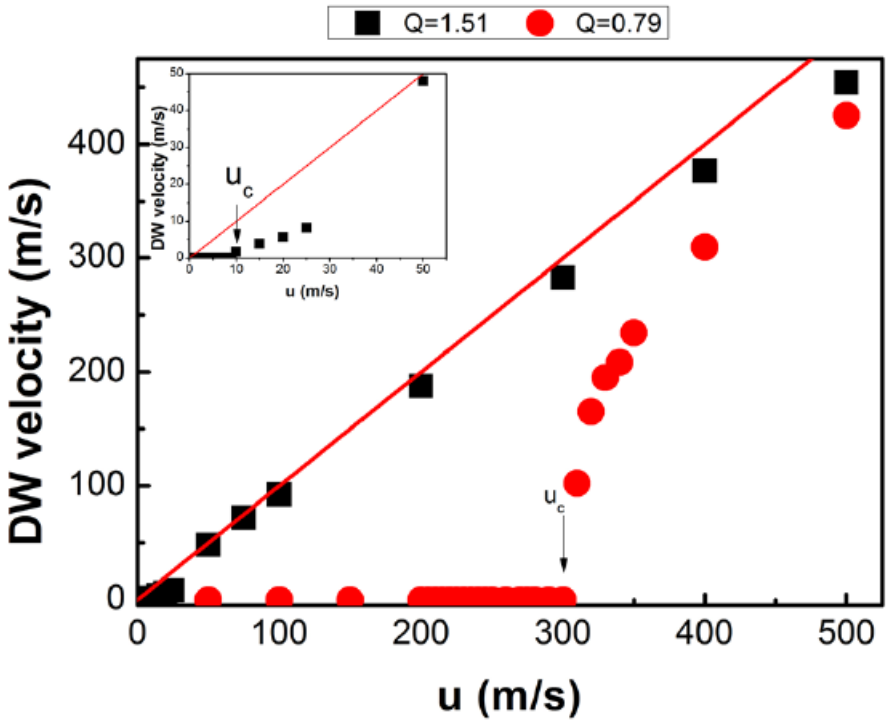

Figure 2.15: *Plots from micromagnetic simulations showing the DW velocity as a function of the spin-polarized current density, for two different values of Q; Q = 1.51 (black squares) and Q = 0.79 (red dots). The red solid line represents the 1D model velocity from Eq.2.6.3. The inset shows the details for small values of the spin-drift velocity for Q = 1.51.*

Influence of the damping factor and of the non-adiabatic torque on the current induced domain wall motion

Until now, we have neglected the non-adiabatic torque in PMA systems. The non-adiabatic term is used to explain the DW velocity in the case of in-plane magnetized permalloy below the intrinsic J_c. However, we have been able to explain the high DW velocity obtained in Mn_4N with adiabatic torque alone. Analytically, the non-adiabatic torque results in the steady regime in the velocity $v = \frac{\beta}{\alpha}\mu$ below the critical current density J_c, while in the precessional regime an additional term of $\frac{\alpha\beta}{1+\alpha^2}$ in included[43]. In the case of Mn_4N, the values of $\alpha = 0.15$ is thus much smaller than 1 whereas β should be in similar range as α[201]. Hence, the non-adiabatic term contribution should be negligible with respect to the adiabatic torque[201, 202].

Micromagnetic simulations were performed to justify our choice to neglect the contribution of the non-adiabatic torque, by considering the cases $\beta = 2\alpha$ and $\beta = 0.5\alpha$ with $\alpha = 0.15$. With the non-adiabatic torque, the DW velocity moves in a steady regime until it reaches the Walker limit given as:

$$\mu_W = \mu_c \frac{\alpha}{|\beta - \alpha|} \tag{2.9}$$

As shown in Fig.2.16, when neglecting the non-adiabatic term, the Walker spin-drift velocity coincides with the critical spin-drift velocity. As stated previously, the DW velocity starts to evolve linearly with J after J_c, in the precessional regime. At this point, the DW mobility is independent of the non-adiabatic β factor, as shown in Fig. 2.17.

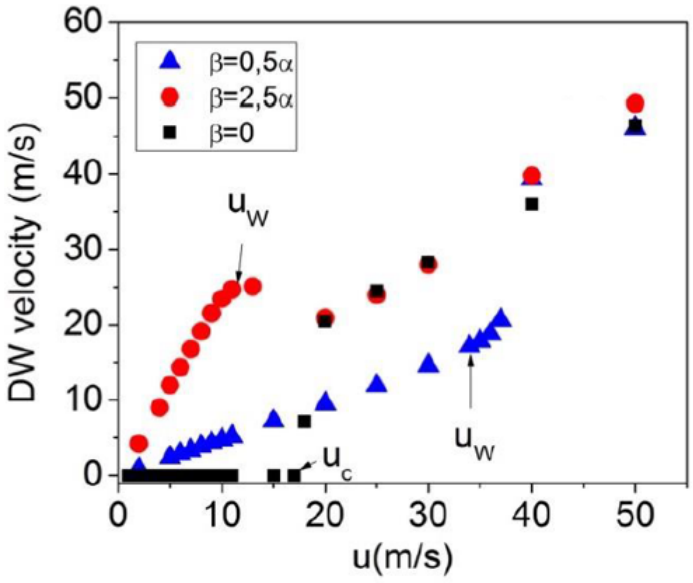

Figure 2.16: *Results of micromagnetic simulations showing the DW velocity as a function of the spin-polarized current for different values of β; $\beta = 2.5\ \alpha$ (red circles), $\beta = 0.5\ \alpha$ (blue triangles) and $\beta = 0$ (black squares) for low current densities close to the critical current density*

From these results, we can conclude that the non-adiabatic torque is not crucial to explain the high velocity obtained experimentally. Additionally the non-adiabatic regime is very well hidden below J_c, behind the thermally activated regime.

The Gilbert damping, on the other hand, plays a crucial role in DW motion. In order to study the impact of the Gilbert damping on the DW motion, micromagnetic simulations have been performed using $\alpha = 0.03$ and $\alpha = 0.3$, as shown in Fig. 2.18. These values are either

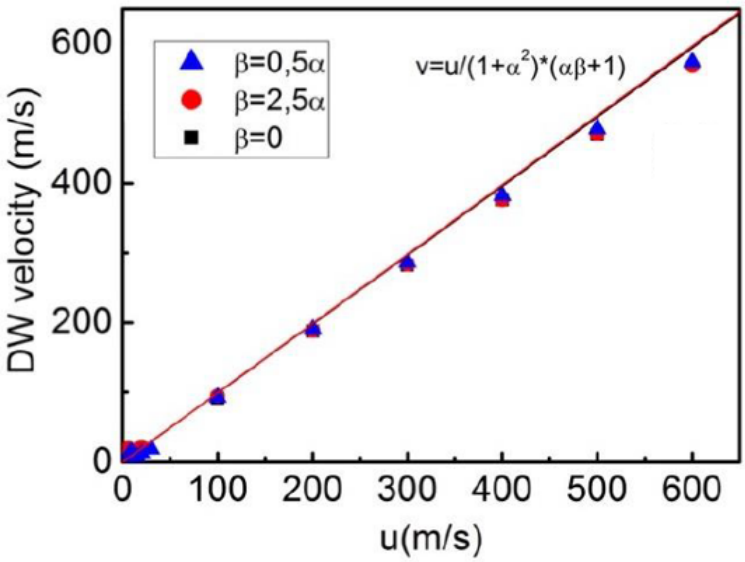

Figure 2.17: *Results of micromagnetic simulations showing the DW velocity as a function of the spin-polarized current for different values of β; $\beta = 2.5\ \alpha$ (red circles), $\beta = 0.5\ \alpha$ (blue triangles) and $\beta = 0$ (black squares) for high current densities, showing a linear behaviour in the precessional regime. The red solid line shows the 1D velocity from Eq.2.6.3.*

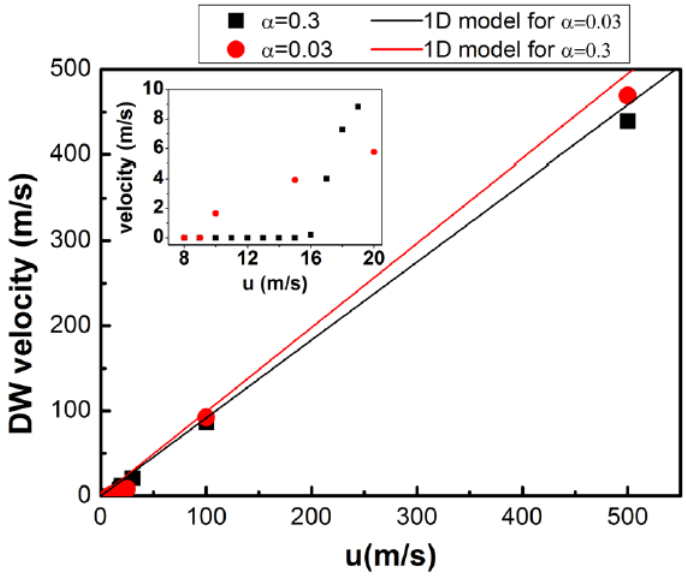

Figure 2.18: *Results of micromagnetic simulations showing the DW velocity as a function of the spin-polarized current for different values of α; $\alpha = 0.3$ (black squares) and $\alpha = 0.03$ (red circles) The solid lines represents the 1D velocity from Eq. 2.6.3*

bigger or smaller than the experimentally determined value of $\alpha = 0.15$. From both curves we observe that the velocity at the maximum current density is only 6% different. The inset shows that the larger damping results in a larger μ_c, however it is negligible in our case.

Damping and Non-adiabatic torque in the particular case of $\alpha = \beta$

Until now we have looked into the evolution of the DW motion in the steady regime below the Walker breakdown, and at higher current densities in the precessional regime. We have been able to reproduce our experimental DW velocities by simulating the precessional motion and assuming that the precessional velocity was equal to the spin-drift velocity. Nonetheless, according to the prediction of the 1D model, when the Gilbert damping and the non-adiabatic torque compensate each other (i.e., where $\alpha = \beta$), the Walker spin-drift velocity becomes infinite (Eq. 2.6.3). In such case, the velocity in the steady state regime is equal to the spin drift velocity for any applied current density. In order to check this effect in Mn_4N, micromagnetic simulations mimicking a PMA strip with Q = 1.51 and α=β=0.03 were performed. The results of these simulations are shown in Fig. 2.19(a) along with the comparison with the case with no non-adiabatic torque (β=0). From this it can be observed that the velocities do not vary substantially in between the two cases. Nonetheless, the DW moves as expected in the precessional regime when β=0, while it moves in the steady flow regime in the case of α=β. This is confirmed by the temporal evolution of the averaged x- and y- components of the DW magnetization, which are shown in Fig. 2.19(b,c). It is however very difficult to distinguish between the cases when the non-adiabatic torque and the Gilbert damping are balanced and unbalanced here. Nonetheless, note that this case of α=β has been demonstrated experimentally in (GaMn)As[202, 203], so we cannot completely exclude it.

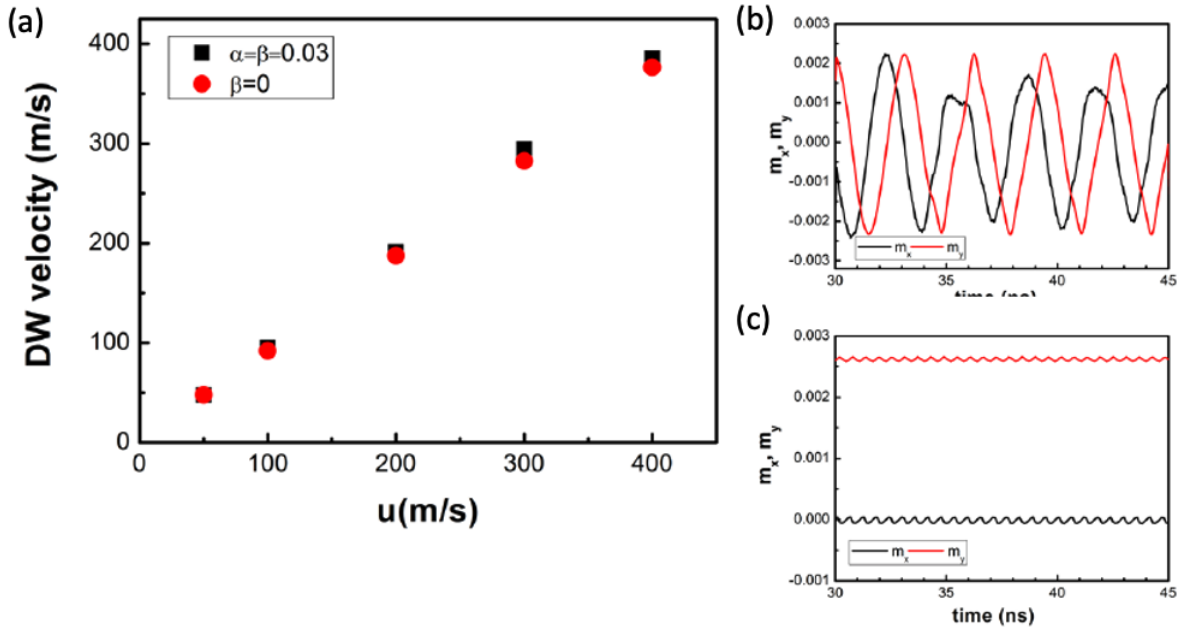

Figure 2.19: *Results of micromagnetic simulations showing (a): the DW velocity as a function of the spin-drift velocity for β=0 and α=β=0.03. (b,c) Temporal evolution of the averaged x- and y- DW magnetic components for α=β=0.03 (b) and β=0 (c) for μ=50 m/s.*

2.6.5 Absence of Dzyaloshinskii-Moriya Interaction and Chiral Néel walls

In this section, we will focus on field driven DW motion in $Mn_4N/SrTiO_3$ to confirm the DW configuration and show the absence of DMI in this system. The chiral Néel structure of DWs are generally stabilized by DMI. These DWs can then be moved by using SOTs either by SHE or the Rashba-Edelstein effect[50, 52, 190]. Field driven DW motion measurements were performed to investigate the nature of the DWs in our system.

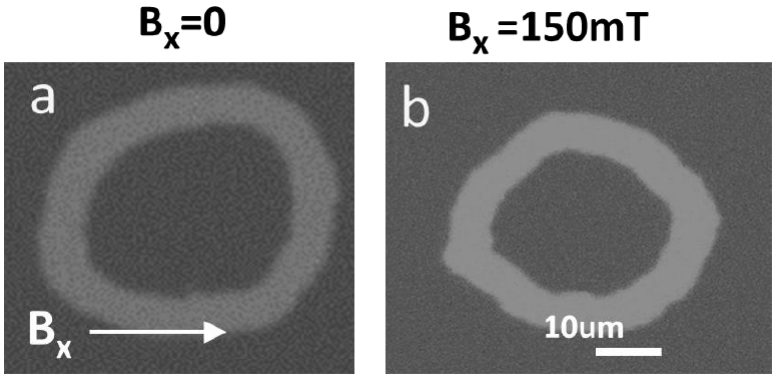

Figure 2.20: *Differential Kerr images (white contrast) showing the domain displacement driven by the out-of-plane magnetic-field pulse. The amplitude of the field pulse was around 400 mT, with a 30 ns pulse width. Result in absence (a) and presence (b) of an in-plane field B_x 150 mT*

For this measurement, a bubble domain is nucleated in a first step using out-of-plane magnetic field pulses on 10 nm layer of $Mn_4N/SrTiO_3$. In a second step, in the presence of a longitudinal in-plane field B_x, the DWs were moved with out-of-plane magnetic field pulses. This measurement was performed while increasing the longitudinal magnetic field in-plane.

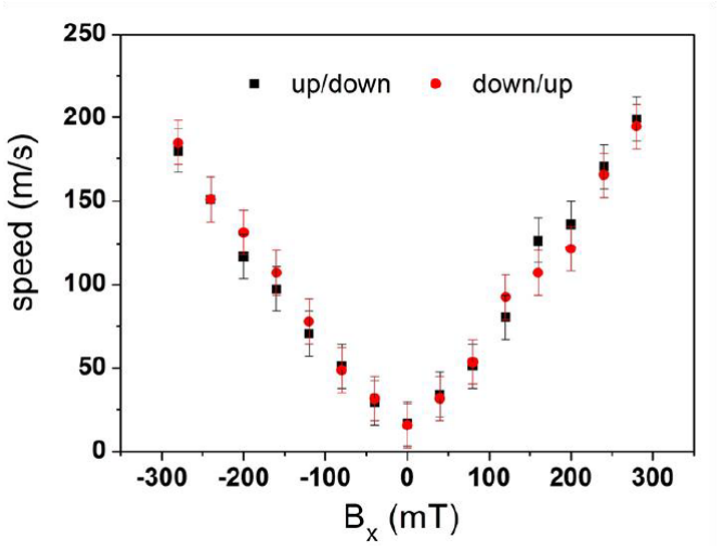

Figure 2.21: *Plot showing the Domain Wall velocity as a function of the applied, continuous, in-plane field B_x. Black points show velocities for up/down domain walls and red points for down/up domain walls*

This method is often used to quantify the DMI field in systems which have chiral Néel DWs. In the presence of chiral Néel DWs, there is an asymmetry in the velocity curve with the minima of the curve indicating the effective DMI field. This shift in the minima arises when the in-plane field totally compensates the DMI field[204–206].

Fig.2.21 shows the evolution of the DW velocity with the in-plane field in both orientations of B_x field. The DW velocity increases with the in-plane field value. The symmetry of the velocity curves confirms the absence of DMI and the Bloch nature of DWs in $Mn_4N/SrTiO_3$.

Summary

In this chapter, we have focused on the growth, and on the resulting structural and magnetic properties of Mn_4N. We have also studied the current induced DW dynamics in this system, demonstrating that Mn_4N is an exceptional candidate for DW-based applications, and that it is possible to reach high DW velocities using pure STT in ferrimagnets with low M_s. Here are the main points to remind :

- Nitrides are a large family of compounds including several magnetic nitrides.
- Mn_4N samples have been grown on MgO and $SrTiO_3$ substrates. Structural and magnetic characterization show that the growth on $SrTiO_3$ is far superior than that on MgO, which can be attributed to the very small lattice mismatch between Mn_4N and $SrTiO_3$.
- DW motion measurements were performed in microwires nanofabricated from 10 nm $Mn_4N/SrTiO_3$ thin films, using MOKE microscopy. A very high DW velocity of more than 900 m/s was observed at room temperature.
- DWs move in the direction of the electron flow, pointing to STT as driving mechanism. The absence of DMI and of a heavy metal layer excludes SOT as the underlying DW driving mechanism.
- High DW velocity can be explained using an analytical modelling taking into account only the adiabatic torques.
- Micromagnetic simulations confirm this assumption.
- The high DW velocity in $Mn_4N/SrTiO_3$ is thus found to be due to the high spin polarization and to the low M_s, in conjunction of low DW pinning.

In the next chapter, we will focus on the effect of substitution in this system, to get closer to the magnetic and angular momentum compensation points.

Chapter

3

Substitution in Mn_4N

After studying the growth, structural and magnetic properties of Mn_4N grown on $SrTiO_3$ and MgO in chapter 2 along with demonstrating DW motion dynamics in Mn_4N on $SrTiO_3$ substrate; In this chapter, we will discuss about substitution in Mn_4N with Ni and Co atoms. We will first start with the growth of the $Mn_{4-x}Ni_xN$ and $Mn_{4-x}Co_xN$ in section 3.2. In section 3.3 we will then compare the structural XRD characterization of both of these compounds. In the following section we will discuss the magnetic properties of these compounds with the help of Magnetization and AHE characterizations. We will also shed some light on the interesting results magnetic orientation of these compounds obtained using XAS and XMCD measurements and analysis in section 3.4 Note that I personally made the the study concerning substitution with Ni which will be shown in chapter 4. The results presented on substitution with Ni were led by Taro Komori. I collaborated to the part concerning substitution with Co, lead by Taro Komori and Haruka Mitarai.

3.1 $Mn_{4-x}Ni_xN$ and $Mn_{4-x}Co_xN$

In the case of Mn_4N, Juza *et al*[207] were the first who attempted to reach the compensation point with the replacement of Mn with Ni, Cr and Fe. Mekata also attempted to replace some of the Mn atoms in the Mn_4N system with In and Sn [106]. They had obtained the MC at appropriate composition ratios and temperature. The ability to tune the compensation points is very interesting in controlling and manipulating the magnetic properties of the materials. A plethora of different effects could be studied not only at the compensation points but also before and after them. AHE[56], AMR and SMR[208], DW dynamics[58, 59] and the damping factor[55, 56] are some of the effects which have been studied in such ferrimagnets. Here, we will discuss about Mn substitution in Mn_4N with Ni and Co magnetic atoms. As the compensation points were achieved with the substitution with non-magnetic In and Sn in Mn_4N, we expect the MC to be attained at room temperature much easily when doped with magnetic elements such as Ni and Co. The achievement of room temperature compensation point is very fascinating as it enables the material to be used in applications such as magnetic memories.

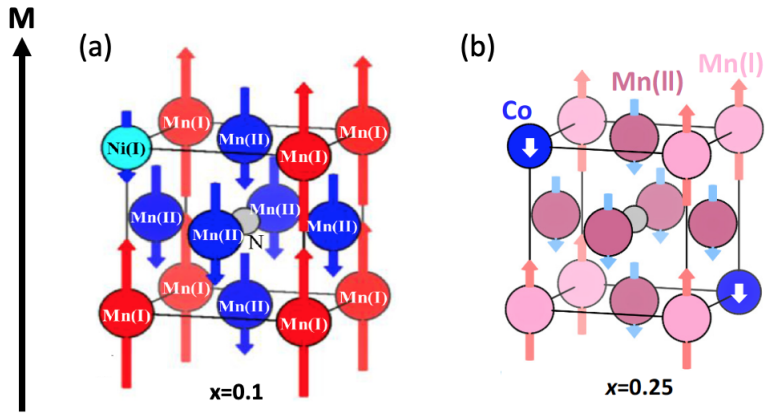

Figure 3.1: *Schematic of the anti-perovskite crystal structure of (a) $Mn_{4-x}Ni_xN$ with Ni concentration $x = 0.1$ [136] and (b) $Mn_{4-x}Co_xN$ with Co concentration $x = 0.25$ [138]*

3.2 Growth of $Mn_{4-x}Ni_xN$ and $Mn_{4-x}Co_xN$

10 nm thick layers of $Mn_{4-x}Ni_xN$ with two Ni concentrations of x = 0.1 and x = 0.25 were grown by MBE on $SrTiO_3$ (001) substrate at 450°C using high temperature Mn and Ni Knudsen cells and a RF-N plasma source. After the growth, the thin films were capped with 2-3 nm thick layer of Ti in-situ to prevent from oxidation of the magnetic layers.

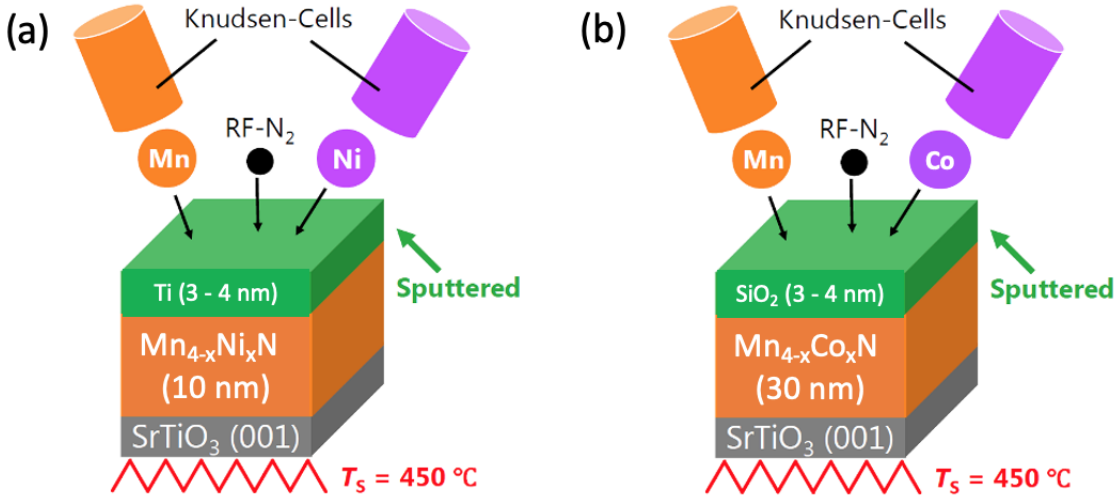

Figure 3.2: *Schematic of the MBE growth process for (a) $Mn_{4-x}Ni_xN$ (b) $Mn_{4-x}Co_xN$*

For $Mn_{4-x}Co_xN$, 30 nm thick layers were grown with Co on $SrTiO_3$ substrate with the Co concentration set at x = 0, 0.2, 0.4, 0.6, 0.7, 0.9, 1.0, 1.1, 1.2, and 1.3. These samples were also grown at 450°C using high temperature Knudsen cells of Mn and Co and a RF-N plasma source. 2-4 nm thick layer SiO_2 was used to cap the magnetic layer in-situ to prevent oxidation.

In both the cases, the $SrTiO_3$ substrates were cleaned by a buffer NH_4F-HF solution to obtain a TiO_2 terminated surface for the growth of the magnetic layer. The deposition rates of the Mn and Co were independently controlled by the crucible temperature for their respective Knudsen cells. The capping layers were deposited using RF-sputtering method.

3.3 Structural Characterization

$Mn_{4-x}Ni_xN$

RHEED characterization was performed on these thin films right before the deposition of a capping layer on the $SrTiO_3$ (100) plane. After capping the sample, in-plane ($\phi - 2\theta\chi$) and out-of-plane ($\omega - 2\theta$) XRD characterizations were performed. A XRR characterization was also done to obtain the thicknesses of these thin films.

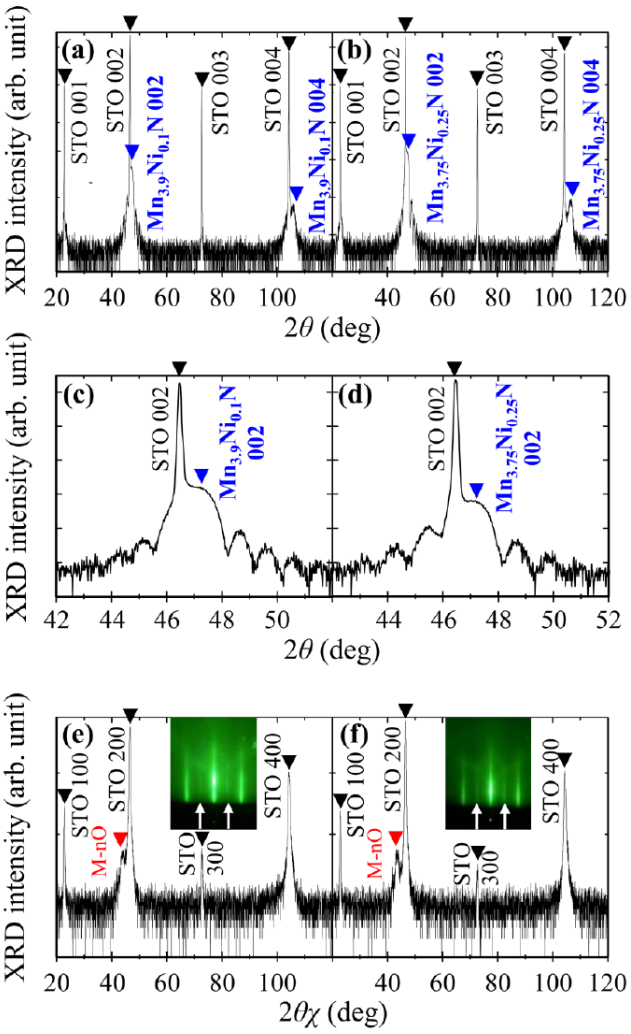

Figure 3.3: *XRD spectra of $Mn_{3.9}Ni_{0.1}N$ (a,c,e) and $Mn_{3.75}Ni_{0.25}N$ thin films grown on $SrTiO_3$. (a,b) are out-of-plane XRD patterns (c,d) shows an enlarged spectra closer to $2\theta = 46$. (e,f) in-plane XRD patterns with insets showing the RHEED patterns taken along the $SrTiO_3$[100] azimuth. The white arrows portray the lattice diffraction. Taken from Komori et al. [136]*

Fig.3.3 (a) and (b) shows the out-of-plane XRD profiles of $Mn_{3.9}Ni_{0.1}N$ and $Mn_{3.75}$-$Ni_{0.25}N$ thin films. In both the plots, the black arrows show the $SrTiO_3$ peaks while the blue arrows show the $Mn_{4-x}Ni_xN$ peaks. Since there is a very good lattice matching between the $SrTiO_3$ substrate and the $Mn_{4-x}Ni_xN$ thin films, the $SrTiO_3$ peaks are overlapped with the $Mn_{4-x}Ni_xN$ peaks. However, the $Mn_{4-x}Ni_xN$ appears at a slightly larger angle than the cubic $SrTiO_3$ and can be identified clearly when seen in the enlarged profiles of Fig.3.3 (c) and (d). The presence of the satellite peaks is also observed in these plots. The peaks of the $Mn_{4-x}Ni_xN$ along with

the satellite peaks are missing from the in-plane XRD profiles with only some Mn-O peaks which are observed next to the $SrTiO_3$ (200) peaks. The clear observation of Laue Fringe patterns along with the super-lattice diffraction peaks for 100 are good indication of a very good epitaxial crystalline structure. Both the XRD and RHEED patterns confirm a very good crystalline quality of these thin films. The lattice constants of $Mn_{4-x}Ni_xN$ were determined by the out-of-plane and in-plane XRD profiles with a c<a relation. Assuming that the $SrTiO_3$ is perfectly cubic, this relation suggests the presence of an in-plane tensile stress related to the perpendicular magnetic anisotropy in these thin films. The sharp diffraction peaks along with the Kikuchi lines obtained in the RHEED patterns suggest a highly c-axis oriented epitaxial films. The superlattice diffraction which are denoted by the white arrows in the RHEED images are attributed to the Nitrogen atoms correctly located at the centre.

$\mathbf{Mn_{4-x}Co_xN}$

Similar RHEED, XRD and XRR measurements were performed with the $Mn_{4-x}Co_xN$ thin films. Fig.3.4 shows the out of plane XRD profiles with the RHEED images in the inset. In the case of $Mn_{4-x}Co_xN$, the peaks are slightly more shifted from the $SrTiO_3$ (001,002 and 004) peaks than in $Mn_{4-x}Ni_xN$. Therefore, the peaks are more clearly observed. The diffraction peaks and streaky RHEED patterns from samples of Co concentration x = 0 - 0.4 confirmed the epitaxial growth of the thin films. The Kikuchi lines observed in thin films of x = 0 - 0.4 composition indicates a very good crystalline quality. The superlattice diffraction in the RHEED patterns which is indicative of the Nitrogen body centre are shown with the white arrows for samples with Co concentration $x \leqslant 0.9$. However, as the Co concentration was increased the XRD peaks of $Mn_{4-x}Co_xN$ were decreasing, indicating a degradation of the crystalline quality. The RHEED patterns were blurred and the $Mn_{4-x}Co_xN$ (004) diffraction peaks were not observed for x = 1.2. The in-plane lattice constant (a) along with the out-of plane lattice constant (c) decreased as the concentration was increased from x = 0 - 0.13. For lattice parameter a it decreased from 0.389 to 0.384 and for lattice parameter c it decreased from 0.386 to 0.381. However, this decrease in the lattice parameter still kept the in-plane mismatch between $SrTiO_3$ and $Mn_{4-x}Co_xN$ similar ($c/a \sim 0.99$).

XRD characterization of $Mn_{4-x}Ni_xN$ and $Mn_{4-x}Co_xN$ point towards an epitaxial growth of the thin films in 100 direction. There is however some peaks indicating the presence of some Mn related oxides which is inevitable. The XRD profiles along with the RHEED patterns confirm an exceptional crystalline quality of these thin films.

3.4 Magnetic Characterization

VSM-SQUID measurements, AHE measurements, X-ray Absorption Spectroscopy (XAS) and X-ray Magnetic Circular Dichroism (XMCD) were performed on the $Mn_{4-x}Ni_xN$ and $Mn_{4-x}Co_xN$ thin films to obtain their magnetic properties.

Magnetization and AHE characterization

$\mathbf{Mn_{4-x}Ni_xN}$

VSM-SQUID measurements were performed on the two $Mn_{3.9}Ni_{0.1}N$ and $Mn_{3.75}Ni_{0.25}N$ thin films. The magnetization hysteresis loops are shown in Fig.3.5 with (a) Ni concentration of 0.1 and (b) Ni concentration of 0.25. Magnetization values of 47 kA/m for the Ni concentration of 0.1 and 29 kA/m for Ni concentration 0.25 were obtained from these curves.

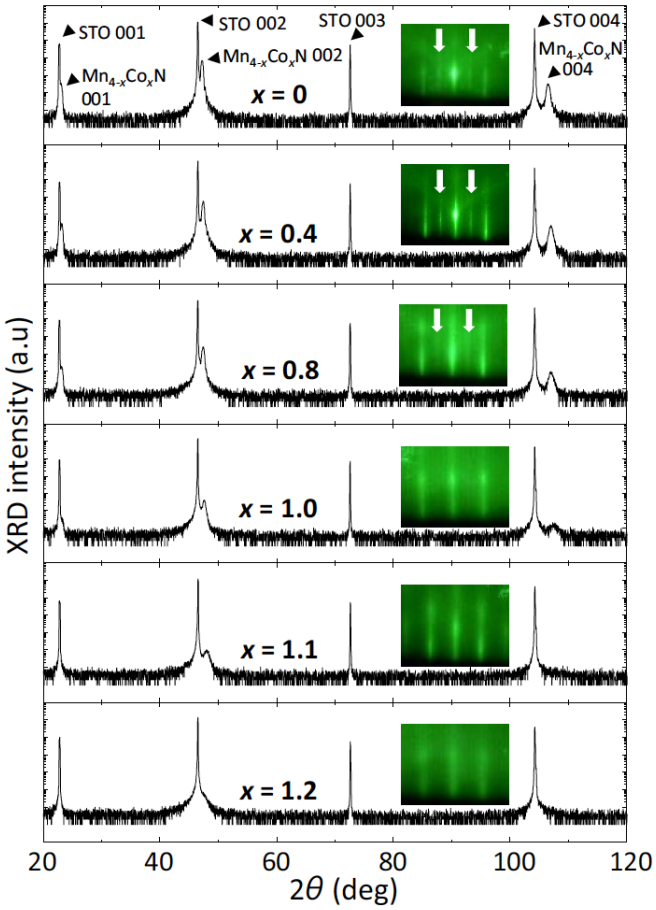

Figure 3.4: *Out-of-plane XRD profiles of $Mn_{4-x}Co_xN$ along the [100] azimuthal direction with the RHEED patterns in inset. The black triangles indicate the diffraction peaks of $Mn_{4-x}Co_xN$ and $SrTiO_3$ while the white arrows indicate the superlattice diffraction in the RHEED images. Taken from Mitarai et al [138]*

The hysteresis loops present a sharp switching behaviour indicating a very good PMA which is a result of the very good lattice matching. The magnetization is observed to be decreasing with the increase of Ni concentration in Mn_4N.

Fig.3.6 shows the AHE curves of (black) Mn_4N, (red) $Mn_{3.9}Ni_{0.1}N$ and (blue) $Mn_{3.75}Ni_{0.25}N$. From the AHE curves we observe the real difference between the two thin films with Ni concentrations. The change of the AHE angle from negative to positive is clearly observed from these curves. This change signifies the crossing of the magnetic compensation point which has been shown in TbCo[63] and CoGd[62]. Therefore, it can be inferred that there could be a point with the Ni substitution where the net magnetization becomes zero.

$Mn_{4-x}Co_xN$

The M-H loops of the $Mn_{4-x}Co_xN$ thin films of different Co concentrations were measured using a VSM. Figure 3.7 shows the M-H loops of the $Mn_{4-x}Co_xN$ thin films with different Co concentration. We observe nice square hysteresis loops for smaller Co concentrations and then as the Co concentration increases, this square hysteresis changes. However, it still retains the PMA at Co concentration of x=1.2.

The saturation magnetization obtained from the hysteresis loops in Fig.3.7 are plotted in Fig.3.8 as a function of the Co concentration in $Mn_{4-x}Co_xN$. From this curve, we clearly

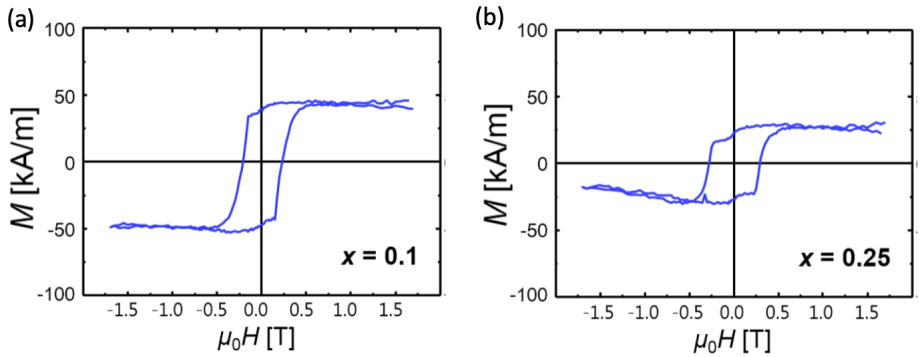

Figure 3.5: *Out-of-plane M-H loops of (a) $Mn_{3.9}Ni_{0.1}N$ and (b) $Mn_{3.75}Ni_{0.25}N$ thin films grown on $SrTiO_3$ substrates. Taken from Komori et al [136]*

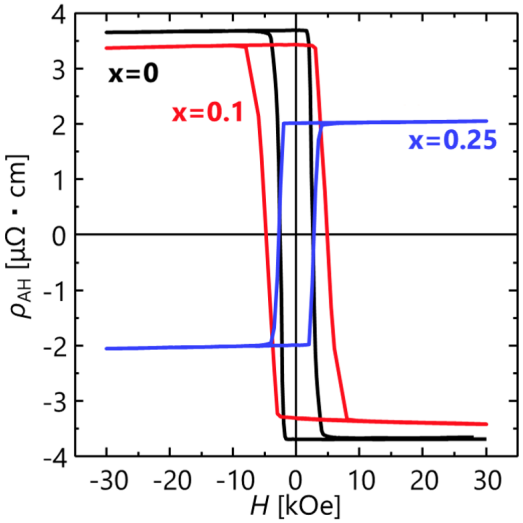

Figure 3.6: *Out-of-plane AHE loops of (black) Mn_4N, (red) $Mn_{3.9}Ni_{0.1}N$ and (blue) $Mn_{3.75}Ni_{0.25}N$ thin films grown on $SrTiO_3$ substrates.*

observe a decrease of the magnetization when Co concentration increases. The lowest saturation magnetization is observed at Co concentration x = 1.0 after which the saturation magnetization starts to increase again sharply. This trend signifies that the MCP has been crossed. However, it must be noted that the saturation magnetization values may not be very accurate because of multiple factors. One of these factors is the presence of antiphase boundaries (APBs) which could affect the saturation magnetization and lead to either larger or lower values as shown in the case of epitaxially grown Fe_3O_4 thin films[209, 210]. APBs are a common phenomenon observed for thin films grown by MBE where the growth process starts with the nucleation of islands and then closed layers. When changing from the islands to uniform layers, the layers gets divided into different domains or phases. The boundary between the different phases are known as APBs. There could be different exchange interaction between the spins of the two phases which lead to either an increase or decrease in the saturation magnetization. In the case of ferrimagnetic $Mn_{4-x}Co_xN$, as the saturation magnetization is already very low, such APBs could be play big role in determining the values of the saturation magnetization. Along with this, the presence of MnO peaks are observed by XRD could also vary the real value of the saturation magnetization. Another possibility is the presence of some ferromagnetic contamination in the $SrTiO_3$ substrate which is seen as an increase in the total saturation magnetization of the samples[211]. These saturation magnetization values are very small and

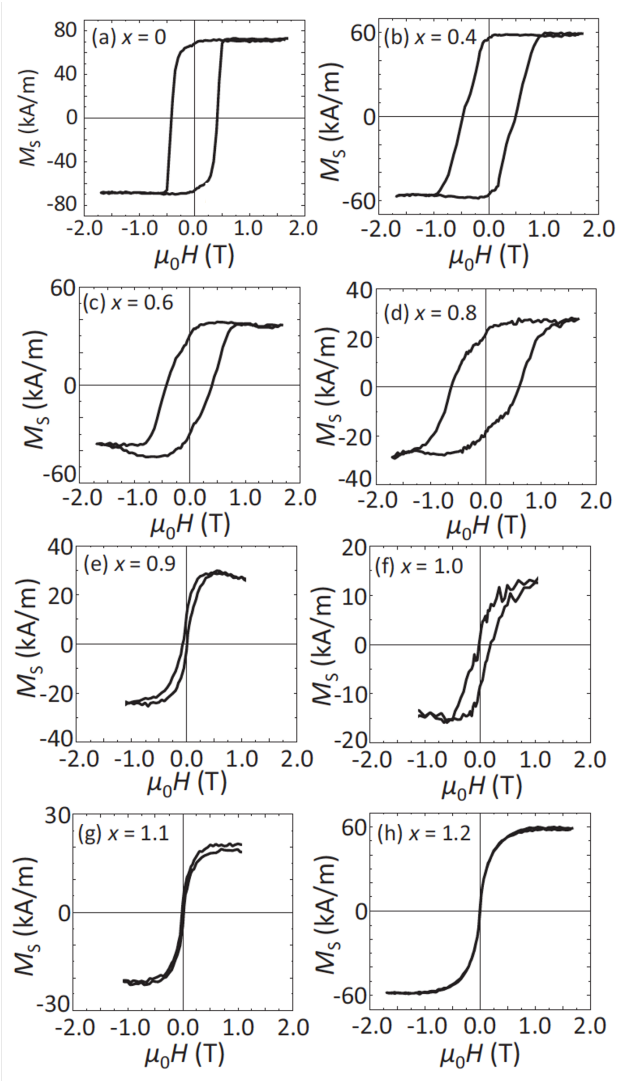

Figure 3.7: *Out-of-plane M-H loop of $Mn_{4-x}Co_xN$ thin films for a Co concentration varying from x=0 to x=1.3. Taken from Mitarai et al. [138]*

hence it is indeed very difficult to obtain extremely accurate values from the VSM.

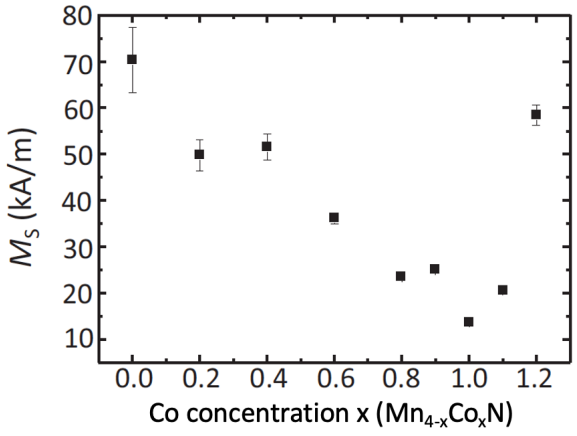

Figure 3.8: *Saturation magnetization as a function of the Co concentration. Taken from Mitarai et al [138]*

Fig.3.9 shows the out-of-plane AHE loops of the $Mn_{4-x}Co_xN$ thin films with the different Co concentrations. The shape of the these hysteresis loops are more clearer than the M-H loops. This effect could be attributed to the fact that it is a magneto-transport measurement and the effect of the Mn oxides does not reflect in the AHE measurements. It is also important to note that the AHE hysteresis loops are saturated under 1 T. It can inferred from this observation that the role of the APBs are minimal as in the case of high APBs interaction, the saturation occurs at much higher magnetic field than usual in the case of Fe_3O_4 thin films[209].

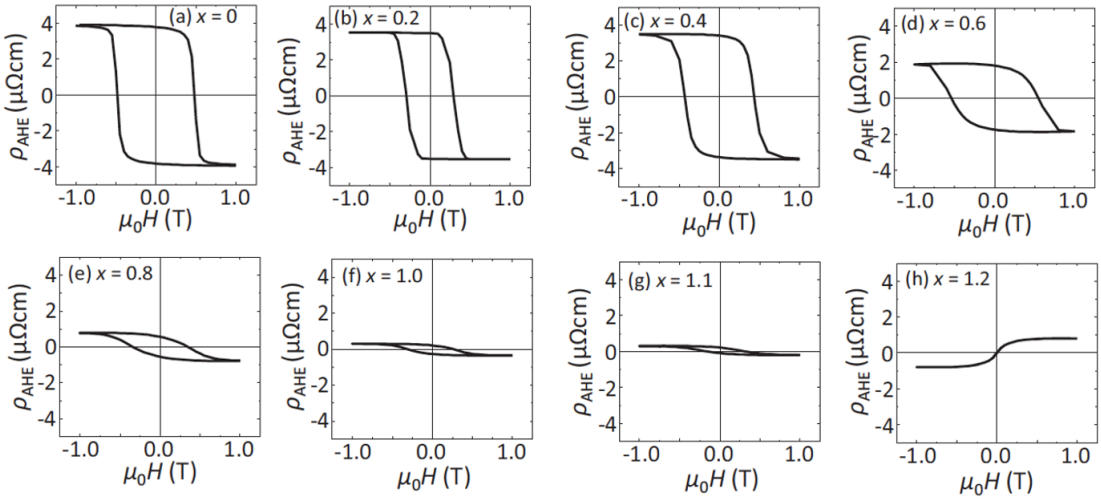

Figure 3.9: *Out-of-plane AHE (ρ_{AHE}) hysteresis loops of $Mn_{4-x}Co_xN$ thin films. Taken from Mitarai et al [138]*

The sign reversal of the AHE from negative to positive is observed between x = 1.1 and 1.2 which signifies the crossing of the MCP as seen before in the case of $Mn_{4-x}Ni_xN$. Hence, with the help of the AHE and M-H hysteresis loops, it is established that the MCP lies somewhere between x=1.1 to x=1.2.

By studying the AHE curves of $Mn_{4-x}Ni_xN$ and $Mn_{4-x}Co_xN$, we can clearly observe the change in the sign of the AHE indicating crossing the MCP. Hence, this validates that MCP could be achieved by the substitution of the Mn atoms by both Ni and Co at room temperature in Mn_4N.

XAS and XMCD characterization

The XAS and XMCD measurements and characterizations for the $Mn_{4-x}Ni_xN$ and Mn_{4-x}-Co_xN were performed by Taro Komori and Haruka Mitarai from University of Tsukuba. XAS and XMCD were performed at the twin APPLE-II undulator beamline BL-16A of Photon Factory in Japan [212]. For the measurements, a magnetic field of ± 3 T (for $Mn_{4-x}Ni_xN$), ± 5 T (for $Mn_{4-x}Co_xN$) and circularly polarized x rays with left and right polarization were applied at an angle of 54.7° for $Mn_{4-x}Ni_xN$ and 54.7°[213] for $Mn_{4-x}Co_xN$ to plane of the thin films. The x-ray polarization was switched at every energy point with a 10 Hz frequency at every energy point with while using five kicker magnets. The energy of the incident soft x rays was adjusted to include the L_2 and L_3 absorption edges of Mn, Ni and Co atoms. The XAS spectra were obtained at room temperature in the total electron yield (TEY) mode and the total fluorescence yield mode at the Mn $L_{2,3}$, Ni $L_{2,3}$ and Co $L_{2,3}$ absorption edges respectively for the $Mn_{4-x}Ni_xN$ and $Mn_{4-x}Co_xN$ thin films.

$Mn_{4-x}Ni_xN$

Fig.3.10 shows the XAS (top) and the XMCD (bottom) spectra of Ni atoms in $Mn_{3.9}Ni_{0.1}N$ (a) and $Mn_{3.75}Ni_{0.25}N$ thin films. Sharp peaks of Ni are observed in the XAS spectra at the L_3 edge between 852-853 eV and at the L_2 edge at 870 eV for both $Mn_{3.9}Ni_{0.1}N$ and $Mn_{3.75}Ni_{0.25}N$.

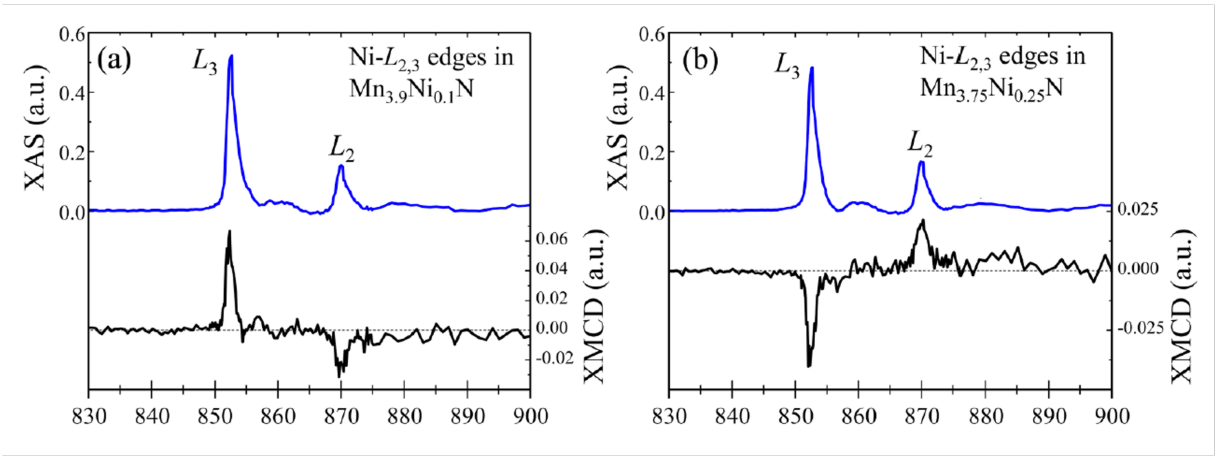

Figure 3.10: *XAS (top) and XMCD (bottom) spectra of (a) $Mn_{3.9}Ni_{0.1}N$ and (b) $Mn_{3.75}Co_{0.25}N$ thin films at the $L_{2,3}$ absorption edges for Ni. Taken from Komori et al [136]*

These XAS peaks at the L_3 and L_2 absorption edges mean that the Ni atom is replacing the Mn site I atoms in Mn_4N as they have exactly the same behaviour in the case of $Fe_{4-x}Ni_xN$ [114, 134, 214]. The XMCD spectra for Ni shows the reversed peaks between the $L_{2,3}$ edges. This is attributed to opposite direction of the Ni magnetic moments in $Mn_{3.9}Ni_{0.1}N$ and $Mn_{3.75}Ni_{0.25}N$.

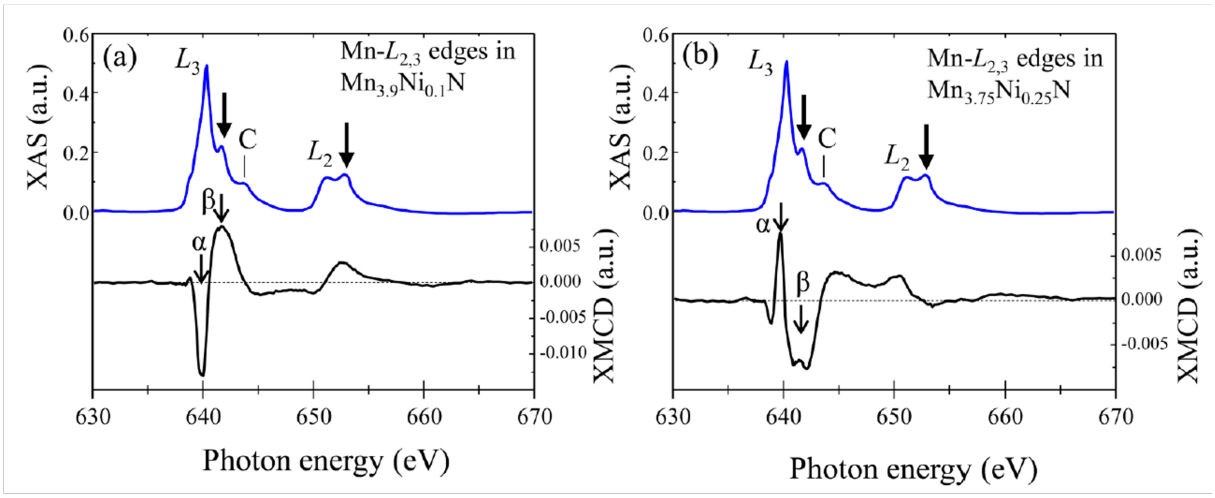

Figure 3.11: *XAS (top) and XMCD (bottom) spectra of (a) $Mn_{3.9}Ni_{0.1}N$ and (b) $Mn_{3.75}Co_{0.25}N$ thin films at the $L_{2,3}$ absorption edges for Mn. Taken from Komori et al. [136]*

Therefore, before the compensation point the magnetic moment of the Ni atoms point in the direction opposite to the net magnetization. After the compensation point, they point towards the net magnetization.

The XAS (top) and XMCD (bottom) spectra of the Mn $L_{2,3}$ absorption edges are shown in Fig. 3.11 (a) for $Mn_{3.9}Ni_{0.1}N$ and (b) for $Mn_{3.75}Ni_{0.25}N$. Shoulder peaks are also observed in the Mn XAS spectra for both the thin films. Additional satellite peaks are also observed in the spectra, which are attributed Mn related oxides and have been also observed in $MnFe_2O_4$

[215]. These MnO peaks are also visible in the XRD profiles, which could be a reason for these satellite peaks.

Unlike the XMCD peaks of Ni, the XMCD peaks of Mn are relatively more complex. The signs of the XMCD peaks are positive, then negative and then again positive around the L_3 edge when going from low to high photon energy in the case of $Mn_{3.9}Ni_{0.1}N$. This superposition of spectra having different signs signifies that the magnetic moments of the Mn(I) and Mn(II) are anti-parallel to each other. Such peaks are representative of the fact that the transition metal at the site I is localised and that the site II correspond to the itinerant states which have been shown in the case of Fe_4N and Mn_4N[113, 137]. Similarly, the XMCD spectra shown here are with the α and β peaks denoting the localised and itinerant states with opposite signs.

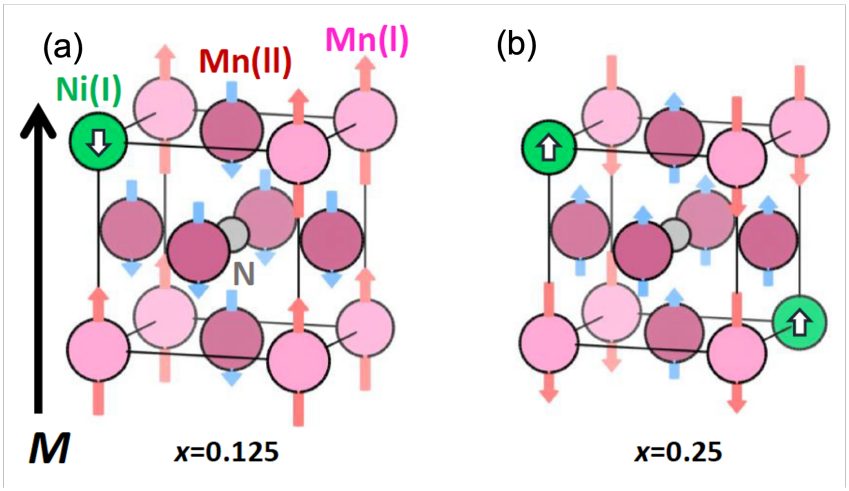

Figure 3.12: *Schematic of the Anti-perovskite crystal structure of (a) $Mn_{3.9}Ni_{0.1}N$ and (b) $Mn_{3.75}Ni_{0.25}N$.*

In the case of $Mn_{3.9}Ni_{0.1}N$, the broader β peak near 642 eV originates from Mn (II) site atoms. This broader peak is the result of the hybridization between the Mn (II) 3d and N 2p orbitals. In comparison, the sharp α peaks comes from the Mn(I) atom with its less hybridization with the N atom. The XMCD spectra of $Mn_{3.75}Ni_{0.25}N$ shows negative, then positive and negative again peak which is exactly opposite to that of $Mn_{3.9}Ni_{0.1}N$. These opposite peaks are attributed to the reversal of the magnetization between the two thin films at both the sites I and II. This behaviour of the XMCD spectra have been reported close to the compensation temperatures for other ferrimagnets as well [114, 216]. It is interesting to note that the sign of the XMCD spectra of Ni is exactly opposite to that of the α peaks, demonstrating that the Ni always aligns anti-parallel to magnetic moment of the Mn site I atoms in this range of Ni concentration.

$Mn_{4-x}Co_xN$

Fig.3.13 shows the XAS and XMCD spectra of the Mn atoms at the $L_{2,3}$ absorption edges for (a) $Mn_{3.8}Co_{0.2}N$,(b) $Mn_{3.2}Co_{0.8}N$ and (c) $Mn_{2.7}Co_{1.3}N$ thin films. There are very slight differences between the three XAS spectra for Mn. In contrast, there is a big difference observed in the three XMCD spectra.

In the case of $Mn_{3.8}Co_{0.2}N$, the signs of the XMCD signal around the L_3 absorption edge goes from positive, then negative and then positive again when going from the low photon to high photon energy. For $Mn_{3.2}Co_{0.8}N$, it is reversed and goes from negative, then positive and then negative again. Fascinatingly, for $Mn_{2.7}Co_{1.3}N$, it reverses again and goes from positive, then negative and then positive again. This superposition of spectra with opposite peaks

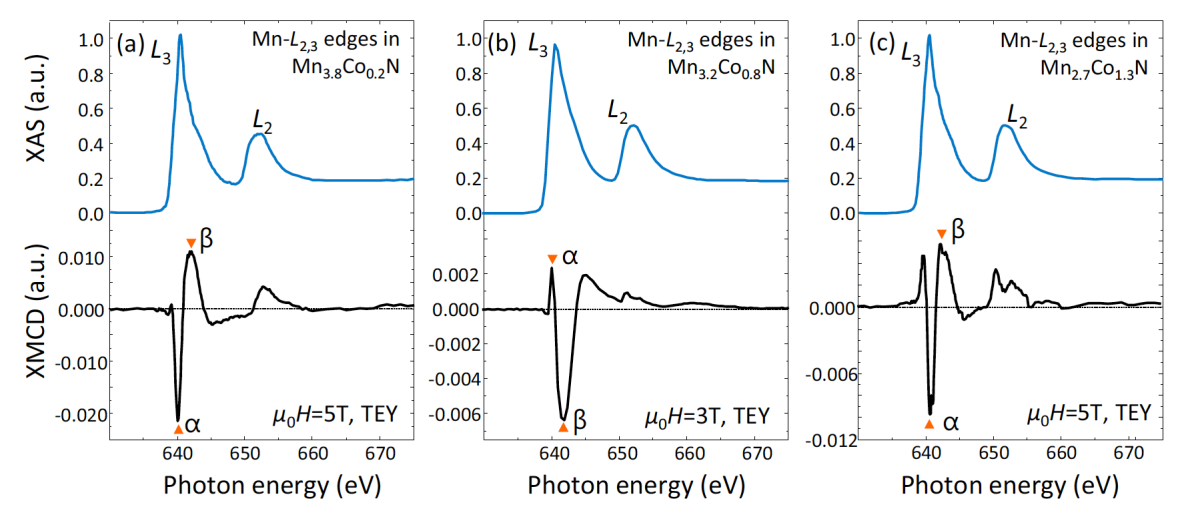

Figure 3.13: *XAS (top) and XMCD (bottom) spectra of (a) $Mn_{3.8}Co_{0.2}N$, (b) $Mn_{3.2}Co_{0.8}N$ and (c) $Mn_{2.7}Co_{1.3}N$ thin films at the $L_{2,3}$ absorption edges for Mn. In the XMCD spectra the sharp α and the broad β peaks originate from the Mn site I and Mn site II atoms. Taken from Mitarai et al. [138]*

demonstrates that the Mn site I and Mn site II atoms have an anti-parallel alignment. Here the sharp α peaks again correspond to the localised Mn site I atoms and the broader β peaks correspond to the Mn site II Nitrogen hybridized sites. In this anti-perovskite crystal structure, the corner site I atoms are localised while the face-centered site II atoms are itinerant in nature, which has been demonstrated by XMCD measurements and first principle calculations as well in Fe_4N [113] and in Mn_4N [137]. These results suggests that the magnetic moments of the Mn site I and Mn site II have been reversed between Co concentration of x=0.2 and 0.8, and again between x = 0.8 and 1.3.

Fig.3.14 shows the XAS and the XMCD spectra of Co at the $L_{2,3}$ absorption edges for (a) $Mn_{3.8}Co_{0.2}N$,(b) $Mn_{3.2}Co_{0.8}N$ and (c) $Mn_{2.7}Co_{1.3}N$ thin films. For the Co XAS absorption peaks, there is slight difference between the three films. In the XMCD spectra the A and A' peaks represent the Co site I atoms at the two $L_{2,3}$ edges. It is similar to what has been shown in the previous work Ito *et al* [137]. The sign of the Co A-A' peaks are reversing between the Co concentrations of x = 0.2 and 0.8. It means that the the magnetic moments of the Mn I, Mn II and Co I are reversing the magnetic moment direction between Co concentration of x = 0.2 and 0.8. It is therefore indicative of crossing the MCP which means that the there should be the MCP, which means that there should MCP somewhere between Co concentration x = 0.2 and 0.8. This point is however not seen through the M-H loops as a very finer control of the Co concentration could be required to reach this compensation point. We also do not see a change in the direction of the AHE angle between these points which is an indicator of the crossing of MCP which can be seen in the case of $Mn_{4-x}Ni_xN$. A more in-depth study of the AHE effect in this $Mn_{4-x}Co_xN$ system is thus required to understand the behaviour of the AHE.

The XMCD spectrum of $Mn_{2.7}Co_{1.3}N$ is very different from that of $Mn_{3.8}Co_{0.2}N$ and $Mn_{3.2}Co_{0.8}N$ in Fig. 3.14. In this case, we observe an additional B and B' peaks along with the A and A' peaks near the $L_{3,2}$ absorption edges. There is therefore an overlap between two sets of components in the XMCD signal.

It is striking to observe the reversal of A(A') peaks between Co concentration x = 0.8 and 1.3. This shows that the magnetic moment of the Co site I atoms are reversed between these two compositions. Here, the peak position of B and B' are slightly shifted from that of the A and A' peaks, signalling that they are similar to the α and β peaks seen in the XMCD spectra

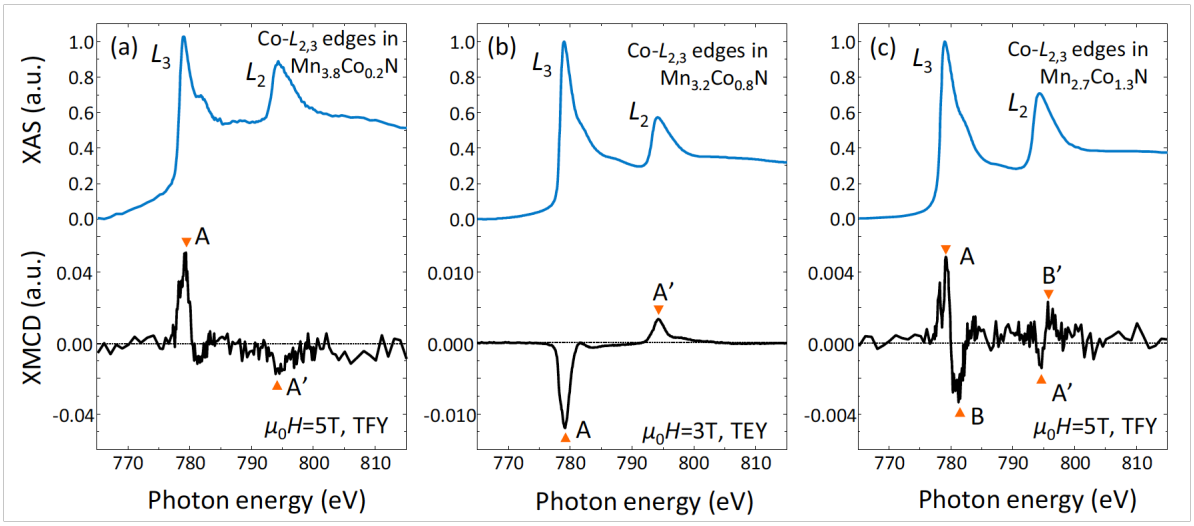

Figure 3.14: *XAS (top) and XMCD (bottom) spectra of (a) $Mn_{3.8}Co_{0.2}N$, (b) $Mn_{3.2}Co_{0.8}N$ and (c) $Mn_{2.7}Co_{1.3}N$ thin films at the $L_{2,3}$ absorption edges for Co. Taken from Mitarai et al. [138]*

of Mn. These peaks are attributed to the Co site II atoms similar to the case of Mn site II atoms. Therefore, in the case of $Mn_{2.7}Co_{1.3}N$ the Co is also replacing the Mn site II atoms and occupying their positions. The magnetic moment of the Co site II atoms are now aligned with the Mn site II atoms. This is evident when the B and B' peaks are compared to the α peaks in the XMCD spectra of Mn.

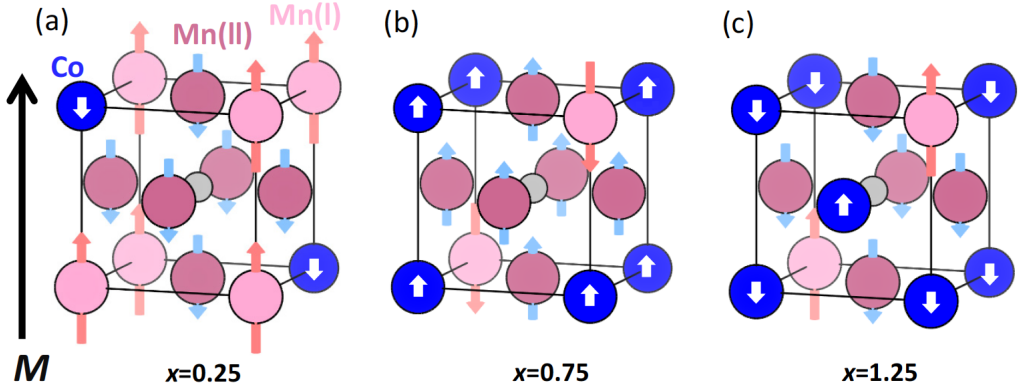

Figure 3.15: *Schematic of the Anti-perovskite crystal structure of (a) $Mn_{3.75}Co_{0.25}N$ (b) $Mn_{3.25}Co_{0.75}N$ and (c) $Mn_{2.75}Co_{1.25}N$. Taken from Mitarai et al [138]*

Overall, we observe a change in the sign of the α, β and A,A',B,B' between Co concentration of x = 0.8 and 1.3. This is attributed to a crossing of the MCP between these two compositions. This is well confirmed with AHE and M-H curves which are shown in Fig.3.8 and 3.9. From these results it could be inferred that after crossing the MCP, the Co atoms occupies either the Mn site I or site II randomly. One would expect that at x = 1, the Co completely occupies all the corner sites (site I). However, the α peak in the XMCD for Mn shows that there is still Mn atoms remaining at the corner site. Fig. 3.15 shows a simplified illustration of the anti-perovskite crystal structure of $Mn_{4-x}Co_xN$ for different Co concentrations. It illustrates how the Co is being substituted into this system. When x = 0.2, the sum of the magnetic moments from Mn(I) is higher than that of the sum of Mn(II) and Co(I), hence the magnetization points in the direction of Mn(I). At x = 0.8, the sum of the magnetic moments of Co(I) and Mn(II) is

higher than that of the sum of the remaining Mn(I) making the magnetization point towards Mn(II). At x = 1.3, the sum of the magnetic moments of Co(II) and Mn(I) atoms is higher than the sum of the magnetic moments of Co(I) and Mn (II) thus making the magnetization point in the direction of Mn(I) again. As mentioned earlier, it should be also noted that the possibility of Co atoms completely filling the corner sites cannot be fully ruled out.

XAS and XMCD study of the $Mn_{4-x}Ni_xN$ thin films were performed. From the XAS of the Mn $L_{2,3}$ edges, shoulder peaks were observed which were 2 eV higher than the main Mn peaks. We have attributed these shoulder peaks to the orbital hybridization of the Mn site II atoms with the N body centre atoms. This becomes more clear when the we study the XMCD α and β peaks. However, such shoulder peaks in the XAS were not observed for the Ni atoms for both $Mn_{3.9}Ni_{0.1}N$ and $Mn_{3.75}Ni_{0.25}N$ thin films. This is a confirmation that the Ni atoms preferentially occupy the site I in these thin films both before and after MCP. From the XMCD study of the $Mn_{3.8}Co_{0.2}N$, $Mn_{3.2}Co_{0.8}N$ and $Mn_{2.7}Co_{1.3}N$ thin films it was observed that the sign of all the magnetic moments reversed between Co concentration of x= 0.2 and 0.8 and then again between x = 0.8 and 1.3. Hence, it points to the presence of presumably two MCP at room temperature. This effect is very significant and be very beneficial for applications as it gives a wide window near the compensation point to utilise the unique properties near the compensation points.

Summary

- 10 nm thick $Mn_{3.9}Ni_{0.1}N$ and $Mn_{3.75}Ni_{0.25}N$ thin films and 30 nm thick $Mn_{4-x}Co_xN$ thin films with Co concentrations ranging from x = 0 to 1.3 were grown on $SrTiO_3$ substrates using MBE at 450°C.

- Out-of-plane and in-plane XRD profiles along with super-lattice RHEED pattern confirmed a very nice and epitaxial growth of the $Mn_{4-x}Ni_xN$ and $Mn_{4-x}Co_xN$ thin films. The lattice constant of these thin films were estimated using the peaks obtained from XRD.

- In the case of $Mn_{4-x}Ni_xN$, the saturation magnetization decreases with the increase of Ni concentration. The change of sign of the AHE from negative to positive between x = 0.1 to 0.25 confirmed that the MCP lies somewhere between these points.

- From the XMCD spectra of Mn of , α (sharper, from site I) and β (broader, from site II) absorption peaks showed the anti-parallel alignment between the Mn(I) and Mn(II) atoms for $Mn_{3.9}Ni_{0.1}N$. The sign of the peak in the case of Ni XMCD spectra confirmed the Ni magnetic moment direction to be pointing towards that of Mn(II). This additionally confirms that the Ni atoms have occupied the Mn I sites. The signs of the α and β peaks were reversed along with that of the Ni peak in the case of $Mn_{3.75}Ni_{0.25}N$, thereby confirming that the MCP has been crossed and that the net magnetization now points in the direction of Mn(II).

- For $Mn_{4-x}Co_xN$, the saturation magnetization inherently decreased with an increase in the Co concentration. It is followed then by a sharp rise corresponding to the presence of a MCP near Co concentration of x = 1.1. The reversal of the AHE sign from negative to positive after x = 1.1 confirmed the presence of the MCP around this concentration.

- XAS and XMCD measurements were performed on thin films of $Mn_{4-x}Co_xN$ with Co concentrations x = 0.2, 0.8 and 1.3. From the Mn XMCD spectra a reversal of the α and

β peaks was observed between x = 0.2 and 0.8. A reversal of the A and A' peaks from the Co XMCD spectra was also observed. This reversal of sign confirms the presence of a MCP between the x = 0.2 and 0.8.

- A reversal of sign of the α and β peaks was also observed between x= 0.8 and 1.3 for the Mn XMCD spectra. In the case of the Co XMCD spectra, a combination of the A-A' and B-B' peaks were observed. The B-B' peaks represents the presence of Co in the Mn site II as well. Hence, at this concentration, the Co atoms also occupied site II. A reversal of the Co A-A' peaks was also observed in x = 1.3. The reversal of the Co A-A' peaks along with the reversal of the Mn α and β peaks confirms the presence of another MCP between x = 0.8 and 1.3. This is also visible in the M-H loops and in the change of sign of the AHE angle from negative to positive.

In chapter 2 we had demonstrated that the Mn_4N grown on $SrTiO_3$ substrate has better properties than when it is grown on MgO substrate. In this chapter, we have shown that $Mn_{4-x}Ni_xN$ and $Mn_{4-x}Co_xN$ have the capability of reaching the compensation points at room temperature with substitution of the Mn atoms. In the next chapter, we will focus on the current induced DW motion on $Mn_{4-x}Ni_xN/SrTiO_3$ system.

Chapter

Current Induced Domain Wall Dynamics in Ni substituted Mn_4N

4

> There are two possible outcomes: if the result confirms the hypothesis, then you've made a measurement. If the result is contrary to the hypothesis, then you've made a discovery.
>
> *Enrico Fermi*

In chapter 2, we focused on the current-induced DW dynamics in Mn_4N. In chapter 3, we showed that the MCP could be achieved at room temperature by the substitution of Mn atoms in Mn_4N with Ni and Co atoms where we had estimated that the MCP should lie between the Ni concentration of x= 0.1 and x =0.25. In this chapter, we will focus on current-induced DW dynamics in $Mn_{4-x}Ni_xN/SrTiO_3$ system, close to the MCP. The section 4.1 will firstly describe how the compensation points could be achieved in $Mn_{4-x}Ni_xN$. It is then followed by section 4.2 which focuses on the growth and structural characterization of $Mn_{4-x}Ni_xN$ thin films on $SrTiO_3$ with a wide range of Ni concentration from x=0 to x=0.3. We will then study the global magnetization and transport properties of the $Mn_{4-x}Ni_xN$ thin films, before focusing on the current induced DW motion in $Mn_{4-x}Ni_xN$ thin films. We will then describe the analytical modelling of the DW dynamics in the anti-ferromagnetically coupled $Mn_{4-x}Ni_xN$ thin films. Lastly, in section 4.6, we will focus on ab-intio calculations that allow us to explain our experimental data for $Mn_{4-x}Ni_xN$ thin films before and after the MCP.

4.1 Reaching the compensation points

In several ferrimagnetic compounds, the magnetic and the angular momentum compensation can be achieved by changing either the temperature or the composition of the materials[55, 56, 64]. As mentioned before, this ability of ferrimagnets have made it an active field of research in recent years to study the current induced DW dynamics[58, 59, 63]. Previous experiments have demonstrated that close to the MCP and ACP, large SOT-driven DW velocities could be obtained in ferrimagnets deposited on heavy metals [59, 63]. The ferrimagnets used for those experiments are however made up of rare-earth and critical elements, the two mostly studied

materials being GdCo[59, 62],TbCo[63], GdFeCo[58] and TbFeCo[217].

As seen in chapter 2, we have demonstrated in the rare-earth-free ferrimagnet Mn_4N[86] high DW velocities, reaching more than 900 m/s. With the help of the asymmetric bubble expansion method[206], we have shown that neither bulk or interfacial DMI exists which led us to believe that the DWs are driven by STT. In order to reach closer to the compensation point in this system, Ni can be substituted into the Mn_4N. Ni atoms occupy the Mn corner sites and leads to a reduction of the magnetization. In chapter 3 we have demonstrated that the MCP in this system should lie somewhere between Ni concentration of x = 0.1 and 0.25[119, 136].

Fig.4.1 shows the normalised magnetization as function of the temperature of Mn_4N, $Mn_{3.9}Ni_{0.1}N$ and $Mn_{3.75}Ni_{0.25}N$ thin films. The magnetization increases for Mn_4N and $Mn_{3.9}Ni_{0.1}N$ thin films, while for $Mn_{3.75}Ni_{0.25}N$ it decreases as the temperature is reduced and brought closer to 5 K. The important thing to note here is that in all of the three cases, changing the temperature does not make the system to reach the MCP, even though in the case of $Mn_{3.75}Ni_{0.25}N$ decreases a lot. Hence, MCP cannot be reached at any temperature. However, changing the concentration allows crossing the MCP between $Mn_{3.9}Ni_{0.1}N$ and $Mn_{3.75}Ni_{0.25}N$[136]. Therefore, a fine adjustment of the Ni composition in these thin films is needed in order to reach and study DW motion at the vicinity of the compensation points.

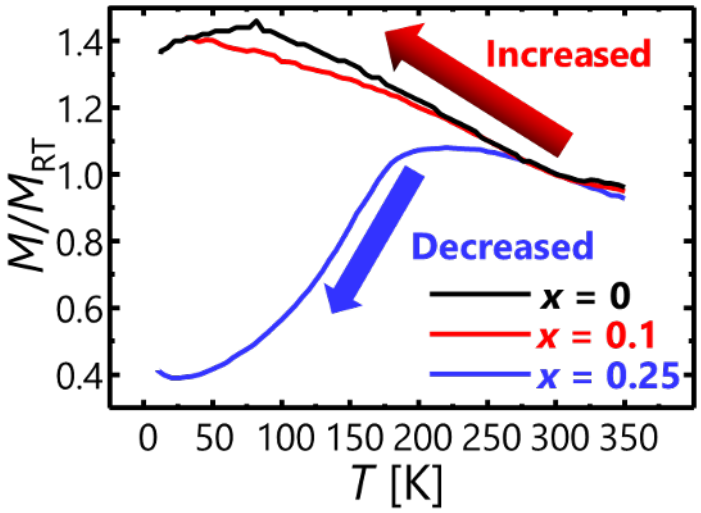

Figure 4.1: *Normalised magnetization as a function of temperature for (black) Mn_4N, (red) $Mn_{3.9}Ni_{0.1}N$ and (blue) $Mn_{3.75}Ni_{0.25}N$. Measurement was performed while applying a field with Field Cooling.*

4.2 Growth and Structural Characterization

For this study, 10 and 30 nm thick layers of $Mn_{4-x}Ni_xN$ with Ni concentrations ranging from x = 0.05 to 0.3 were fabricated, using molecular beam epitaxy at 450°C on 300 μm thick $SrTiO_3$ (001) substrates. The Mn and Ni were obtained from the solid sources of high temperature Knudsen cells while N was incorporated by using a RF-N plasma source. The growth conditions were optimised to be around 1 nm/min with a N_2 gas flow rate of 0.9 cm^3/min at 4.1 $\times$ 10^{-3} Pa chamber pressure. To prevent oxidation of the thin films, a 3 nm layer of SiO_2 was also deposited in-situ on top of the thin films, using a sputtering gun and an Ar plasma gun.

Scanning transmission electron microscopy (STEM), RHEED, XRD measurements were performed to check the crystalline quality of the $Mn_{4-x}Ni_xN$ thin films. Additional XRR

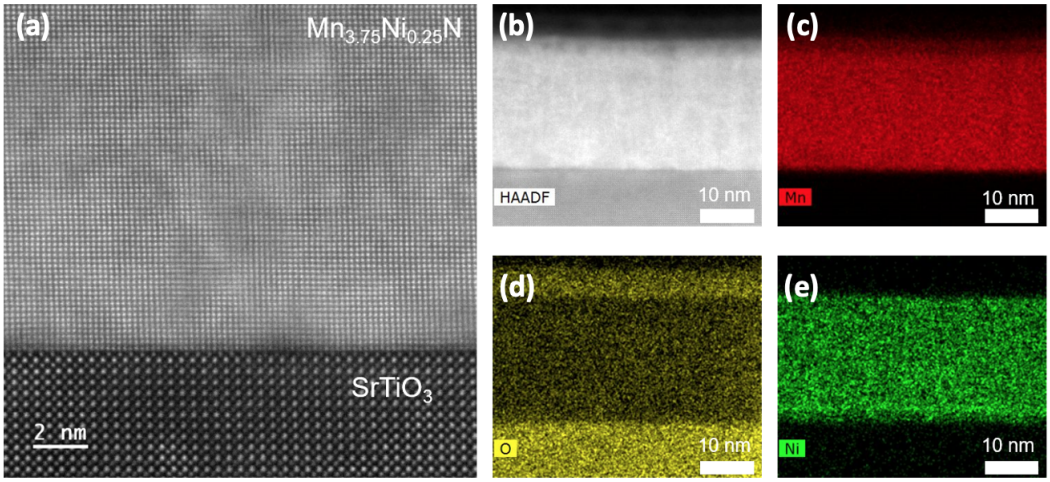

Figure 4.2: *(a) High resolution STEM image of a 30 nm $Mn_{3.75}Ni_{0.25}N$ thin film deposited on a $SrTiO_3$ substrate. (b) HAADF-STEM image of the full thin film with the capping layer of 3 nm of SiO_2 and the associated EDX elemental map of Mn (c), O (d) and Ni (e).*

measurements were also performed to confirm the thickness of the thin films. The characterization and analysis by cross sectional Scanning Transmission Electron Microscopy (STEM) and energy-dispersive X-ray(EDX) was performed by Dr. Hanako Okuno. Fig.4.2 (a) shows the high resolution STEM image of a 30 nm $Mn_{3.75}Ni_{0.25}N$ layer grown on a $SrTiO_3$ substrate. It demonstrates a highly ordered crystalline structure, with a negligible density of defects. A smooth interface between the $Mn_{3.75}Ni_{0.25}N$ and $SrTiO_3$ substrate can also be observed from this image, resulting from a very good lattice matching between the materials. The high-angle annular dark field scanning transmission electron microscopy (HAADF-STEM) image of the full stack with the SiO_2 capping, along with the elemental maps of Mn, O and Ni obtained by EDX are shown in Fig.4.2 (b-e). They show that the Ni is very well and uniformly distributed throughout the thin film. The oxygen is well concentrated in the substrate and the capping layer. However, there is small layer containing oxygen near the interface between $Mn_{3.75}Ni_{0.25}N$ and the capping SiO_2 layer. This Mn-oxide layer has probably to be considered as magnetic dead layer. Its thickness can be obtained from the XRR measurements. XRD peaks for such Mn-oxide peaks were observed earlier in the case of $Mn_{4-x}Ni_xN$ thin films (cf. Fig.3.3 of chapter 3.

The growth technique and parameters are similar to our previously grown thin films of $Mn_{4-x}Ni_xN$ [119, 136]. The STEM images are a testimony of the flawless crystalline quality of these epitaxially grown thin films.

4.3 Magnetization and Transport Measurements

In order to obtain the saturation magnetization of these films, M-H loops were measured using a VSM-SQUID setup at room temperature. Fig.4.3 shows the saturation magnetization as a function of the Ni concentration. As demonstrated earlier in chapter 3, the magnetization in $Mn_{4-x}Ni_xN$ thin films points towards the magnetic moment of Mn site (I) atoms before the MCP and it points towards that of Mn site (II) after the MCP. Therefore the saturation magnetization is shown in a similar way with with the positive saturation magnetization values denoting the thin films before the MCP while negative values denoting the thin films after the MCP in Fig.4.3. Corresponding AHE measurements were performed to estimate whether the

thin films had composition before or after the MCP with negative AHE angle[118, 161, 167] attributed to compositions before the MCP while positive AHE angle[119, 136, 138] attributed to compositions after the MCP as shown in Fig. 4.4.

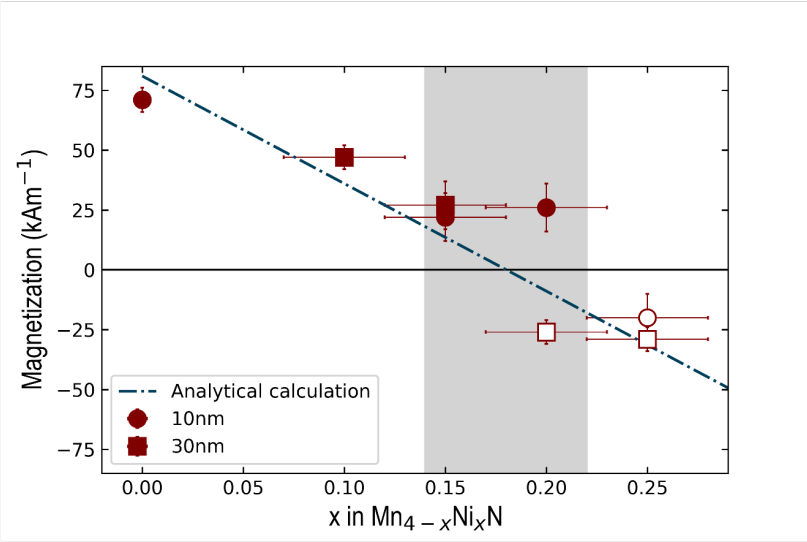

Figure 4.3: *Saturation magnetization as a function of the Ni concentration. The filled symbols represent the magnetization before the compensation point, while the open symbols represent the magnetization after the compensation point. The gray shaded area shows the spread of the observed deviation of the Ni content x at the compensation point with respect to the nominal value. The dotted line represents the magnetization obtained analytically.*

In agreement with our previous results[119, 136], the saturation magnetization is observed to be decreasing when increasing the Ni concentration. There is a change in the direction of the saturation magnetization between x = 0.15 and 0.2. There is a difference in the saturation magnetization observed for x = 0.15 and 0.25 in the 10 and 30 nm thin films. This could be the result of a small deviation of the targeted Ni content, or of the presence of the dead layer.

AHE curves were measured for the $Mn_{4-x}Ni_xN$ thin films, by patterning them into Hall crosses and also by using the Van der Pauw method on blanket layers. Fig.4.4 shows the AHE curves with Ni concentrations (x=0, 0.15, 0.2 and 0.25). The sharp magnetization switching in all the samples is indicative of the retention of the large PMA after patterning. The sign of the Anomalous Hall angle changes between x = 0.15 and 0.25 indicates that the MCP is close to the analytically obtained value of x ≈ 0.18.

Our previous XMCD measurements shown in chapter 3 confirmed that the Ni atoms are occupying the Mn I site, with the magnetic moment pointing towards that of Mn site II atoms[136]. Thus, by increasing the Ni concentration in the system, the saturation magnetization is expected to decrease. After a certain concentration, the sum of the magnetic moments of the Mn site II atoms and Ni site I gets higher than that of the sum of the magnetic moments of the Mn site I atoms. This reverses the saturation magnetization, which then points towards the magnetic moment of the Mn site II atoms, as shown in Fig. 4.5.

The MCP is also estimated to be around Ni concentration of x = 0.18 using analytical calculation using the magnetic moment values obtained though neutron diffraction studies[108, 152], which only corresponds to 3.6% of Ni content. It is interesting to note here that only a very small amount of Ni is actually required to reach the MCP at room temperature.

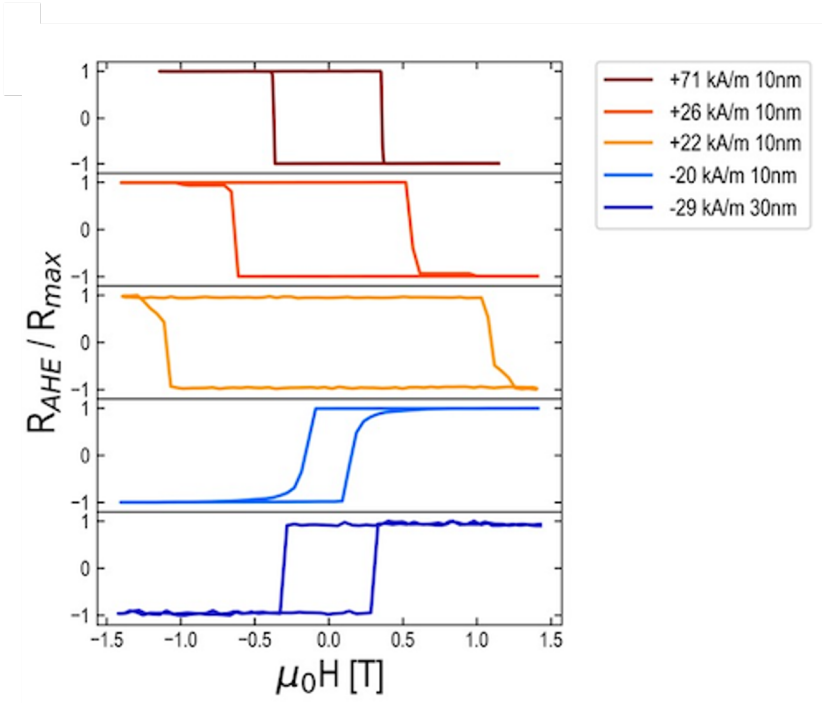

Figure 4.4: *Anomalous hall effect curves measured for thin films with different Ni concentrations (x= 0 (10 nm), 0.15 (10nm), 0.2 (10 nm), 0.25 (10 nm) and 0.25 (30 nm)) The sign of the Anomalous Hall angle changes from negative to positive when crossing the compensation point between x = 0.15 and 0.2. It is also representative of the change of the direction of the net saturation magnetization. The corresponding M_s values of these thin films are shown in the legend.*

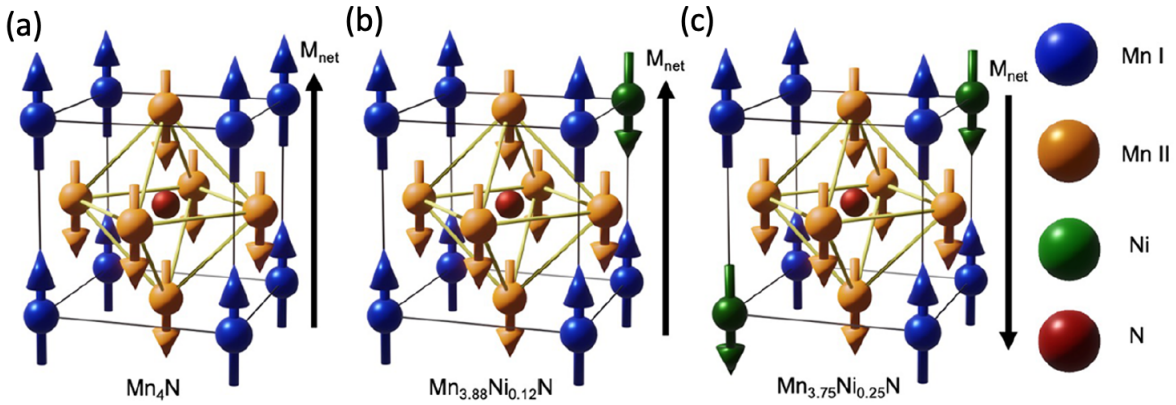

Figure 4.5: *Anti-perovskite crystal structure of (a) Mn_4N, (b) $Mn_{3.88}Ni_{0.12}N$ and (c) $Mn_{3.75}Ni_{0.25}N$, showing the Ni atoms occupying the corner sites and the direction of the spontaneous magnetization reversing after the magnetic compensation point. The blue atoms represent Mn site I atoms, orange Mn site II atoms, green Ni site I atoms and red shows the nitrogen atom at the body centre.*

4.4 Current induced domain wall motion

To study the current induced DW dynamics, 1 μm wide microwires were fabricated using standard e-beam lithography and Ar ion milling (cf. Appendix B). The complete image of the device is shown in Fig.4.6 (a). The DW dynamics was studied using MOKE microscopy, with the help of differential imaging in order to enhance the magnetic contrast.

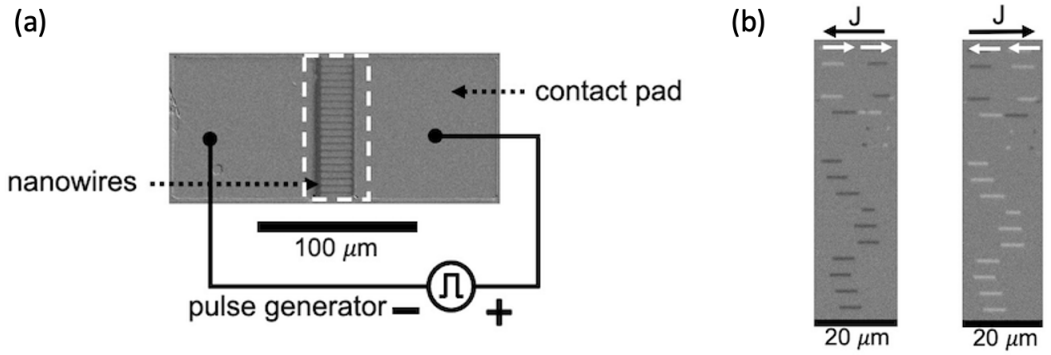

Figure 4.6: *(a) Image of a device used for the study of the domain wall motion. 20 parallel 1 μm wide 20 μm long wires are shown in the image, along with the contact pads from where the DWs injected. (b) Differential polar MOKE images showing the displacement of the domain walls after the application of a negative (left) and a positive (right) current pulses. The white arrows indicate the direction of the motion of domain walls. The device shown here is fabricated on a sample before the compensation point, and the domain walls move in the direction of flow of electrons.*

Out-of-plane magnetic field pulses close to the coercive field of the sample were used to nucleate reversed domains in the nucleation pads and to inject them onto the edges of the multiwires. The DWs were then displaced by the injection of 1-5 ns long current pulses. The shape of the pulses were captured and stored using an oscilloscope. Fig.4.6 (b) are examples of differential MOKE images with black and white contrasts, with displacement of the DWs in the opposite direction for the application of opposite current pulses. As expected, the DWs move in the same direction for a given current polarity. The DW displacements from the different wires were averaged to obtain a precise estimation of the DW velocity. The mean DW velocity is thus obtained by dividing the averaged displacements by the averaged full width half maxima of the pulse widths, taking into account the number of pulses applied. This procedure was performed for all the $Mn_{4-x}Ni_xN$ thin films. For each of the thin films, the DW motion was studied as a function of the current densities. The mean velocities expressed as a function of the current densities, for thin films of different Ni concentrations are shown in Fig.4.7. Here, the velocity curves are shown with respect to the saturation magnetization since it is the key parameter. There was some dispersion found in the nominal compositions which led us to show the velocity with the saturation magnetization rather than the nominal composition.

Current-induced DW velocities below/above the compensation points are shown as positive/negative. As the Ni concentration is increased, the saturation magnetization decreases and the DW velocities are observed to be increasing, with a maximum of 2000 m/s at J = 1.17 $\times$ 10^{12} A/m^2, before the compensation point at 22 kA/m.

Before compensation, a general trend of increase of DW mobility (dv/dj) is observed when getting closer to the MCP (i.e., as the saturation magnetization decreases). Until this point, the DW motion direction is that of the flow of electrons. Intriguingly, after crossing the MCP

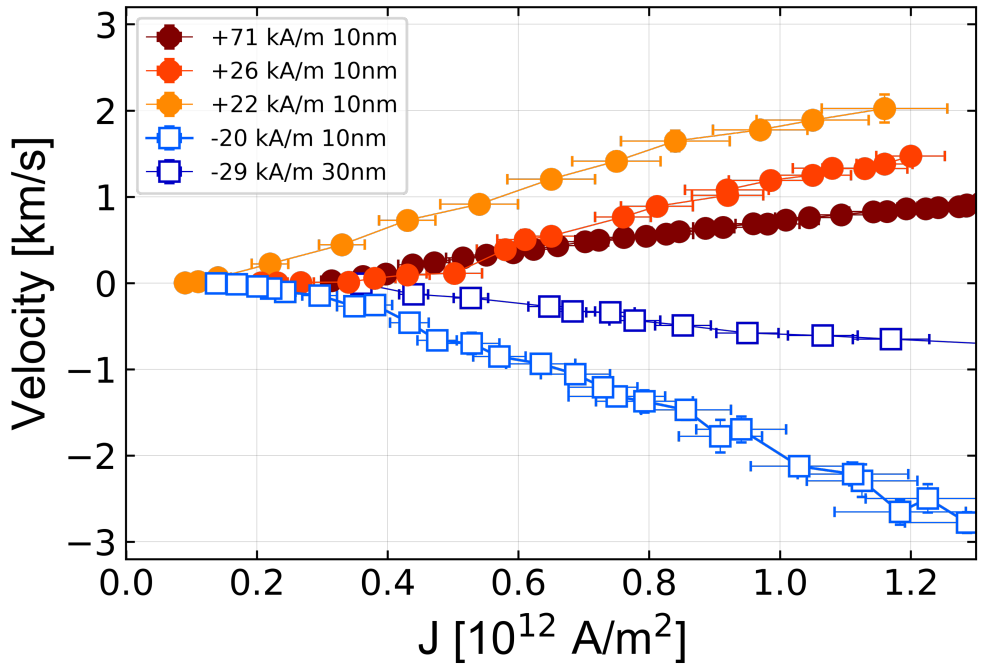

Figure 4.7: *Domain wall velocity plotted against the current density for $Mn_{4-x}Ni_xn$ thin films for Ni concentrations on both sides of the compensation point. Here M_s = 71 kA/m (maroon curve) corresponds to pure Mn_4N with $x = 0$ (Taken from Gushi et al[86]). The filled/open symbols correspond to Ni concentrations below/above the compensation point. The direction of the domain wall motion changes after crossing the magnetic compensation point.*

the DW motion direction is reversed, the DW moving in the direction opposite to the flow of electrons. A very large DW velocity approaching 3000 m/s at J = 1.26 × 10^{12} A/m^2 is obtained for a Ni concentration of x = 0.25 (M_s = -20 kA/m). After the MCP, the DW mobility starts to decrease, with the increase of the saturation magnetization, and eventually reaches similar values to those observed in Mn_4N.

The increase in of the DW velocity close to the compensation point and the subsequent decrease is very similar to that observed for DWs in several ferrimagnetic materials[58, 62, 63]. From Fig.4.7, it can be seen that the threshold current density at which the DWs start to move is very low in these thin films. The lowest threshold current density is close to 0.1 × 10^{12} A/m^2, and is observed for a Ni concentration of x = 0.2 (M_s = 22 kA/m). The DW velocity obtained from the different thin films follow a similar trend starting with the thermally assisted regime followed by the linear regime corresponding the precessional motion of the DW motion driven by STT[191]. Close to the compensation point in the case of Ni concentrations of x = 0.2 (M_s = 22 kA/m) and 0.25 (M_s = -20 kA/m), the thermally assisted regime is extended and the linear appears to start very late as compared to the pure Mn_4N thin film. The threshold current density is also smaller in both samples than for Mn_4N, indicating a very low pinning in these thin films. These threshold current density values are comparable to other metallic ferrimagnets with TbFeCo[196], × 10^{12} A/m^2 for GdCo[62]. It is however much lower than ferrimagnetic insulators such as TmYIG[65] and BiYIG[66].

The DW velocities obtained in these $Mn_{4-x}Ni_xN$ thin films are the highest DW velocities observed until now using STT at room temperature, without the application of an in-plane field.

4.5 Analytical Modelling of the two sub-lattice system

In order to explain these results, and in particular the high DW velocities and the reversal of the DW motion direction, one can use the collective coordinate $q - \phi$ model[58, 60]. The $q - \phi$ was expanded into a ferrimagnetic system with the two sub-lattices "1" and "2" using the effective parameters from the two sub-lattices.

The two sub-lattices of Mn_4N are composed of the same atomic species with two different Mn (I) and Mn (II) atoms. In the case of $Mn_{4-x}Ni_xN$, the amount of Ni atoms replacing the Mn site I corner atoms are at most 5%. As there is no precise measurement of the individual gyromagnetic factors γ, and because of the very small Ni concentration, we will for the sake of simplicity assume that $\gamma_1 = \gamma_2$. This implies that the MCP and the ACP points coincide in this $Mn_{4-x}Ni_xN$ system. Furthermore, due to the strong anti-ferromagnetic coupling in this system we have considered that the damping factors of both the sub-lattices are equals (α_1,α_2) $\alpha_1 = \alpha_2$. Taking this into account in the two sub-lattice model, the DW velocity is in the asymptotic limit of the precessional regime, well above the critical current density(J_C), and given by

$$v = \frac{L_S + L_\alpha \beta}{L_S^2 + L_\alpha^2} L_S u \tag{4.1}$$

where $L_S\mathbf{u}$ = PJh/(2e)$\mathbf{e}_J$, J$\mathbf{e}_J$ is the current density, P=P_1 - P_2 is the effective spin polarization from the two sub-lattices, α is the Gilbert damping parameter, β is the non-adiabatic contribution to the STT, L_s = (M_1 - M_2)/γ is the angular momentum density and L_α = (α/γ)(M_1 + M_2).

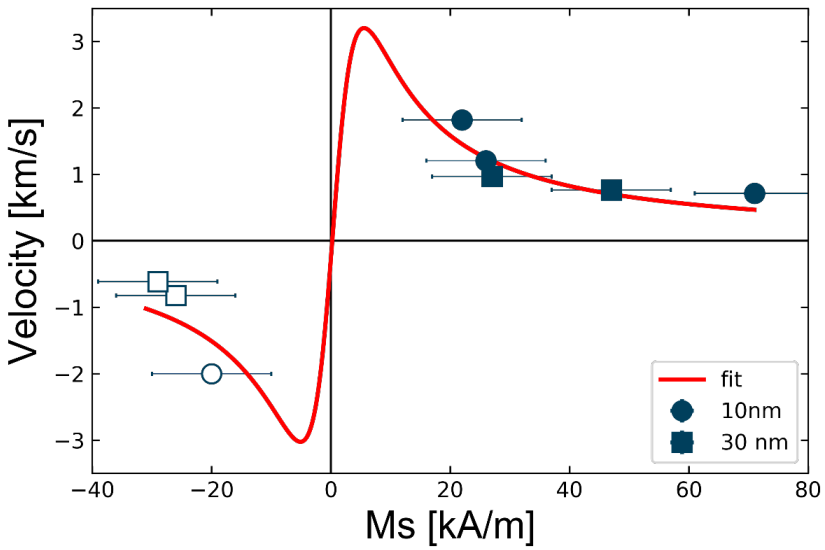

Figure 4.8: *Domain wall velocity versus net magnetization M_s, measured at $J = 1 \times 10^{12}$ A/m^2 (blue circles and squares) compared with the best fit obtained using the $q - \phi$ model from Eq. 4.5.*

In Fig.4.8, the experimental DW velocities at J = 1 × 10^{12} A/m^2 from Fig.4.7 are plotted against the saturation magnetization; M_s = (M_1 - M_2) = γL_s. The best fit of the experimental data by Eq. 4.5 is obtained for P = 0.65, α = 0.013 and β = 0.002. The fit is shown in Fig.4.8 as a red line. Now, taking the $q - \phi$ model into consideration, the DW motion direction reversal is expected to occur at L_s = -βL_α, just below the ACP. Indeed, in the Fig.4.7 curve, the velocity

vanishes just below the experimental MCP. This result validates our assumption that $\gamma_1 = \gamma_2$, and therefore that the MCP and the ACP coincide in this system.

These results show that the large STT driven DW velocity is due to the mobility increase when approaching the ACP, together with the large spin polarization of the conduction electrons in this system. The reversal of the DW motion direction is also predicted by the analytical $q - \phi$ model. It assumes that the sign of the spin polarization P does not change with the angular momentum density L_s. The reversal of the DW motion direction is therefore related to the relative change of the net spin polarization with respect to the angular momentum after crossing the ACP. In other words, after crossing the ACP, the spin polarization P acts as an effective negative spin polarization.

4.6 AB-initio calculations and analysis

In order to confirm the assumption that the spin polarization remains in the same direction after crossing the ACP/MCP, ab-initio band structure calculations have been performed by Dr. Ali Hallal from SPINTEC. These first principle calculations were performed in the framework of Density Functional Theory (DFT) using spin polarized relativistic Korringa-Kohn-Rostoker (SPR-KKR) and Vienna ab-initio simulation packages (VASP) [218–226]. VASP was used for structure optimization, with the electron-core interactions being described by the projector augmented wave method for the potentials and the exchange correlated energy calculated within the Generalised Gradient Approximation (GGA) of the Perdew-Burke-Ernzerhof form[222, 223]. The cutoff energies for the plane wave basis set which were used to expand the Kohn-Sham orbitals were 500 eV for all the calculations. Structural relaxations along with the total energy calculations were performed while making sure that the Hellmann-Feynman forces acting on ions were less than 10^{-2} N. The calculations for Mn_4N were based on the perovskite crystal structure ($Pm\bar{3}m$ space group). A bulk lattice constant of 3.74 Å was taken, with a collinear configuration after full relaxation using a mesh of $44 \times 44 \times 44$ $Å^{-1}$ as shown in Fig. 4.5 (a). The total calculated magnetic moment was found to be 1 μ_B (Mn I, 3.3 μ_B and Mn II, -0.8 μ_B) along the [001] quantization axis, which is in good agreement with the previous calculations[163, 227]. The substitution of Ni in this system was tackled by using the supercell approach where the Mn I was replaced by Ni in $1 \times 1 \times 4$ and $1 \times 1 \times 8$ unit cells for modelling the Ni concentrations of x = 0.125 and 0.25. In order to verify the supercell approach, the effect of the Ni substitution in $Mn_{4-x}Ni_xN$ was calculated using the coherent potential approximation (CPA) which is implemented in the SPR-KKR code[224–226].

Figure 4.9 (a) shows the total calculated magnetic moment as a function of the Ni concentration. One observes a similar trend of decrease of the magnetization with an increase in the Ni concentration, followed by the MCP, which occurs at x = 0.15 using the SPR-KKR approach (green) and at x = 0.17 using the VASP approach (orange). These calculated total magnetic moments match very well with our experimental data, the experimental MCP being at x = 0.18. The transport properties and spin polarization can be estimated from studying the s-orbitals of materials which are responsible for electron transport. The s-orbital projected density of states(PDOS) of the Mn(I) and Mn(II) atoms for Mn_4N are presented in Fig.4.9 (b,c). The calculated polarization is "up"(towards the Mn(I) magnetic moment, also taken as the global quantization axis here) at the Fermi level for both Mn(I) and Mn(II) atoms, with the polarization of Mn(II) being one order of magnitude higher than that of Mn(I). This is an evidence that in this system the electron transport is taking place through the Mn(II) atoms rather than through the Mn(I) atoms.

Fig.4.9 (d,e,f) shows the s-orbital PDOS of $Mn_{3.75}Ni_{0.25}N$, whose concentration lies after the

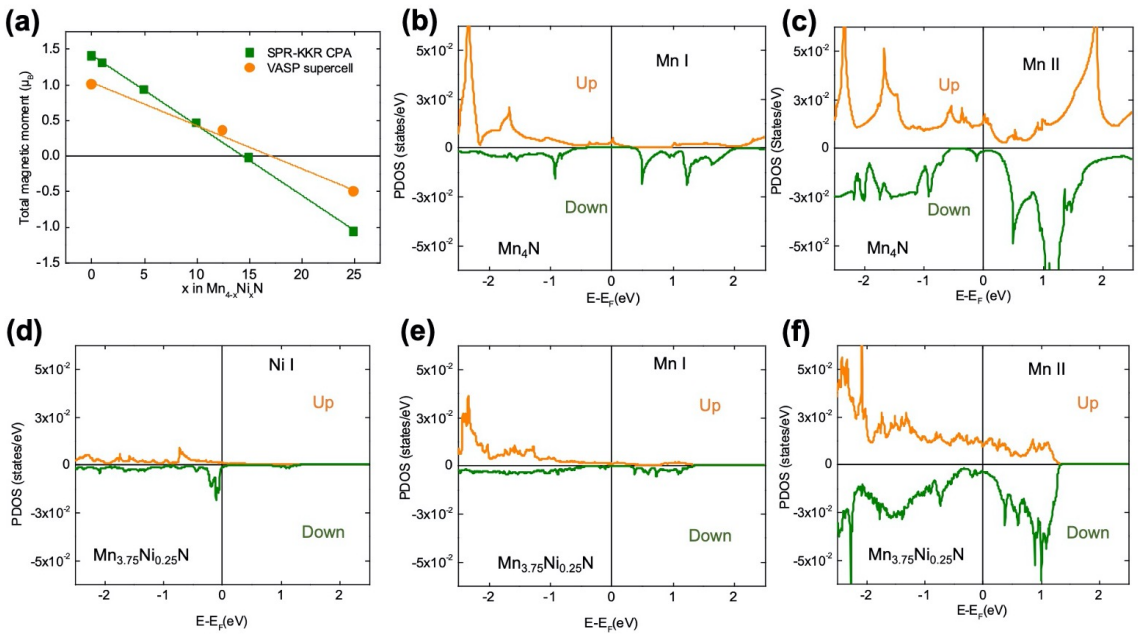

Figure 4.9: *(a) Ab-initio calculations of the net magnetic moment as a function of the Ni concentration showing that the MCP is at x=0.15 for the SPR-KKR CPA approach (green) and at x= 0.17 for the VASP approach (orange) (b,c) s orbital PDOS of Mn(I) and Mn(II) of Mn_4N. (d,e,f) s-orbital PDOS of Ni(I), Mn(I) and Mn (II) atoms. Here, UP represents the direction of the magnetic moment of Mn (I) and DOWN represents the direction of the magnetic moment of Mn(II).*

MCP. A closer look at the Fermi level unveils that the polarization in here also lies towards the magnetic moment of Mn(I) for Ni, Mn(I) and Mn(II) atoms. Also, the PDOS is again one order of magnitude higher for Mn(II) than for Mn(I) and Ni(I). Therefore, the transport is dominated by electrons carrying spins parallel to the global quantization axis. The ab-initio calculations show that the spin polarization direction remains in the direction of the magnetic moment of Mn(I) before and after the ACP. Hence, these calculations allows explaining our experimental results, in agreement with the predictions made by the $q - \phi$ model.

Summary

To sum up, current induced DW dynamics was investigated on ferrimagnetic $Mn_{4-x}Ni_xN$ thin films, while tuning the Ni concentration to reach the magnetic and angular momentum compensation points.

- 10 and 30 nm thin layers of ferrimagnetic $Mn_{4-x}Ni_xN$ were grown epitaxially on $SrTiO_3$ substrates.
- RHEED, XRD and STEM characterizations confirmed the good crystalline quality of the samples. A smooth interface between the $SrTiO_3$ substrate and $Mn_{3.75}Ni_{0.25}N$ was observed by STEM. An EDX characterization confirmed that Ni was uniformly and homogeneously present throughout the thin film.
- The magnetization of the thin films decreased when increasing the Ni concentration, as expected, and then changes direction after a certain Ni concentration.

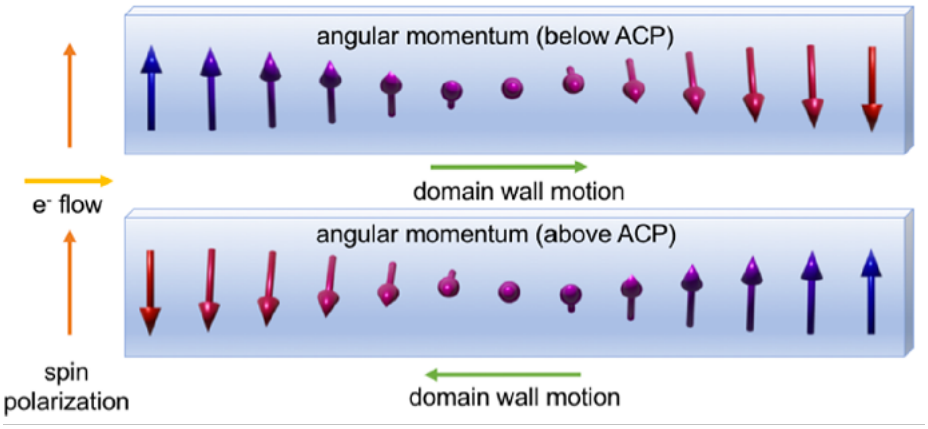

Figure 4.10: *Sketch of the Bloch domain wall with the individual net magnetic moments, for the thin film below (top) and above (bottom) the ACP. The orange arrow indicates the spin polarization direction, which remains in the same direction both below and above the ACP. The yellow arrow represents the direction of the electron flow. As the spin polarization direction remains the same after the ACP, while the net angular momentum changes direction, the STT drives the domain walls in the opposite direction above the ACP.*

- The switch of the AHE angle from negative to positive confirmed the crossing of the MCP with increasing the Ni concentration. With the help of the AHE curves, of M_s measurement and of an analytical calculation of the saturation magnetization, the MCP was estimated to be around a Ni concentration x = 0.18.
- With the increase in the Ni concentration towards the MCP, the DW velocities increase. A velocity of more than 2000 m/s was obtained before the MCP.
- After crossing the MCP, the DW motion direction was observed, along with a very high DW velocity approaching 3000 m/s at the vicinity of the MCP.
- Analytical model based on the collective coordinate approach ($q-\phi$) can be used to predict the high DW wall velocities, using a two sub-lattice model with effective parameters.
- Two assumptions were taken for the analytical model; i) As both the sub-lattices contain Mn atoms and the percentage of Ni in the system is very low, the magnetic and the angular momentum compensation point was considered to be coinciding with an effective gyromagnetic ratio $\gamma = \gamma_1 = \gamma_2$ ii) the spin polarization direction must remain constant before and after the MCP.
- The best fitting of the $q-\phi$ model was obtained which matched very well with the experimental DW velocities confirming the first assumption of the MCP and ACP coinciding in this system.
- Ab-initio calculations were performed using the VASP and SPR-KKR approach for $Mn_{4-x}Ni_xN$ thin films. Both of these approaches confirmed the presence of a MCP for x = 0.15 and 0.17, which is very close to our experimentally obtained MCP concentration of x = 0.18.
- The s-orbital PDOS shows that the electron transport is due to Mn (II) atoms, with a one order higher DOS at the Fermi level in Mn_4N. The spin polarization direction was also observed towards the global quantization axis [001] (parallel to the magnetic moment of Mn(I)).

- From the s-orbital PDOS of $Mn_{3.75}Ni_{0.25}N$ it was observed that the DOS is one order of magnitude higher at the Fermi level for Mn (II) than for Mn (I) and Ni(I). Interestingly, the spin polarization direction also remained towards the global quantization axis [001]. This is a confirmation of our second assumption.
- The results of the ab-initio calculations along with the predictions of the $q - \phi$ model explain the high DW velocity and the reversal of the DW motion direction in these $Mn_{4-x}Ni_xN$ thin films.

In this chapter we have explained the effect of current on the DW dynamics of $Mn_{4-x}Ni_xN$. Beyond the record velocities, We have shown a good convergence between the experimental and the theoretical results, explaining how and why the dynamics changes before and after the compensation points. In the next chapter, we will focus on the study of the Anomalous Hall Effect on Mn_4N and $Mn_{4-x}Ni_xN$ thin films.

Chapter

5

Perspectives for Mn_4N

> Anyone who has never made a mistake
> has never tried anything new
>
> *Albert Einstein*

This chapter will focus on perspectives involving Mn_4N thin films. In section 5.1 we will discuss on the study of SOT switching in Mn_4N. The following section 5.2 will focus on the study of DW based logic devices using Mn_4N.

5.1 Spin orbit torque switching in Mn_4N

Bilayers consisting of a heavy metal layer and a ferromagnetic layer combine several interesting features which have made them the archetypal system for spinorbitronics. Their geometry breaks the structural inversion symmetry, allowing the generation of SOTs generated by SHE in the bulk of the heavy metals, and/or by the Rashba Edelstein effect at the interface. The large spin orbit coupling of the heavy metals can also lead to a large interfacial Dzyaloshinskii-Moriya interaction (DMI)[192, 228]. This leads to several interesting micromagnetic configurations such as Néel domains[28, 206] or exotic spin textures such as skyrmions[193], merons[229], which can be manipulated using SOTs[41, 50].

In this section, we will focus on the SOT driven magnetization switching. The SOT switching of ferromagnets was first demonstrated by Miron *et al.*[230] and Liu *et al.*[231]. In the last decade, it has become a well studied phenomenon, even leading to the development of the SOT-MRAM[232]. In SOT switching, the spin polarization of the electrons is achieved thanks to the heavy metal layer and to its interface with the ferro or ferri magnetic thin film. It is due to the interfacial Rashba-Edelstein effect[47, 48] and the bulk spin hall effect[44–46]. This spin polarization leads to a spin accumulation at the interface, which diffuses into the magnetic layer. This exerts two different torques on the magnetization, known as the *Anti-damping* and the *Field-like* torques[41, 233]. These spin orbit torques can lead to the deterministic switching of the magnetization, providing that a small in-plane magnetic field is applied to break the symmetry[233].

Ferrimagnetic/heavy metals bilayers have been studied in the last few years, exhibiting similar interfacial effects, and improved properties with respect to Ferromagnetic/heavy metals

bilayers. In particular, faster DW motion[58, 66], smaller skyrmions[59] and SOT switching[62] have been observed when using ferrimagnets. In the case of ferrimagnets, the magnetization dynamics dominate over that of the ferromagnetic materials. This is due to the lower saturation magnetization and faster dynamics close to the ACP. Zheng *et al* demonstrated field free switching with multi-layers of CoTb with different concentration resulting in gradient DMI[234]. It is very interesting to note here that they not only demonstrated field free switching but also gradient DMI which is another feature in case of ferrimagnets. In this context, Mn_4N is perfectly suitable for SOT switching with its fast dynamics at room temperature which has been demonstrated by Gushi *et al*[86]. It also has the advantage of reaching the compensation points at room temperature either by substitution by Ni or by Co, thus making it viable for technological integration.

5.1.1 Growth and Characterization

In order to study the effects of the SOTs in heavy metal/ferrimagnetic Mn_4N bilayers, Tungsten (W) and Platinum (Pt) heavy metals deposited on top of the Mn_4N layers are used both as capping and SOT layer. 7 nm thick Mn_4N layers were grown on $SrTiO_3$ substrates at 450°C, using the growth parameters shown in Appendix A. 5 nm thick W and 2 nm thick Pt layers were then deposited on top of the Mn_4N layers.

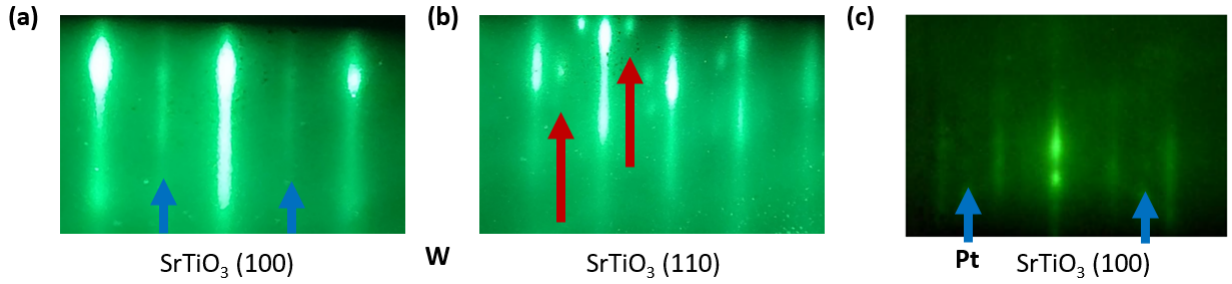

Figure 5.1: *RHEED patterns of (a) $W/Mn_4N/SrTiO_3$ for the $SrTiO_3$ (100) direction, with blue arrows showing the super-lattice diffraction lines, thus confirming the epitaxial growth, and (b) for the $SrTiO_3$ (110) directions. Red arrows indicate Kikuchi lines, which are indicative of kinks and steps on the $SrTiO_3$ surface. (c) RHEED patterns of Pt/Mn_4N for the $SrTiO_3$ (100) direction. The blue arrows indicate similar super-lattice patterns*

Structural Characterization

Fig.5.1 shows the RHEED images taken after the growth of the 7 nm Mn_4N layer and before the deposition of the W layer. The Mn_4N (001) reflections (streaks) are shown in Fig.5.1 (a) and the $SrTiO_3$ (100) reflections are shown in (b). The blue arrows point towards the supperlattice diffraction streaks which are attributed to the body centre Nitrogen atoms. These well separated RHEED patterns, along with the superlattice diffraction patterns, are a confirmation of a very good epitaxial growth of the thin films. However, the red arrows point towards satellite patterns next to the main $SrTiO_3$ diffraction lines. These are known as Kikuchi lines, and are attributed to the roughness of the surface[235, 236]. The roughness in this system could be coming from the roughness of the substrate. Another reason for the observation of these Kikuchi lines could be that, the film being thin, the defects close to the substrate are revealed. Fig. 5.1 (c) shows the RHEED pattern of a Pt/Mn_4N sample. These also have a similar superlattice diffraction patterns indicated by the blue arrows.

Magnetic Characterization

In this subsection, we will discuss the magnetic properties obtained from SQUID and magneto-transport measurements before moving on to SOT switching in subsection 5.1.2.

Saturation magnetization

A SQUID setup was used to measure the M-H curves in these thin films, in order to extract the saturation magnetization. Fig. 5.2 shows the M-H curves of the (a) W/Mn_4N and (b) Pt/Mn_4N thin films. The M-H loops are not square hysteresis curves, the signal corresponding to the sum of the contributions of two different phases. The reversal of the magnetically hard phase can be seen at higher magnetic fields, while that of the soft phase appears near zero field. Such a small coercivity seems to be coming from the artifacts.

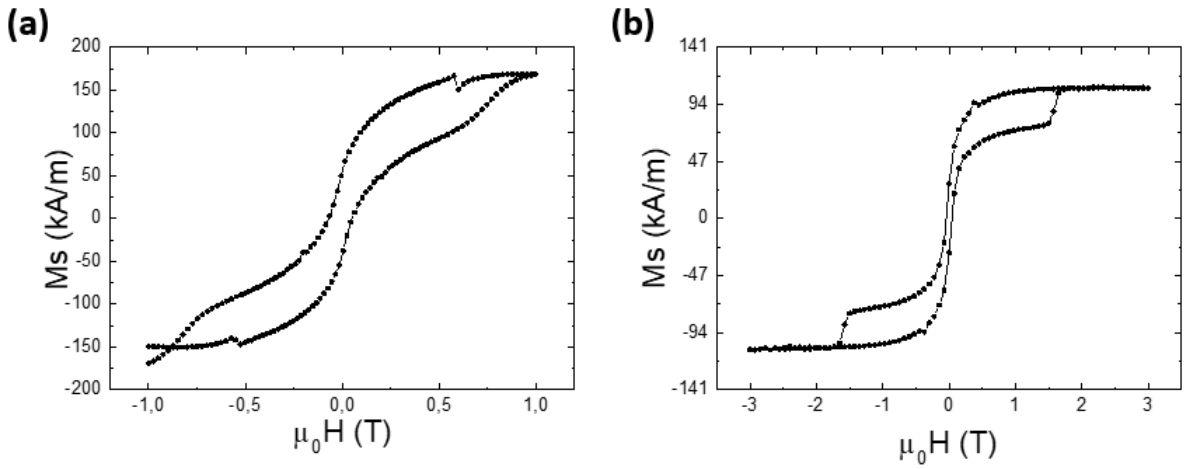

Figure 5.2: *M-H loops of (a) W/Mn_4N and (b) Pt/Mn_4N samples*

The saturation magnetization extracted from these curves are 160 kA/m for the W/Mn_4N sample and the 105 kA/m for the Pt/Mn_4N sample. Such saturation magnetization values have been reported before Mn_4N. However, they are much higher and hence differ from the saturation magnetization values from our previous work[86, 129]. From the unusual shapes of the saturation magnetization hysteresis curves, it becomes very clear that they are coming from the soft phase artifacts. After removing the soft phase from the curves, saturation magnetization of 60 $\pm$ 15 for W/Mn_4N and 34 $\pm$ 5 for Pt/Mn_4N were extracted. One possible explanation for these artifacts and the soft phase could be presence of ferromagnetic impurities in the $SrTiO_3$ substrate[211].

Magneto-transport measurement

Magneto-transport measurements were performed on the Pt/Mn_4N and W/Mn_4N samples using the Van der Pauw method. These measurements were performed using a PPMS setup (cf. Appendix A). Fig.5.3 (a) and (b) shows the AHE curves of the W/Mn_4N and Pt/Mn_4N thin films. Both the AHE curves show a negative AHE angle similarly to what has been observed in single Mn_4N layers. An important point to note here is that the AHE curves are very different from the M-H curves presented in Fig.5.2. The soft phase which can be seen in the M-H curves are not present in these curves. Hence, we can observe the real coercivity of these 7 nm thin films. These AHE curves therefore confirm the anomalous M-H curves are indeed coming from artifacts possibly originating from the ferromagnetic contamination of the $SrTiO_3$ substrate [211].

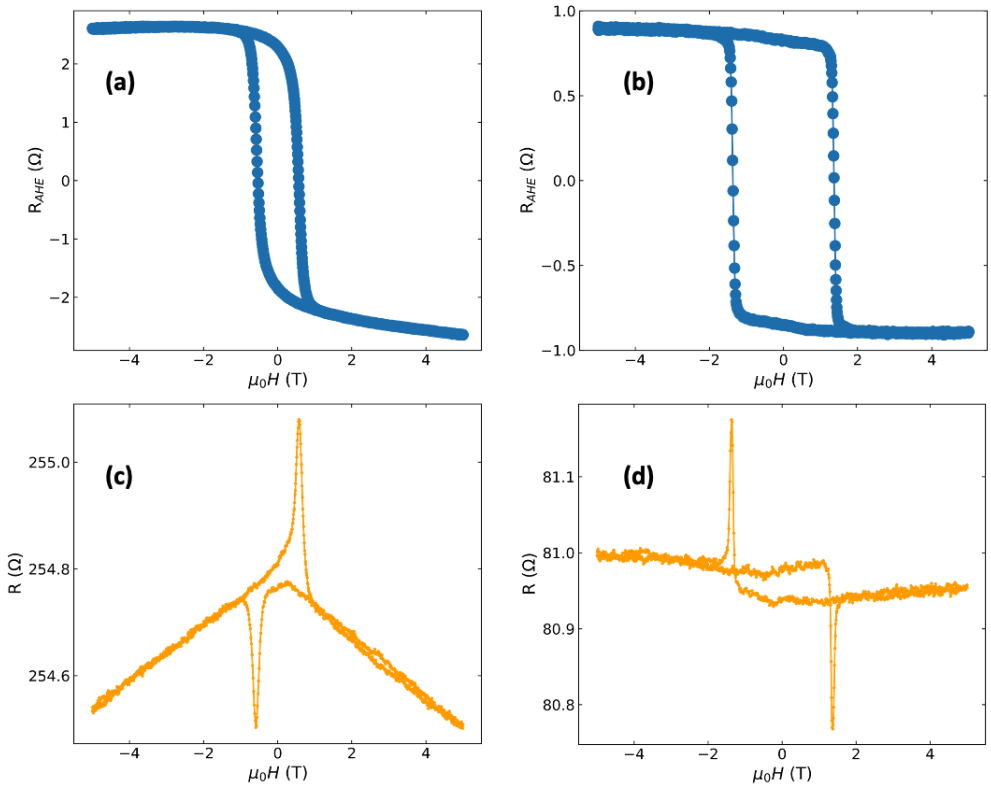

Figure 5.3: *AHE curves of (a) W/Mn_4N and (b) Pt/Mn_4N. Longitudinal resistance curves of (c) W/Mn_4N and (d) Pt/Mn_4N.*

The coercivity of the W/Mn_4N sample is much smaller (0.55 T) than that of the Pt/Mn_4N which (1.37 T). At this stage it is unclear why these coercivity are so different, as the thicknesses of the Mn_4N layers are the same (7nm). The deposits were made using the same growth conditions, but not at the same time, which could for instance lead to variations in extrinsic defects concentration. For thicknesses below 10 nm, it looks like the magnetic properties are not always reproducible. Also, there might be different DMI and/or anisotropy interfacial contributions, but this cannot be evidenced at this stage. The resistance for the Pt capped sample seems to be much lower than that of W/Mn_4N sample. This could be due to shunting of the current through the Pt, as the resistivity of Pt is much lower than that of β-W and varies between 25-100 µΩcm[237, 238] in thin films.

The longitudinal resistances curves are plotted in Fig.5.3 (a) for W/Mn_4N sample and (b) for the Pt/Mn_4N sample. In these curves, the asymmetric peaks correspond to the magnetization switching and probably coming from AHE contribution from the contacts[239]. For the W/Mn_4N sample, we observe a slope at high field in these curves which is due to the contribution of magnons to the resistance, the MMR [239]. It is unclear for now why this contribution is not observed in the Pt/Mn_4N sample, it might be due to the electrical shunting by the Pt layer. Indeed, the calculated average resistivity of the stacks are 398 µΩcm for the W/Mn_4N sample and 113 µΩcm for the Pt/Mn_4N sample, which indicates that for the Pt/Mn_4N sample the Pt layer acts as an electrical shunt. Resistance variations at low fields could arise from AMR [240, 241], DW resistance [241, 242], but one would expect this contribution to be even in field, whereas here the low-field peaks are odd in field. This rather points towards a contribution of the AHE to the resistance measurement, as previously observed in perpendicularly magnetized system [239].

Overall, the magneto-transport measurements provide a clearer picture of the hysteresis

than the M-H curves. The large resistivity value of W/Mn_4N sample suggests that the W could be in the β phase[243, 244]. Also, an increase of the resistivity of the Mn_4N layer could be due to the thickness decrease to 7 nm.

5.1.2 SOT switching measurement and Analysis

In this subsection, we will first briefly discuss the device fabrication. We will then present our first results of SOT switching without an in-plane field, and then results on SOT switching without and with an in-plane field.

Device Fabrication

Using ion beam lithography and Ar milling, 1, 2 and 3 μm wide and 10μm long microwires and hall bar structures were fabricated (cf. Appendix B). A thick layer of around 100 nm of Au-Ti was deposited on the big nucleation pads. This reduces the distance between the two contacts hence we only get the resistance from the wires. The wires are designed in a way to get closer to the 50 Ω output impedance to match the input impedance of the devices to the output impedance of the voltage source to transmit high frequency signals. It is particularly necessary here as in the case of W/Mn_4N the resistivities are high.

SOT Switching without In-Plane Field

For detecting the SOT switching, we used the polar-MOKE microscopy setup shown in the previous chapters 2 and 4 for DW motion. W/Mn_4N sample was glued on the sample holder and the microstrip (similar to those used for DW motion) devices were wirebonded and connected to the power supply, with an oscilloscope to record the shape of the pulse. Out-of-plane magnetic field pulses higher than the coercive field of 0.55 T were applied to saturate the magnetization of the samples in one direction. After the saturation, current pulses with a pulse width of 1-3 ns were applied to the device.

Fig.5.4 shows the differential images of 3 µm wide and 10 µm long nanowires taken by MOKE microscopy. The images on the left in Fig. 5.4 (a,c,e,g) have been taken after full saturation of the magnetization, using out-of-plane magnetic field pulses. The white and the black indicates the different magnetization directions, the white corresponding to a magnetization pointing up, and the black pointing down. The images on the right in Fig.5.4 are taken after the application of 2 current pulses with a pulse width of 2.98 ns and a current density between 0.9 - 0.95 $\times$ 10^{12} A/m^2. No external fields were applied during the application of these current pulses. The switching of the magnetization here is characterized by the change of the color from white (black) to black (white). As seen in the images on the right, the magnetization seems to be switching. However, the switching is only observed in the wires, and not on the whole structure. This could be expected as the current density is higher only on the wires and not on the pads.

Now, let us look into the behaviour of the switching. The magnetization switching was only observed at high current densities, above 0.8 $\times$ 10^{12} A/m^2, and it was only observed for pulse lengths of 2.8 ns or longer.

Two important observations can be made from these measurements.

1) It is possible to saturate in the up state, and then to switch to the down state, or the contrary.

2) This switching occurs for either a positive or a negative current pulse, whatever the initial magnetization direction. This suggests that the switching is not due to Oersted field, but rather to Joule heating and/or spin torques.

3) The switching occurs only once. Further application of pulses do not allow switching it back and forth, neither with an opposite polarity current pulses, nor with higher current densities or wider pulse widths.

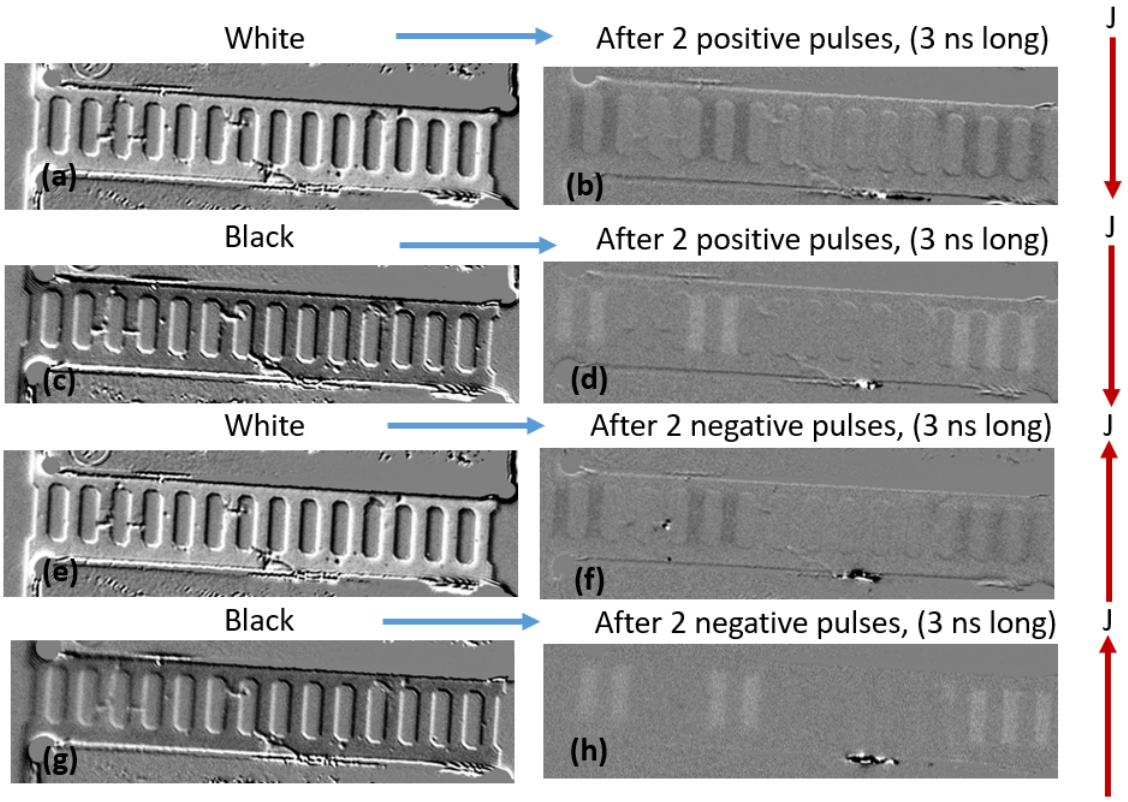

Figure 5.4: *Differential MOKE images of devices on W capped Mn_4N thin films, fully saturated (a,c,e,f), and after the application of a train of 2 positive and negative 3 ns pulses (b,d,f,h) The white and black colour shows here again the direction of the magnetization.*

However, if saturated again using a magnetic field, the switching using a current pulse can be performed again. The origin of this behaviour is yet unclear, it suggests that the magnetization state after saturating the magnetization in the up state or after switching from down to up are different. The contrast seen in Fig.5.4 could correspond to a demagnetized state, but the contrast remains large, close to that observed in between up and down domains. Such a demagnetization could be expected in absence of an external in-plane field to break the symmetry between the Anti-damping like SOT and the magnetization direction[41, 230, 245].

Although this experiment shows that a switching can be induced, it is not possible to switch repeatedly back and forth, and the contributions of Joule heating and of spin torques are unclear. Note that in the case of SOT switching without an external field, the symmetry between the AD Torque and the magnetization state is not broken. The switching is then usually random, even though it is possible to switch back and forth[41, 233]. The fact that we do not retrieve this behaviour in these preliminary experiments is not clear for now. It could be due to heating, to specificities of the STT and of SOTs in our devices. Some other phenomena could come into play: for instance, Yang *et al* [246] demonstrated magnetic switching in a 5 µm ferrimagnetic Pt/GdFeCo bar with 10 ps electrical current pulse. The current density they used for this switching is very high of 2×10^{13} A/m^2. They claim that the switching is due to heating effect in GdFeCo very similar to all-optical switching along with the SOC effect of Pt with GdFeCo.

SOT Switching with an In-Plane Field

The usual way to obtain a reproducible back-and-forth switching using SOTs is usually to apply an additional in-plane field [230, 231]. To probe the effect of such a field in our system, an additional in-plane oriented magnet was installed to provide a constant magnetic field. At first, the device was fully saturated in one direction (up or down), as done previously, with the help of out-of-plane magnetic field pulses higher than the coercive field of the sample.

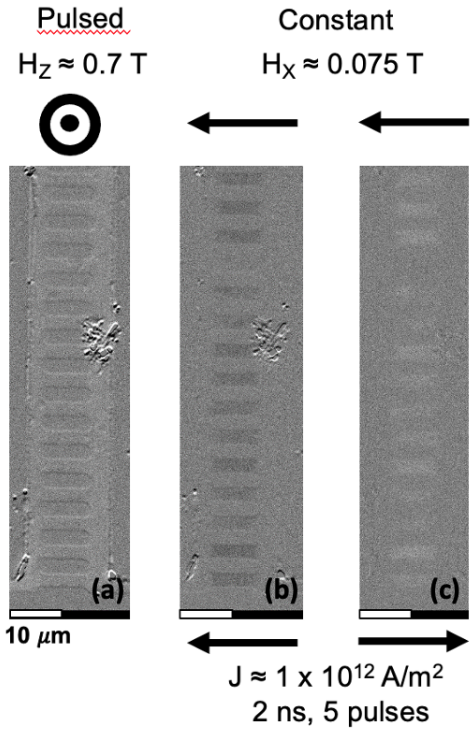

Figure 5.5: *Differential MOKE images of devices on W/Mn_4N thin films (a) fully saturated white contrast (b) black contrast in the wires after the application of a positive current pulse and of a DC in-plane field (c) white contrast after application of a negative current pulse with the same in-plane field*

The saturated magnetization in one direction is seen as the white contrast in Fig.5.5 (a). Now, in presence of an in-plane field, a train of 5 pulses were injected into the device, with a delay of 1 ms between the pulses. Magnetization switching was observed for a current pulse widths of 2 ns, a current density of 1×10^{12} A/m^2, and an in-plane field of 75 mT. This can be seen in Fig.5.5 (b) and (c) where the contrast first changes from white to black and then to white again when current pulses with an opposite polarity were applied to the device. This back and forth switching has been done more than 20 times using pulses. No DW motion was observed in our measurements. This suggests that the switching occurs through semi-coherent magnetization reversal rather than by nucleation and DW propagation. A partial switching was observed in this system when a lower pulse width and a lower in-plane magnetic fields were applied. However, no switching was observed below a current density of $J = 0.85 \times 10^{12}$ A/m^2. Another thing to note here is that that the switching was only observed when 3 or more pulses were applied. A single shot switching with a single current pulse was not observed.

We did not have time yet to make a complete set of experiments that would allow a fruitful analysis. In particular, we need to study the dependence of the switching with the current polarity, the amplitude of the in-plane field, the number of pulses, their length, etc. We also have to check for the reproducibility of the phenomenon and the endurance of these devices.

Among the numerous questions opened by these first results are the role and amplitude of the DMI, and the respective roles of the SOT and STT in this system.

To perform these experiments, we plan to use magnetotransport measurements in Hall crosses[230], which are more convenient than MOKE measurements made here in nanowires originally designed to study DW motion. Nonetheless, these results already show that Mn_4N is an interesting candidate for studying macrospin switching by SOTs. In particular the probable SOT switching occurs here for current pulses as short as 2 ns, much shorter than those used in other studies based on ferrimagnets (e.g. Pt/GdFeCo[247], Pt/CoGd[62]). However, Cai *et al.* showed that the switching occurs around 0.4 ns for Pt/CoGd with a switching probability of 90% albeit almost using double the magnitude of the in-plane field as ours and similar current density. These results can also be compared to a recent work on switching on a 20 nm thick Pt/Mn_4N system, where Bai *et al*[248] showed magnetization switching with a lower current density and a lower in-plane field but a current pulse width of 0.5 ms. They claim this to be the result of bulk like SOT in Mn_4N which have been reported for other systems like CoTb[249]. It is also interesting to note that current driven magnetization switching was demonstrated in non-collinear 111 oriented Mn_4N by Isogami et al recently[158], where they observed the magnetization switching by giving an in-plane current without any SOT layer. In this case, the in-plane current provides a torque for the magnetization switching.

5.2 Domain-wall based logic devices

In this section, we will focus on DW-based logic devices. This work was done in collaboration with Dr. Eline Raymenants and Dr. Van Dai Nguyen from IMEC, Belgium. Information can be stored using magnetic domains, which can be moved by STT and/or SOT along a track[36]. These tracks can be made into arbitrary shapes which can enable performing logic operations. Logic operations using DW motion has been first demonstrated by Allwood *et al*[19], where they had demonstrated a ferromagnetic NOT gate operation and a shift register using field driven DW motion using a specific shape of the DW track. Several DW-based logic concepts have been proposed in the last two decades[21, 38, 250–254]. A review of DW-based logic devices has been proposed by Raymenants *et al.* in Ref[255].

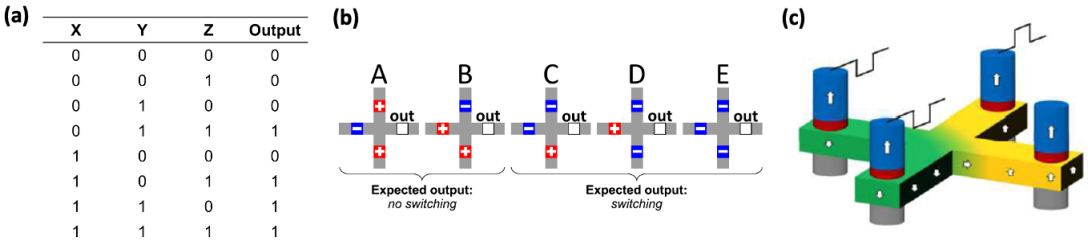

Figure 5.6: *(a) Majority gate truth table (b) Schematic of the top view of the cross Spin Torque Majority Gate devices showing the expected switching or absence of switching depending on the inputs (Taken from Vaysset et al [256]) (c) 3D schematic of the cross STMG showing the connected free layer with the MTJ pillars on the four corners of the cross. Taken from Raymenants et al[255]*

Here, we have focused on a concept proposed by Nikonov *et al*[250] called the Spin-Torque Majority Gate (STMG). The majority gate works with three input and one output, instead of the normal two inputs and 1 output which are being used. Fig.5.6 (a) shows the truth table of a majority gate where X, Y and Z denote the three inputs. The output depends on the

majority input with two cases. First, If all three inputs have the same input, the output would be the same. Second, if two out of three inputs are the same; then the output will be the same as the two similar inputs. Fig.5.6 (b) shows the top view of the schematic of how majority can be implemented using MTJs and DW tracks. These crosses are made up of extended free layer from the 4 MTJs which are shown here as the squares. Out of the four squares, the one on the right is taken as the output, while the ones on the left are used as the input for the majority gate. Here 0 and 1 are high and low resistance states, based on the direction of the magnetization of the free layer. The idea here is to nucleate under the MTJ a DW, using a high current density pulse through the MTJ [257]. This DW can then be moved by applying current pulses from the different arms of the crosses. If only one DW moves, it will get pinned at the cross. However, when the there are two or more DWs at the cross, they should propagate towards the output MTJ. Once the combined DW reaches the output MTJ, it switches the free layer, which can be then be read using using TMR.

Fig.5.6 (c) shows the 3D schematic of the cross shape with the MTJs on the edges of the crosses. Any logic operation can be performed by using the inverters and three inputs of the majority gates[258]. Other key features of this concepts are non-volatility through bi-stable states, expected compact circuits, low power spin manipulation and continuous connections through potential high speed and high density spintronic devices[256]. The STMG concept has been studied extensively by simulations and have to shown to be working very well. However, there has not been a full experimental demonstration of this concept yet.

As Mn_4N exhibits a high efficiency for STT-induced DW motion, our goal was to develop a STMG based on this material.

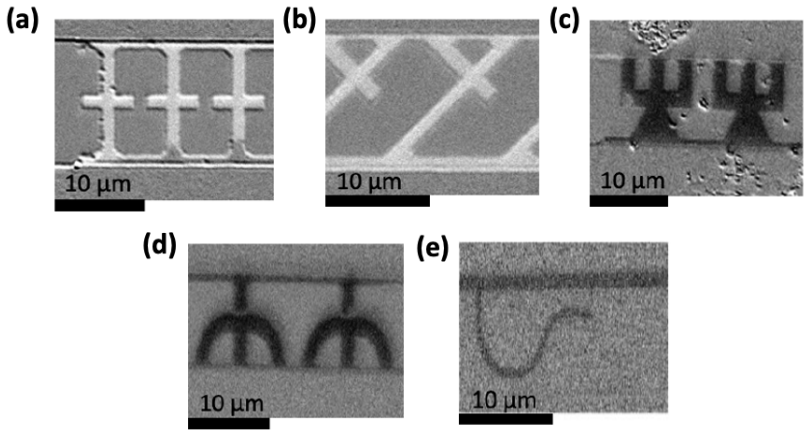

Figure 5.7: *Differential MOKE images of device with different geometries: (a) cross (b) two inputs (c) three inputs with curved tracks (d) three inputs with bigger output (e) flexible S shaped track*

In order to develop the first steps of a STMG, varying DW track shapes with different number of inputs were designed with Dr. Eline Raymenants. These devices were then fabricated on a 10 nm thick Mn_4N layer capped with SiO_2, with two contacts pads on either side of the devices(cf. Appendix B). The MOKE microscopy setup was used to nucleate and move the DWs in these devices similarly to what was shown in the chapter 2 and 4. Straight microwires were also fabricated to measure the DW velocity. These devices are shown in Fig.5.7.

This preliminary study allowed us to get insights concerning the development of STMGs. Designs have to be made keeping in mind resistance of the device so that enough current density could be supplied to move the DWs in a reproducible way without adding up to any heating effects. Therefore the lengths and width of the devices are very critical along with the

shape. In the test geometry used here the current density was higher at the output cross as compared to the input cross. This led to heating and nucleation of the DW along along with edge of the output tracks. It also led to the breakdown of several devices. If the road towards a full functional STMG remains long, these first results nonetheless show that it it possible to manipulate DWs in Mn_4N using complex geometries.

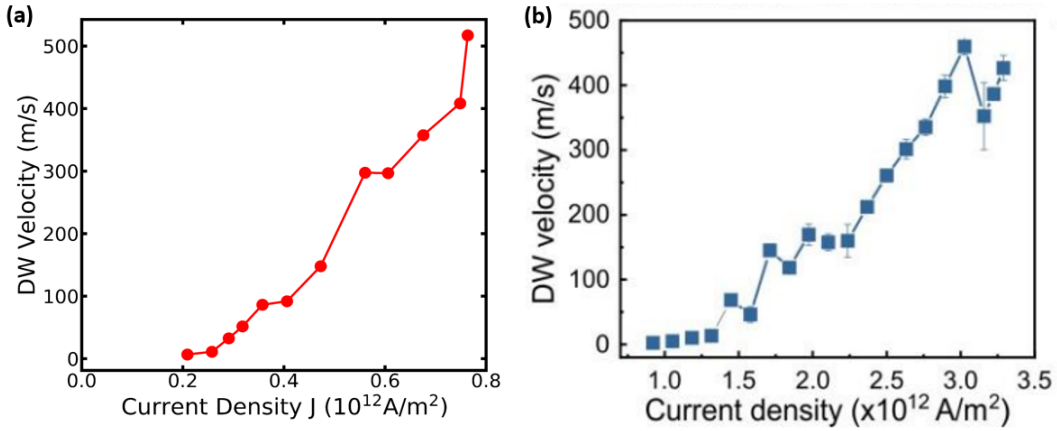

Figure 5.8: *DW velocity curves of (a) STT driven 10 nm Mn_4N (b)SOT driven SAF Taken from the supplementary information of Raymenants et al.[253]*

The velocities obtained from these devices were exactly similar to our previous work [86] as shown in Fig.5.8 (a). This result also showcases the reproducibility of the DW velocity in Mn_4N. If we compare the DW velocity in Mn_4N with the DW velocity in the SAF shown in Fig.5.8 (b), similar velocities can be obtained in Mn_4N for a five times lower current density. Furthermore, Mn_4N also provides a wide window of operation for the DW velocity in which the DW moves in the flow regime. Overall, the study of these complex shaped tracks in Mn_4N helped us identifying the different challenges related to the design of the STMG, and showcased the advantages of using ferrimagnetic Mn_4N for such devices. Following these preliminary results, new designs are under development at IMEC, with the aim of realizing the STMG functionality.

Summary

To summarize, in this chapter preliminary studies on SOT switching on Mn_4N and DW based logic devices was presented.

- Possible SOT Switching without an in-plane field was observed on W/Mn_4N when a current pulses (pulse width of 3ns) higher than J = 0.8×10^{12} A/m^2.
- This switching was observed only once. The possible switching could be due to Joule heating or sample being demagnetized.
- Back and forth magnetization switching was observed when current pulses J $\sim 1 \times 10^{12}$ A/m^2 (pulse width of 2ns) were applied in the presence of in-plane fields $H_x \sim 75$ mT.
- Possible deterministic SOT switching was observed with the in-plane field. However, further experiments are required to demonstrate this effect clearly and to explore the role of SOT, STT and DMI in this system.

- Different shaped tracks were fabricated to study the STMG concept for DW logic. This study has allowed us with helpful insights to design and develop such DW logic devices.
- From this study we have got a better understanding of the STMG working concept and have also showed that effectiveness of using ferrimagnets such as Mn_4N for DW based logic applications.

In this chapter, we have shown that indeed Mn_4N could be used for and a lot of different studies ranging from spin textures to switching and logic applications. With this we move on to the conclusion of this thesis.

Conclusion

The main results presented in this thesis are related to domain wall dynamics in Mn_4N and $Mn_{4-x}Ni_xN$ thin films.

Chapter 1 focused on ferrimagnetic materials for spintronics, and introduced fundamental mechanisms linked to the current induced domain wall motion in these systems. In chapter 2, an overview of Mn_4N was presented, with a focus on the growth and characterization of Mn_4N samples deposited on MgO and $SrTiO_3$ substrates. From this study it was discovered that Mn_4N grown on $SrTiO_3$ is more preferable for domain wall motion, due to the presence of large domains with a small density of pinning sites. This result can be attributed to the good lattice matching between the $SrTiO_3$ substrate and Mn_4N. In the second part of chapter 2, we demonstrated very high domain wall velocities, of up to 900 m/s, in $Mn_4N/SrTiO_3$. This can be explained with the help of micromagnetic simulations, by taking into account the low saturation magnetization and the high spin polarization of this system.

In chapter 3, we established that $Mn_4N/SrTiO_3$ samples reach the compensation point at room temperature using Mn substitution by Ni or Co. For $Mn_{4-x}Ni_xN/SrTiO_3$, we showed that the magnetic compensation point lies between a Ni concentration of x = 0.1 and x = 0.25. From the XMCD measurements, we determined that the Ni atoms replaced the Mn site I corner atoms, with the magnetic moment of Ni pointing towards that of Mn site II face-centered atoms. In the case of $Mn_{4-x}Co_xN/SrTiO_3$, we observed the interesting possibility of having two compensation points, the first one between Co concentrations x = 0.2 and x = 0.8, and the second one between x = 0.8 and x = 1.3. This was observed by combining magnetization saturation, AHE angle reversal and XMCD measurements. XMCD measurements showed that the Co replaces the Mn site I atoms for $Mn_{3.2}Co_{0.8}N$ which was expected. The net magnetization points towards the magnetic moment of the Mn site I atoms. For $Mn_{3.2}Co_{0.8}N$, we observed more Co atoms replacing the Mn site I atoms. Here, the net magnetization points towards the magnetic moment of Mn site II atoms. Hence, indicating a compensation point between Co concentrations of x = 0.2 and x = 0.8. Interestingly, in the case of $Mn_{1.3}Co_{2.7}N$ we noticed that Co atoms not only occupy the Mn corner site I atoms but also the Mn site II atoms, with the magnetic moment in the direction of Mn site I. Here, the net magnetization is again towards the magnetic moment of Mn site I atoms. Hence, from this we concluded that the there are two compensation points, between Co concentrations of x = 0.2 and x= 0.8.

In chapter 4, $Mn_{4-x}Ni_xN/SrTiO_3$ samples were fabricated with varying Ni concentrations, in order to reach the compensation points at room temperature. Domain wall motion measurements were then performed on these samples. Here, we achieved a very high domain wall velocity of more than 2000 m/s just before the magnetic compensation point, and an even higher velocity approaching 3000 m/s after the compensation point. A reversal of the domain wall motion direction was also observed after the compensation point. To explain the high domain wall velocities, an assumption was taken that in the case of $Mn_{4-x}Ni_xN$, the MCP coincides with the ACP. Using this assumption, analytical calculations were performed. The DW velocity obtained from these calculations were in agreement with our experimental results.

It also indicated that the in order to have a reversal of the DW motion direction, the spin polarization direction has to remain the same even after the crossing the MCP/ACP. Ab-initio calculations were performed using VASP and SPRKKR approach. It was observed from both the approaches that the MCP in $Mn_{4-x}Ni_xN$ with Ni concentrations which were close to our experimental results. From the s-orbital PDOS for $Mn_{4-x}Ni_xN$ before and after the MCP, it was confirmed that the spin polarization remains in the same direction before and after the MCP. These calculations further justified our assumptions and helped explain the reversal of DW motion after the MCP.

Chapter 5 focused on the some of the ongoing work related to Mn_4N. In the first part, we showed a preliminary study showing possible SOT switching on Mn_4N/W sample, with and without an external in-plane field. In the following part, we showed preliminary work done on the realization of STMG concept using Mn_4N. Devices with different shapes and different number of inputs and outputs were fabricated on $Mn_4N/SrTiO_3$ and studied using MOKE microscopy. By showing the possibility to displace DWs in complex wire shapes, this study lays the first bricks towards the development of a STMG in Mn_4N.

Contributions

During the course of my joint PhD program between Université Grenoble Alpes and University of Tsukuba, I have studied and performed various systems and experimental techniques, in three different Institutions, namely SPINTEC and Institut Néel in Grenoble, and University of Tsukuba. I have learnt thin films growth techniques by MBE, along with XRD and XRR measurements, at University of Tsukuba, on Mn_4N and $Mn_{4-x}Ni_xN$. I have performed the optimization of $Mn_{4-x}Ni_xN$ thin films to reach the compensation point. I have been trained on the MBE setup by Taro Komori, Taku Hirose, Haruka Mitarai and Prof. Takashi Suemasu. The growth is an essential part of this thesis, involved in all Chapters 2,3,4 and 5. I have been trained on MOKE microscopy by Dr. Jose Peña Garcia, Dr. Jan Vogel and Dr. Stefania Pizzini at Institut Néel. I have performed the imaging of the domains for DW motion which is shown in Chapter 4 and 5. I have been trained on Nanofabrication by Dr. Laurent Vila and other staff at the clean room at SPINTEC and performed the device fabrication for domain wall motion and magneto-transport measurements shown in chapter 2,4 and 5. I have been trained to perform the magneto-transport measurements by Dr. Laurent Vila and Dr. Jean-Philippe Attané at SPINTEC. I have performed the magneto-transport measurements of the Mn_4N and $Mn_{4-x}Ni_xN$ thin films and of the devices shown in Chapter 2, 3, 4 and 5. I have also performed measurements using VSM, trained by Isabelle Joumard of SPINTEC, and SQUID, trained by Jean-Francois Jacquot of CEA.

Apart from this, I discussed the micromagnetic simulations performed by Dr. Jose Peña Garcia. The growth of the thin films in Chapter 2 were performed by Dr. Toshiki Gushi and were part of his PhD. I participated to the measurements and to the results discussion.

The band structure and transport characteristics in Mn_4N and $Mn_{4-x}Ni_xN$ have been obtained in collaboration with Dr. Ali Hallal and Prof. Mairbek Chshiev of SPINTEC, who performed the ab-initio calculations. The $Mn_{4-x}Co_xN$ thin films were grown by Haruka Mitarai, and the subsequent XMCD measurements were performed by Haruka Mitarai, Taro Komori and Prof. Takashi Suemasu. Although I was not able to perform the XMCD measurements myself, I participated to the interpretation of the experimental results.

Finally, the MFM microscopy on W/Mn_4N samples was performed in collaboration with Dr. Van Tuong Pham, with discussions with Dr. Olivier Boulle and Dr. Stefania Pizzini to study the presence of skyrmions in this system.

The devices for DW logic were designed by Dr. Eline Raymenants of Imec in Belgium and Dr. Van Dai Nguyen. Discussions with Dr. Kevin Garello helped to move forward with the study of SOT Switching in W/Mn_4N.

Dr. Laurent Vila, Dr. Jean-Philippe Attané, Prof. Takashi Suemasu, Dr. Stefania Pizzini and other colleagues and researchers at SPINTEC, Institut Néel and University of Tsukuba have immensely helped and guided me in this endeavour. The various studies, experimental techniques and numerous discussions during my PhD have benefited me in advancing my knowledge in experimental physics.

Output of this work

Several parts of this thesis have already been published:

- The part of the work presented in Chapter 2 about Domain wall motion in Mn_4N has been published in ACS Nano Letters[86].
- The study of $Mn_{4-x}Co_xN$ showing two different compensation points which is presented in Chapter 3 has been published in published in Physical Review Materials[138].
- The work on current induced domain wall motion presented in Chapter 4 has been published in ACS Nano Letters[129].

I also took part, as co-author, to several studies that are not detailed in this thesis:

- I have helped Dr. Eline Raymenants in the design, nanofabrication and testing of new tracks for DW logic. This work was part of the main work published in IEEE International Electronic Devices Meeting (IEDM) 2021[255].
- I have taken part in discussions on the results and analysis of the effect of doping in Mn_4N and its subsequent Ferrimagnetic to Ferromagnetic transition. This work has been published in Journal of Physics D: Applied Physics[135].

Apart from this, I have performed with Taro Komori AHE measurements on Mn_4N and $Mn_{4-x}Ni_xN$ thin films. From our analysis to de-convolute the different interactions contributing to the AHE, it appears that the reason for the high AHE angle in Mn_4N and $Mn_{4-x}Ni_xN$ of 2%, and of the reversal of the AHE angle at low temperatures, is the role of phonons in this system. Results from ab-initio calculations matches well with our experimental results. This work is still in progress.

I have also been part of an ongoing study on the presence of skyrmions in W/Mn_4N and Pt/Mn_4N with Dr. Van Tuong, Dr. Olivier Boulle and Dr. Stefania Pizzini.

Outlook

I hope that the work presented in this thesis has showcased the fascinating properties of Mn_4N, $Mn_{4-x}Ni_xN$ and $Mn_{4-x}Co_xN$. We have shown domain wall velocities comparable to those obtained in SOT systems, whereas there is here only STT, at room temperature and without the need for an external in-plane field. We have also shown that Mn_4N could be used as potential candidate for DW logic and SOT switching. There are several other potential spintronics applications where the fast dynamics of Mn_4N could be used or prove to be highly beneficial.

The absence of rare-earth is also an asset for the integration with what could become the next generation of greener and cheaper alternatives or complements to the CMOS technology.

Nonetheless, in order to justify as a potential candidate in spintronics, this material must be implemented in MTJs. MTJs have indeed become the backbone of spintronics, from sensors to STT oscillators and MRAMs. Hence, there is a continuous effort towards the improvement of MTJs, with a focus on the materials used for the magnetic layers and the tunneling barrier[17]. In this context, ferrimagnets can be an interesting choice to develop MTJs, as their much lower magnetization could reduce the stray fields and hence could allow a higher density of devices. Also, the lower magnetization and faster dynamics[259] could help lowering the switching current densities. For instance, Kaiser *et al*[260] had demonstrated a high negative TMR of -90% using ferrimagnetic CoFe/CoFe-Gd for the free layers. In regards to Rare-earth free nitrides, Narahara *et al*[84] had demonstrated a MTJ structure using a ferromagnetic Fe_4N/MgO/Fe_4N stack. Here, Fe_4N has the same anti-perovskite crystal structure as Mn_4N. Mn_4N being a ferrimagnet with an anti-perovskite crystal structure, it is worth trying to develop Mn_4N based MTJs. Ultrafast spin dynamics[129], high spin polarization[86], PMA from crystalline anisotropy along with high thermal stability[118] makes Mn_4N a suitable candidate, which could be used in MTJs both as a free layer and reference layer.

If MTJs based on Mn_4N are realized, they can be applied to Spin Torque Nano Oscillators (STNO) as well. STNOs are nanoscale pillars made of MTJs[261]. In the case of STNOs, the spin polarized current is used to induce oscillations of the magnetization of the free layer, rather than magnetization switching. The oscillation frequencies depend on the properties of the free layer and could range from hundreds of MHz to several tens of GHz. These oscillations can then be converted into voltage signals using the MTJs magneto-resistance.

In this context, Mn_4N could be used as the oscillating free layer in STNOs. Mn_4N has an estimated resonant frequency higher than 70 GHz at zero field. This high resonant frequency originates from the large anisotropy of Mn_4N and from a small saturation magnetization. Present STNOs can go up to tens of GHz frequency range. However, it was demonstrated by Tsunegi *et al*[262] that by using a layer of MnGa under the oscillator layer, the frequency could be increased to up to 70 GHz at 2 T. Similarly, it was shown that in the optical mode the MnGa could reach up to sub-THz 150 GHz due to its large anisotropy[263]. With Mn_4N as the oscillating layer, we can reach this sub-THz regime at zero field. The present state of the art in telecommunications industry is the 5G technology, which operates with a bandwidth up to 54 GHz. Using Mn_4N could help increasing the frequency of operation upto 100 GHz, enabling the next generation of devices in the telecommunication industry with much faster data transfer rates.

With the potential to be used in spintronics for DW or SOT devices, STT-MRAM, SOT-MRAM or oscillators, Mn_4N could become the next years a new member of the magnetic materials family for spintronics.

Acknowledgement

Firstly, I am extremely indebted to my parents who have supported and guided me in life to follow my passion. Without their never-ending support, this PhD would not have been possible. You have been a pillar of my constant support. I thank you very much for everything.

I am very fortunate to having worked with fantastic team of supervisors at University of Grenoble, France and University of Tsukuba, Japan. My experiences and learnings in last 3 years have helped me appreciate the hardships and become more patient and adjusting. I would like to express my sincere gratitude towards my supervisor Laurent who helped and guided me in both my day to day work and personally. I will always cherish our time profoundly at the lab and outside at various meetings and conferences. I deeply thank Jean-philippe for being the guiding light and steer me in the right direction in my PhD whenever I felt a bit lost. I am thankful to you for patiently teaching me the art of skiing in the beautiful French Alps. Last but not the least, I am extremely grateful to Prof. Suemasu for immense help in the lab and making my life in Japan feel like a walk in the park. I am still looking forward to playing table tennis with you when I return to Japan.

I would like to immensely thank Stefania Pizzini for her expert guidance and support with the measurements at Institut Neel and key teachings of the subject matter. My PhD would not have been completed without your help and guidance. I also want to thank Jan Vogel for his impeccable insights and guidance for the PhD work.

Special thanks to Mair and Ali for their help with the computational work and sharing their insights without which our work could not have been well explained. I would also like to thank Asst. Prof. Toko for not only helping and guiding me at the lab at University of Tsukuba, but also showing me the spiciest Ramen shop there.

I would like to thank Olivier and Tuong for their advice and guidance on the study of skyrmions. I want to thank Dai and Eline for helping with the development of domain wall based logic devices. It was also amazing to share the office with Eline and have stimulating discussions.

Words are going to fall short for thanking my fellow labmates with whom I have had fantastic discussions and spent wonderful time in the last 4 years. I want to thank Jose and Aymen for helping me whenever I was stuck at the MOKE setup at Insitut Neel and our long coffee sessions discussing physics, life and more. I would love to thank Paul and Nicolas for helping me settle in the lab upon arrival and having infinite interesting discourse. I wish to thank Yu Fu for being like an older sister to me and having amazing lunch-time conversations and also for the delicious hot pots. I want to thank Maxen for all the discussions and setups during the covid times and after work as well. I would love to thank Sara for being an amazing friend and for countless discussions. I want to thank Cecile for helping me at the magneto-transport setups and providing me guidance. I want to thank Ryuhei for being there whenever I needed any support and having amazing chats both in and outside the lab. I would also like to thank Salvatore, Paolo and Aurelie for having very good times both in and outside the lab. I would also especially like to thank Ariel who has been so kind to me and have always helped out in

the lab. This PhD would not have been completed without your crucial help.

Now coming to my fellow labmates at Tsukuba, I would like to firstly thank Taro who helped, guided and supervised me throughout my stay in Tsukuba. I want to thank Taku and Haruka for helping me at the lab and having great discussions and conversations at lunch. I want to thank Yudai and Xi for really helping me learn all the bureaucracy and culture in Japan. I want to thank Takuma for being a great friend and having interesting conversations. I would also like to say thanks to all the other students in the Suemasu lab, all of you were very kind, inviting and helpful to me. I will always remember our ski trip, gyoza party and trips to Ramen shops. Lastly, I wish to thank Toshiki who gave great insights and advice on my PhD work which helped me extensively.

I want to thank Ahmed and Philippe from the rf group with whom I had amazing brainstorming sessions and discussions. They helped me understand the working of STNOs and Neural networks. I want to thank Lucian, Gilles and Olivier for being part of my CSI. They have been very kind to me and have always given me great advice. I want to thank Marco, Daniel, Alvaro, Olivier, Stefan and Nuno from MRAM group for having amazing times in Grenoble. I want to thank Rafael, Micheal, Laura, Kaushik, Arijit and Kevin for having great discussions and having a good time in SPINTEC and Grenoble. I want to specially thank my friends in Grenoble Louis, Namanu, Sameer, Ranjana, Valid, Martin and Lucila for being there after work and supporting me through the PhD. I particularly want to thank Mahima who supported me throughout my writing process and helped me push through the end.

I would really like to thank Liliana, Prof. Mangin, Prof. Otani, Prof. Mitani, Prof. Kuroda, Prof. Yanagihara, Prof. Ohno and Stefania for being a part of my jury committee. I thank them for being very thorough and asking very interesting questions to me for my PhD.

I thank IDEX for the funding of my PHD (IDEX-DOMINO) in France and University of Tsukuba for the funding in Japan.

Bibliography

1. Mocuta, A. *et al. Enabling CMOS Scaling Towards 3nm and Beyond* in *2018 IEEE Symposium on VLSI Technology* 2018 IEEE Symposium on VLSI Technology (IEEE, Honolulu, HI, June 2018), 147–148.
2. Moore, G. E. Cramming more components onto integrated circuits. **38,** 6 (1965).
3. Sánchez-Sinencio, E. & Andreas G, A. Low-voltage/low-power integrated circuits and systems: low-voltage mixed-signal circuits. *Wiley-IEEE Press* **4** (1999).
4. Vidal, J. *'Tsunami of data' could consume one fifth of global electricity by 2025* Climate Home News. Section: Energy. https://www.climatechangenews.com/2017/12/11/tsunami-data-consume-one-fifth-global-electricity-2025/ (2021).
5. *Beyond CMOS - IEEE International Roadmap for Devices and Systems* (IEEE, 2018).
6. Baibich, M. N. *et al.* Giant Magnetoresistance of (001)Fe/(001)Cr Magnetic Superlattices. *Physical Review Letters* **61,** 2472–2475 (Nov. 21, 1988).
7. Binasch, G., Grünberg, P., Saurenbach, F. & Zinn, W. Enhanced magnetoresistance in layered magnetic structures with antiferromagnetic interlayer exchange. *Physical Review B* **39,** 4828–4830 (Mar. 1, 1989).
8. Youssef, J. B. *et al.* Correlation of GMR with texture and interfacial roughness in optimized rf sputtering deposited Co/Cu multilayers. *Journal of Magnetism and Magnetic Materials* **165,** 288–291 (Jan. 1997).
9. Bowen, M. *et al.* Nearly total spin polarization in La2/3Sr1/3MnO3 from tunneling experiments. *Applied Physics Letters* **82,** 233–235 (Jan. 13, 2003).
10. Ikeda, S. *et al.* Tunnel magnetoresistance of 604% at 300K by suppression of Ta diffusion in CoFeBMgOCoFeB pseudo-spin-valves annealed at high temperature. *Applied Physics Letters* **93,** 082508 (Aug. 25, 2008).
11. Julliere, M. Tunneling between ferromagnetic films. *Physics Letters A* **54,** 225–226 (Sept. 1975).
12. Miyazaki, T. & Tezuka, N. Giant magnetic tunneling effect in Fe/AlzO3/Fejunction. *Journal of Magnetism and Magnetic Materials,* 4 (1995).
13. Moodera, J. S., Kinder, L. R., Wong, T. M. & Meservey, R. Large Magnetoresistance at Room Temperature in Ferromagnetic Thin Film Tunnel Junctions. *Physical Review Letters* **74,** 3273–3276 (Apr. 17, 1995).
14. *Seagate reaches One Terabit per Square Inch Milestone in Hard Drive Storage with New Technology Demonstration | News Archive | Seagate* Seagate.com. https://www.seagate.com/in/en/news/news-archive/terabit-milestone-storage-seagate-master-pr/ (2022).
15. *2014: HDD areal density reaches 1 terabit/sq. in. | The Storage Engine | Computer History Museum* computerhistory.org. https://www.computerhistory.org/storageengine/hdd-areal-density-reaches-1-terabit-sq-in/ (2022).
16. Chappert, C., Fert, A. & Nguyen, F. V. The emergence of spin electronics in data storage. *NANOSCIENCE AND TECHNOLOGY* **6,** 11 (2009).
17. Dieny, B. *et al.* Opportunities and challenges for spintronics in the microelectronics industry. *Nature Electronics* **3,** 446–459 (Aug. 2020).

18. Brataas, A., Kent, A. D. & Ohno, H. Current-induced torques in magnetic materials. *Nature Materials* **11,** 372–381 (May 2012).
19. Allwood, D. A. Submicrometer Ferromagnetic NOT Gate and Shift Register. *Science* **296,** 2003–2006 (June 14, 2002).
20. Currivan, J. A., Youngman Jang, Mascaro, M. D., Baldo, M. A. & Ross, C. A. Low Energy Magnetic Domain Wall Logic in Short, Narrow, Ferromagnetic Wires. *IEEE Magnetics Letters* **3,** 3000104–3000104 (2012).
21. Currivan-Incorvia, J. A. *et al.* Logic circuit prototypes for three-terminal magnetic tunnel junctions with mobile domain walls. *Nature Communications* **7,** 10275 (Apr. 2016).
22. Manipatruni, S. *et al.* Scalable energy-efficient magnetoelectric spinorbit logic. *Nature* **565,** 35–42 (Jan. 2019).
23. Noël, P. *et al.* Non-volatile electric control of spincharge conversion in a SrTiO3 Rashba system. *Nature* **580,** 483–486 (Apr. 23, 2020).
24. *Samsung Electronics Starts Commercial Shipment of eMRAM Product Based on 28nm FD-SOI Process* `https://news.samsung.com/global/samsung-electronics-starts-commercial-shipment-of-emram-product-based-on-28nm-fd-soi-process` (2022).
25. Zhu, J.-G. & Park, C. Magnetic tunnel junctions. *Materials Today* **9,** 36–45 (Nov. 2006).
26. LaBonte, A. E. TwoDimensional BlochType Domain Walls in Ferromagnetic Films. *Journal of Applied Physics* **40,** 2450–2458 (May 1969).
27. Hubert, A. & Schäfer, R. *Magnetic domains: the analysis of magnetic microstructures* 696 pp. (Springer, Berlin ; New York, 1998).
28. Coey, J. M. D. Louis Néel: Retrospective (invited). *Journal of Applied Physics* **93,** 8224–8229 (May 15, 2003).
29. Ono, T. *et al.* Propagation of a Magnetic Domain Wall in a Submicrometer Magnetic Wire. *Science* **284,** 468–470 (Apr. 16, 1999).
30. Beach, G. S. D., Nistor, C., Knutson, C., Tsoi, M. & Erskine, J. L. Dynamics of field-driven domain-wall propagation in ferromagnetic nanowires. *Nature Materials* **4,** 741–744 (Oct. 2005).
31. Fukumoto, K. *et al.* Dynamics of Magnetic Domain Wall Motion after Nucleation: Dependence on the Wall Energy. *Physical Review Letters* **96,** 097204 (Mar. 9, 2006).
32. Tsoi, M., Fontana, R. E. & Parkin, S. S. P. Magnetic domain wall motion triggered by an electric current. *Applied Physics Letters* **83,** 2617–2619 (Sept. 29, 2003).
33. Yamaguchi, A. *et al.* Real-Space Observation of Current-Driven Domain Wall Motion in Submicron Magnetic Wires. *Physical Review Letters* **92,** 077205 (Feb. 19, 2004).
34. Kläui, M. *et al.* Controlled and Reproducible Domain Wall Displacement by Current Pulses Injected into Ferromagnetic Ring Structures. *Physical Review Letters* **94,** 106601 (Mar. 15, 2005).
35. Berger, L. Low-field magnetoresistance and domain drag in ferromagnets. *Journal of Applied Physics* **49,** 2156–2161 (Mar. 1978).
36. Parkin, S. S. P., Hayashi, M. & Thomas, L. Magnetic Domain-Wall Racetrack Memory. *Science,* 190–194 (Nov. 4, 2008).
37. Parkin, S. & Yang, S.-H. Memory on the racetrack. *Nature Nanotechnology* **10,** 195–198 (Mar. 2015).
38. Luo, Z. *et al.* Current-driven magnetic domain-wall logic. *Nature* **579,** 214–218 (Mar. 2020).
39. Slonczewski, J. Current-driven excitation of magnetic multilayers. *Journal of Magnetism and Magnetic Materials* **159,** L1–L7 (June 1996).
40. Thiaville, A., Nakatani, Y., Miltat, J. & Suzuki, Y. Micromagnetic understanding of current-driven domain wall motion in patterned nanowires. *Europhysics Letters (EPL)* **69,** 990–996 (Mar. 2005).

41. Manchon, A. *et al.* Current-induced spin-orbit torques in ferromagnetic and antiferromagnetic systems. *Reviews of Modern Physics* **91,** 035004 (Sept. 9, 2019).

42. Freitas, P. P. & Berger, L. Observation of s d exchange force between domain walls and electric current in very thin Permalloy films. *Journal of Applied Physics* **57,** 1266–1269 (Feb. 15, 1985).

43. Mougin, A., Cormier, M., Adam, J. P., Metaxas, P. J. & Ferré, J. Domain wall mobility, stability and Walker breakdown in magnetic nanowires. *Europhysics Letters (EPL)* **78,** 57007 (June 2007).

44. Kato, Y. K., Myers, R. C., Gossard, A. C. & Awschalom, D. D. Observation of the Spin Hall Effect in Semiconductors. *Science* **306,** 1910–1913 (Dec. 10, 2004).

45. Wunderlich, J., Kaestner, B., Sinova, J. & Jungwirth, T. Experimental Observation of the Spin-Hall Effect in a Two-Dimensional Spin-Orbit Coupled Semiconductor System. *Physical Review Letters* **94,** 047204 (Feb. 4, 2005).

46. Sinova, J., Valenzuela, S. O., Wunderlich, J., Back, C. H. & Jungwirth, T. Spin Hall effects. *Reviews of Modern Physics* **87,** 1213–1260 (Oct. 27, 2015).

47. Meier, L. *et al.* Measurement of Rashba and Dresselhaus spinorbit magnetic fields. *Nature Physics* **3,** 650–654 (Sept. 2007).

48. Manchon, A., Koo, H. C., Nitta, J., Frolov, S. M. & Duine, R. A. New perspectives for Rashba spinorbit coupling. *Nature Materials* **14,** 871–882 (Sept. 2015).

49. Khvalkovskiy, A. V. *et al.* High Domain Wall Velocities due to Spin Currents Perpendicular to the Plane. *Physical Review Letters* **102,** 067206 (Feb. 13, 2009).

50. Mihai Miron, I. *et al.* Current-driven spin torque induced by the Rashba effect in a ferromagnetic metal layer. *Nature Materials* **9,** 230–234 (Mar. 2010).

51. Haazen, P. P. J. *et al.* Domain wall depinning governed by the spin Hall effect. *Nature Materials* **12,** 299–303 (Apr. 2013).

52. Emori, S., Bauer, U., Ahn, S.-M., Martinez, E. & Beach, G. S. D. Current-driven dynamics of chiral ferromagnetic domain walls. *Nature Materials* **12,** 611–616 (July 2013).

53. Ryu, K.-S., Thomas, L., Yang, S.-H. & Parkin, S. Chiral spin torque at magnetic domain walls. *Nature Nanotechnology* **8,** 527–533 (July 2013).

54. Imai, M. *et al.* Observation of gyromagnetic reversal. *Applied Physics Letters* **113,** 052402 (July 30, 2018).

55. Stanciu, C. D. *et al.* Ultrafast spin dynamics across compensation points in ferrimagnetic GdFeCo : The role of angular momentum compensation. *Physical Review B* **73,** 220402 (June 12, 2006).

56. Binder, M. *et al.* Magnetization dynamics of the ferrimagnet CoGd near the compensation of magnetization and angular momentum. *Physical Review B* **74,** 134404 (Oct. 9, 2006).

57. Baltz, V. *et al.* Antiferromagnetic spintronics. *Reviews of Modern Physics* **90,** 015005 (Feb. 15, 2018).

58. Kim, K.-J. *et al.* Fast domain wall motion in the vicinity of the angular momentum compensation temperature of ferrimagnets. *Nature Materials* **16,** 1187–1192 (Dec. 2017).

59. Caretta, L. *et al.* Fast current-driven domain walls and small skyrmions in a compensated ferrimagnet. *Nature Nanotechnology* **13,** 1154–1160 (Dec. 2018).

60. Haltz, E., Krishnia, S., Berges, L., Mougin, A. & Sampaio, J. Domain wall dynamics in antiferromagnetically coupled double-lattice systems. *Physical Review B* **103,** 014444 (Jan. 27, 2021).

61. Han, J. *et al.* Room-Temperature Spin-Orbit Torque Switching Induced by a Topological Insulator. *Physical Review Letters* **119,** 077702 (Aug. 18, 2017).

62. Cai, K. *et al.* Ultrafast and energy-efficient spinorbit torque switching in compensated ferrimagnets. *Nature Electronics* **3,** 37–42 (Jan. 2020).

63. Siddiqui, S. A., Han, J., Finley, J. T., Ross, C. A. & Liu, L. Current-Induced Domain Wall Motion in a Compensated Ferrimagnet. *Physical Review Letters* **121,** 057701 (July 30, 2018).

64. Je, S.-G. *et al.* Spin-orbit torque-induced switching in ferrimagnetic alloys: Experiments and modeling. *Applied Physics Letters* **112,** 062401 (Feb. 5, 2018).

65. Avci, C. O. *et al.* Interface-driven chiral magnetism and current-driven domain walls in insulating magnetic garnets. *Nature Nanotechnology* **14,** 561–566 (June 2019).

66. Caretta, L. *et al.* Relativistic kinematics of a magnetic soliton. *Science* **370,** 1438–1442 (Dec. 18, 2020).

67. Palomino, A. *et al.* Evaluating critical metals contained in spintronic memory with a particular focus on Pt substitution for improved sustainability. *Sustainable Materials and Technologies* **28,** e00270 (July 2021).

68. *Concepts in spin electronics* (ed Maekawa, S.) *Series on semiconductor science and technology* **13** (Oxford University Press, Oxford ; New York, 2006). 398 pp.

69. Korenivski, V. & Slonczewski, J. *Introduction to Spintronics* (KTH-Physics, Stockholm, Mar. 13, 2007).

70. Coey, J. M. D. *Magnetism and Magnetic Materials* (Cambridge University Press, 2009).

71. Néel, L. Antiferromagnetism and Ferrimagnetism. *Proceedings of the Physical Society. Section A* **65,** 18 (1952).

72. Serga, A. A., Chumak, A. V. & Hillebrands, B. YIG magnonics. *Journal of Physics D: Applied Physics* **43,** 264002 (July 7, 2010).

73. Dionne, G. A review of ferrites for microwave applications. *Proceedings of the IEEE* **63,** 777–789 (1975).

74. Rodmacq, B., Auffret, S., Dieny, B., Monso, S. & Boyer, P. Crossovers from in-plane to perpendicular anisotropy in magnetic tunnel junctions as a function of the barrier degree of oxidation. *Journal of Applied Physics* **93,** 7513–7515 (May 15, 2003).

75. Ikeda, S. *et al.* A perpendicular-anisotropy CoFeBMgO magnetic tunnel junction. *Nature Materials* **9,** 721–724 (Sept. 2010).

76. Peng, S. *et al.* Origin of interfacial perpendicular magnetic anisotropy in MgO/CoFe/metallic capping layer structures. *Scientific Reports* **5,** 18173 (Dec. 2015).

77. Landau, L. & Lifshitz, E. in, 153–169 (Phys. Z. Sowjetunion 8, 1935).

78. Bloch, F. in *Zur Theorie des Austauschproblems und der Remanenzerscheinung der Ferromagnetika: Probleme des Atomkernbaues* (ed Bloch, F.) 295–335 (Springer Berlin Heidelberg, Berlin, Heidelberg, 1932).

79. Fong, X. *et al.* Spin-Transfer Torque Devices for Logic and Memory: Prospects and Perspectives. *IEEE Transactions on Computer-Aided Design of Integrated Circuits and Systems* **35,** 1–22 (Jan. 2016).

80. Néel, L. Energie des parois de Bloch dans les couches minces. *C. R. Acad. Sci. Paris* **241,** 533–536 (1958).

81. Ralph, D. & Stiles, M. Spin transfer torques. *Journal of Magnetism and Magnetic Materials* **320,** 1190–1216 (Apr. 2008).

82. Marrows, C. H. Spin-polarised currents and magnetic domain walls. *Advances in Physics* **54,** 585–713 (Dec. 2005).

83. Huang, S. X., Chen, T. Y. & Chien, C. L. Spin polarization of amorphous CoFeB determined by point-contact Andreev reflection. *Applied Physics Letters* **92,** 242509 (June 16, 2008).

84. Narahara, A., Ito, K. & Suemasu, T. Growth of ferromagnetic Fe4N epitaxial layers and a-axis-oriented Fe4N/MgO/Fe magnetic tunnel junction on MgO(001) substrates using molecular beam epitaxy. *Journal of Crystal Growth* **311,** 1616–1619 (Mar. 2009).

85. De Groot, R. A., Mueller, F. M., Engen, P. G. v. & Buschow, K. H. J. New Class of Materials: Half-Metallic Ferromagnets. *Physical Review Letters* **50,** 2024–2027 (June 20, 1983).

86. Gushi, T. *et al.* Large Current Driven Domain Wall Mobility and Gate Tuning of Coercivity in Ferrimagnetic Mn $_4$ N Thin Films. *Nano Letters* **19,** 8716–8723 (Dec. 11, 2019).

87. Gilbert, T. Classics in Magnetics A Phenomenological Theory of Damping in Ferromagnetic Materials. *IEEE Transactions on Magnetics* **40,** 3443–3449 (Nov. 2004).

88. Emori, S. *Magnetic Domain Walls Driven by Interfacial Phenomena* PhD thesis (Massachusetts Institute of Technology, 2014).

89. Zhang, S. & Li, Z. Roles of Nonequilibrium Conduction Electrons on the Magnetization Dynamics of Ferromagnets. *Physical Review Letters* **93,** 127204 (Sept. 17, 2004).

90. Tatara, G. & Kohno, H. Theory of Current-Driven Domain Wall Motion: Spin Transfer versus Momentum Transfer. *Physical Review Letters* **92,** 086601 (Feb. 26, 2004).

91. Wangsness, R. K. Sublattice Effects in Magnetic Resonance. *Physical Review* **91,** 1085–1091 (Sept. 1, 1953).

92. Yang, S.-H., Ryu, K.-S. & Parkin, S. Domain-wall velocities of up to 750 m s1 driven by exchange-coupling torque in synthetic antiferromagnets. *Nature Nanotechnology* **10,** 221–226 (Mar. 2015).

93. Okuno, T. *et al.* Spin-transfer torques for domain wall motion in antiferromagnetically coupled ferrimagnets. *Nature Electronics* **2,** 389–393 (Sept. 2019).

94. Haltz, E. *Domain wall dynamics driven by spin-current in ferrimagnetic alloys* PhD thesis (2019).

95. Kobayashi, T., Hayashi, H., Fujiwara, Y. & Shiomi, S. Damping parameter and wall velocity of RE-TM films. *IEEE Transactions on Magnetics* **41,** 2848–2850 (Oct. 2005).

96. Atkins, P. *et al. Shriver and Atkins' Inorganic chemistry* 5th ed. (Oxford University Press, W. H. Freeman and Company, 41 Madison Avenue, New York, NY 10010, 2010).

97. Doll, G. L. *et al.* Intercalation of hexagonal boron nitride with potassium. *Journal of Applied Physics* **66,** 2554–2558 (Sept. 15, 1989).

98. Stone, D. S., Yoder, K. B. & Sproul, W. D. Hardness and elastic modulus of TiN based on continuous indentation technique and new correlation. *Journal of Vacuum Science & Technology A: Vacuum, Surfaces, and Films* **9,** 2543–2547 (July 1991).

99. Oyama, S. T. *The chemistry of Transition Metal Nitrides and Carbides* (Springer International Publishing, 1996).

100. Pierson, H. O. *Handbook of Refractory Carbides and Nitrides* (William Andrew Inc., 1996).

101. Carlson, O. N. The N-Si (Nitrogen-Silicon) system. *Bulletin of Alloy Phase Diagrams* **11,** 569–573 (Dec. 1990).

102. Riley, F. L. Silicon Nitride and Related Materials. *Journal of the American Ceramic Society* **83,** 245–265 (Dec. 21, 2004).

103. *The Nobel Prize in Physics 2014* NobelPrize.org. `https://www.nobelprize.org/prizes/physics/2014/press-release/` (2022).

104. Jain, A. *et al.* Commentary: The Materials Project: A materials genome approach to accelerating materials innovation. *APL Materials* **1,** 011002 (July 2013).

105. Bykov, M. *et al.* Fe-N system at high pressure reveals a compound featuring polymeric nitrogen chains. *Nature Communications* **9,** 2756 (Dec. 2018).

106. Mekata, M. Magnetic Study on Mn4N and its Related Compounds. *Journal of the Physical Society of Japan* **17,** 796–803 (1962).

107. Fruchart, D. & Bertaut, E. F. Magnetic Studies of the Metallic Perovskite-Type Compounds of Manganese. *Journal of the Physical Society of Japan* **44** (Mar. 1978).

108. Fruchart, D., Givord, D., Convert, P., l'Heritier, P. & Senateur, J. P. The non-collinear component in the magnetic structure of Mn $_4$ N. *Journal of Physics F: Metal Physics* **9,** 2431–2437 (Dec. 1979).

109. Matsunami, D., Fujita, A., Takenaka, K. & Kano, M. Giant barocaloric effect enhanced by the frustration of the antiferromagnetic phase in Mn3GaN. *Nature Materials* **14,** 73–78 (Jan. 2015).

110. Zemen, J. *et al.* Frustrated magnetism and caloric effects in Mn-based antiperovskite nitrides: *Ab initio* theory. *Physical Review B* **95,** 184438 (May 31, 2017).

111. Takenaka, K. & Takagi, H. Giant negative thermal expansion in Ge-doped anti-perovskite manganese nitrides. *Applied Physics Letters* **87,** 261902 (Dec. 26, 2005).

112. Ito, K., Lee, G. H. & Suemasu, T. Epitaxial growth of ferromagnetic Fe $_4$ N thin films on SrTiO $_3$ (001) substrates by molecular beam epitaxy. *Journal of Physics: Conference Series* **266,** 012091 (Jan. 1, 2011).

113. Ito, K. *et al.* Local electronic states of Fe $_4$ N films revealed by x-ray absorption spectroscopy and x-ray magnetic circular dichroism. *Journal of Applied Physics* **117,** 193906 (May 21, 2015).

114. Takata, F. *et al.* Preferred site occupation of 3 d atoms in Ni x F e 4 x N (x = 1 and 3) films revealed by x-ray absorption spectroscopy and magnetic circular dichroism. *Physical Review Materials* **2,** 024407 (Feb. 23, 2018).

115. Ito, K., Harada, K., Toko, K., Akinaga, H. & Suemasu, T. Epitaxial growth and magnetic characterization of ferromagnetic Co4N thin films on SrTiO3(001) substrates by molecular beam epitaxy. *Journal of Crystal Growth* **336,** 40–43 (Dec. 2011).

116. Ito, K. *et al.* X-ray magnetic circular dichroism of ferromagnetic Co $_4$ N epitaxial films on SrTiO $_3$ (001) substrates grown by molecular beam epitaxy. *Applied Physics Letters* **99,** 252501 (Dec. 19, 2011).

117. Yasutomi, Y., Ito, K., Sanai, T., Toko, K. & Suemasu, T. Perpendicular magnetic anisotropy of Mn $_4$ N films on MgO(001) and SrTiO $_3$ (001) substrates. *Journal of Applied Physics* **115,** 17A935 (May 7, 2014).

118. Gushi, T. *et al.* Millimeter-sized magnetic domains in perpendicularly magnetized ferrimagnetic Mn $_4$ N thin films grown on SrTiO $_3$. *Japanese Journal of Applied Physics* **57,** 120310 (Dec. 1, 2018).

119. Komori, T., Anzai, A., Gushi, T., Toko, K. & Suemasu, T. Molecular beam epitaxy growth of Mn4Ni N thin films on MgO(0 0 1) substrates and their magnetic properties. *Journal of Crystal Growth* **507,** 163–167 (Feb. 2019).

120. Hirose, T. *et al.* Strong correlation between uniaxial magnetic anisotropic constant and in-plane tensile strain in Mn $_4$ N epitaxial films. *AIP Advances* **10,** 025117 (Feb. 1, 2020).

121. Sanai, T., Ito, K., Toko, K. & Suemasu, T. Epitaxial growth of ferromagnetic CoxFe4xN thin films on SrTiO3 (001) and magneticproperties. *Journal of Crystal Growth* **378,** 342–346 (Sept. 2013).

122. Ito, K. *et al.* Perpendicular magnetic anisotropy in Co $_x$ Mn $_{4\,x}$ N (x = 0 and 0.2) epitaxial films and possibility of tetragonal Mn $_4$ N phase. *AIP Advances* **6,** 056201 (May 2016).

123. Anzai, A., Takata, F., Gushi, T., Toko, K. & Suemasu, T. Epitaxial growth and magnetic properties of Fe 4 x Mn x N thin films grown on MgO(0 0 1) substrates by molecular beam epitaxy. *Journal of Crystal Growth* **489,** 20–23 (May 2018).

124. Anzai, A. *et al.* Transition from minority to majority spin transport in iron-manganese nitride Fe $_{4\,x}$ Mn $_x$ N films with increasing x. *Journal of Applied Physics* **124,** 123905 (Sept. 28, 2018).

125. Takata, F. *et al.* Epitaxial growth and magnetic properties of Ni $_x$ Fe $_{4-x}$ N ($x = 0$, 1, 3, and 4) films on SrTiO $_3$ (001) substrates. *Journal of Applied Physics* **120,** 083907 (Aug. 28, 2016).

126. Matar, S., Mohn, P., Demazeau, G. & Siberchicot, B. The calculated electronic and magnetic structures of Fe4N and Mn 4N. *Journal de Physique* **49,** 1761–1768 (1988).

127. Tagawa, Y. & Motizuki, K. Electronic band structures and magnetism of intermetallic manganese compounds Mn $_4$ X (X identical to N, C). *Journal of Physics: Condensed Matter* **3,** 1753–1761 (Mar. 25, 1991).

128. Kokado, S., Fujima, N., Harigaya, K., Shimizu, H. & Sakuma, A. Theoretical analysis of highly spin-polarized transport in the iron nitride Fe 4 N. *Physical Review B* **73,** 172410 (May 17, 2006).

129. Ghosh, S. *et al.* Current-Driven Domain Wall Dynamics in Ferrimagnetic Nickel-Doped Mn $_4$ N Films: Very Large Domain Wall Velocities and Reversal of Motion Direction across the Magnetic Compensation Point. *Nano Letters* **21,** 2580–2587 (Mar. 24, 2021).

130. Jiang, E.-y., Sun, C.-q., Li, J.-e. & Liu, Y.-g. The structures and magnetic properties of FeN films prepared by the facing targets sputtering method. *Journal of Applied Physics* **65,** 1659–1663 (Feb. 15, 1989).

131. Wang, X., Zheng, W., Tian, H., Yu, S. & Wang, L. Effect of substrate temperature and bias voltage on DC magnetron sputtered FeN thin films. *Journal of Magnetism and Magnetic Materials* **283,** 282–290 (Dec. 2004).

132. Suzuki, K. *et al.* Crystal structure and magnetic properties of the compound MnN. *Journal of Alloys and Compounds* **306,** 66–71 (June 2000).

133. Coey, J. & Smith, P. Magnetic nitrides. *Journal of Magnetism and Magnetic Materials* **200,** 405–424 (Oct. 1999).

134. Monachesi, P., Björkman, T., Gasche, T. & Eriksson, O. Electronic structure and magnetic properties of Mn, Co, and Ni substitution of Fe in Fe 4 N. *Physical Review B* **88,** 054420 (Aug. 26, 2013).

135. Yasuda, T. *et al.* Ferrimagneticferromagnetic phase transition in Mn $_4$ N films favored by non-magnetic In doping. *Journal of Physics D: Applied Physics* **55,** 115003 (Mar. 17, 2022).

136. Komori, T. *et al.* Magnetic reversal in rare-earth free Mn $_{4-x}$ Ni $_x$ N epitaxial films below and above Ni composition needed for magnetic compensation around room temperature. *Journal of Applied Physics* **127,** 043903 (Jan. 31, 2020).

137. Ito, K. *et al.* Manipulation of saturation magnetization and perpendicular magnetic anisotropy in epitaxial C o x M n 4 x N films with ferrimagnetic compensation. *Physical Review B* **101,** 104401 (Mar. 2, 2020).

138. Mitarai, H. *et al.* Magnetic compensation at two different composition ratios in rare-earth-free Mn 4 x Co x N ferrimagnetic films. *Physical Review Materials* **4,** 094401 (Sept. 8, 2020).

139. Fruchart, D., Bertaut, E. F., Madar, R., Lorthioir, G. & Fruchart, R. Structure magnetique et rotation de spin de Mn3NiN. *Solid State Communications* **9,** 1793–1797 (1971).

140. Boldrin, D. *et al.* Multisite Exchange-Enhanced Barocaloric Response in Mn 3 NiN. *Physical Review X* **8,** 041035 (Nov. 28, 2018).

141. Boldrin, D. *et al.* The Biaxial Strain Dependence of Magnetic Order in Spin Frustrated Mn $_3$ NiN Thin Films. *Advanced Functional Materials* **29,** 1902502 (Oct. 2019).

142. Gurung, G., Ding-Fu, S., Tula R, P. & Evgeny Y, T. Anomalous Hall conductivity of noncollinear magnetic antiperovskites. *Phys. Rev. Materials* **3,** 044409 (Apr. 23, 2019).

143. Liu, Z. Q. *et al.* Electrical switching of the topological anomalous Hall effect in a non-collinear antiferromagnet above room temperature. *Nature Electronics* **1,** 172–177 (Mar. 2018).

144. Boldrin, D. *et al.* Giant Piezomagnetism in Mn $_3$ NiN. *ACS Applied Materials & Interfaces* **10,** 18863–18868 (June 6, 2018).

145. Terao, P. N. Une Nouvelle Formede Nickel: Ni4N. *Journal of the Physical Society of Japan* **15** (Feb. 1960).

146. Fang, C.-M., Koster, R. S., Li, W.-F. & van Huis, M. A. Predicted stability, structures, and magnetism of 3d transition metal nitrides: the M4N phases. *RSC Advances* **4,** 7885 (2014).

147. Linnik, A. I. *et al.* Magnetic properties and thermal modification of nanostructured films of nickel nitrides. *Technical Physics Letters* **39,** 143–146 (Feb. 2013).

148. Pandey, N., Gupta, M. & Stahn, J. Structure, Thermal Stability, and Magnetism of Ni $_4$ N Thin Films. *physica status solidi (RRL) Rapid Research Letters* **14,** 2000294 (Oct. 2020).

149. Asano, K., Koyama, K. & Takenaka, K. Magnetostriction in Mn3CuN. *Applied Physics Letters* **92,** 161909 (Apr. 21, 2008).

150. Shimizu, T., Shibayama, T., Asano, K. & Takenaka, K. Giant magnetostriction in tetragonally distorted antiperovskite manganese nitrides. *Journal of Applied Physics* **111,** 07A903 (Apr. 2012).

151. Matsumoto, T. *et al.* Hall effect measurements of high-quality M n 3 CuN thin films and the electronic structure. *Physical Review B* **96,** 205153 (Nov. 29, 2017).

152. Takei, W. J., Shirane, G. & Frazer, B. C. Magnetic Structure of Mn 4 N. *Physical Review* **119,** 122–126 (July 1, 1960).

153. Wiener, G. W. & Berger, J. A. Structure and Magnetic Properties of Some Transition Metal Nitrides. *JOM* **7,** 360–368 (Feb. 1955).

154. Juza, R. V., Puff, H. & Wagenknecht, F. Zur Kenntnis des Systems Mangan/Stickstoff. *Z. Electrochem* **61,** 804 (June 24, 1957).

155. Takei, W. J., Heikes, R. R. & Shirane, G. Magnetic Structure of Mn 4 N-Type Compounds. *Physical Review* **125,** 1893–1897 (Mar. 15, 1962).

156. Dhar, S., Brandt, O. & Ploog, K. H. Ferrimagnetic Mn4N(111) layers grown on 6H-SiC(0001) and GaN(0001) by reactive molecular-beam epitaxy. *Applied Physics Letters* **86,** 112504 (Mar. 14, 2005).

157. Li, C. *et al.* Fabrication and magnetic characteristic of ferrimagnetic bulk Mn4N. *Journal of Alloys and Compounds* **457,** 57–60 (June 2008).

158. Isogami, S., Rajamanickam, N., Kozuka, Y. & Takahashi, Y. K. Efficient current-driven magnetization switching owing to isotropic magnetism in a highly symmetric 111-oriented Mn $_4$ N epitaxial single layer. *AIP Advances* **11,** 105314 (Oct. 1, 2021).

159. Nakagawa, S. & Naoe, M. Preparation and magnetic properties of Mn $_4$ N films by reactive facing targets sputtering. *Journal of Applied Physics* **75,** 6568–6570 (May 15, 1994).

160. Ching, K. M., Chang, W. D., Chin, T. S., Duh, J. G. & Ku, H. C. Anomalous perpendicular magnetoanisotropy in Mn $_4$ N films on Si(100). *Journal of Applied Physics* **76,** 6582–6584 (Nov. 15, 1994).

161. Kabara, K. & Tsunoda, M. Perpendicular magnetic anisotropy of Mn $_4$ N films fabricated by reactive sputtering method. *Journal of Applied Physics* **117,** 17B512 (May 7, 2015).

162. Suemasu, T., Vila, L. & Attané, J.-P. Present Status of Rare-earth Free Ferrimagnet Mn $_4$ N and Future Prospects of Mn $_4$ N-based Compensated Ferrimagnets. *Journal of the Physical Society of Japan* **90,** 081010 (Aug. 15, 2021).

163. Isogami, S., Masuda, K. & Miura, Y. Contributions of magnetic structure and nitrogen to perpendicular magnetocrystalline anisotropy in antiperovskite M n 4 N. *Physical Review Materials* **4,** 014406 (Jan. 13, 2020).

164. Li, W. *et al.* Growth of Mn4N film with enhanced perpendicular magnetization on glass substrate using MnO seed layer. *Materials Letters* **311,** 131615 (Mar. 2022).

165. Ma, C. T., Hartnett, T. Q., Zhou, W., Balachandran, P. V. & Poon, S. J. Tunable magnetic skyrmions in ferrimagnetic Mn $_4$ N. *Applied Physics Letters* **119,** 192406 (Nov. 8, 2021).

166. Shen, X. *et al.* Metallic transport and large anomalous Hall effect at room temperature in ferrimagnetic Mn $_4$ N epitaxial thin film. *Applied Physics Letters* **105,** 072410 (Aug. 18, 2014).

167. Meng, M. *et al.* Extrinsic anomalous Hall effect in epitaxial Mn $_4$ N films. *Applied Physics Letters* **106,** 032407 (Jan. 19, 2015).

168. Ching, K.-M., Chang, W.-D. & Chin, T.-S. Magnetic properties and structure of Mn4N films on glass substrates. *Journal of Alloys and Compounds* **222,** 184–187 (May 1995).

169. Zhang, Z. *et al.* Magnetic properties of MBE grown Mn $_4$ N on MgO, SiC, GaN and Al $_2$ O $_3$ substrates. *AIP Advances* **10,** 015238 (Jan. 1, 2020).

170. Isogami, S., Masuda, K., Miura, Y., Rajamanickam, N. & Sakuraba, Y. Anomalous Hall and Nernst effects in ferrimagnetic Mn $_4$ N films: Possible interpretations and prospects for enhancement. *Applied Physics Letters* **118,** 092407 (Mar. 1, 2021).

171. Hirose, T., Komori, T., Gushi, T., Toko, K. & Suemasu, T. Perpendicular magnetic anisotropy in ferrimagnetic Mn4N films grown on (LaAlO3)0.3(Sr2TaAlO6)0.7(0 0 1) substrates by molecular beam epitaxy. *Journal of Crystal Growth* **535,** 125566 (Apr. 2020).

172. Kabara, K., Tsunoda, M. & Kokado, S. Magneto-transport properties of pseudo-single-crystal Mn $_4$ N thin films. *AIP Advances* **7,** 056416 (May 2017).

173. Zhang, Z., Shi, X., Liu, X., Chen, X. & Mi, W. Microstructure, magnetic and electronic transport properties of reactively facing-target sputtered epitaxial Mn $_4$ N films. *Journal of Physics: Condensed Matter* **34,** 065802 (Feb. 9, 2022).

174. Ikhlas, M., Tomita, T. & Nakatsuji, S. *Sample Quality Dependence of the Magnetic Properties in Non-Collinear Antiferromagnet Mn $_3$ Sn* in *Proceedings of the International Conference on Strongly Correlated Electron Systems (SCES2019)* Proceedings of the International Conference on Strongly Correlated Electron Systems (SCES2019) (Journal of the Physical Society of Japan, Okayama, Japan, Mar. 19, 2020).

175. Yang, H., Al-Brithen, H., Trifan, E., Ingram, D. C. & Smith, A. R. Crystalline phase and orientation control of manganese nitride grown on MgO(001) by molecular beam epitaxy. *Journal of Applied Physics* **91,** 1053–1059 (Feb. 2002).

176. Mihai, A. P., Attané, J. P., Marty, A., Warin, P. & Samson, Y. Electron-magnon diffusion and magnetization reversal detection in FePt thin films. *Physical Review B* **77,** 060401 (Feb. 7, 2008).

177. Nguyen, V. D. *et al.* Detection of Domain-Wall Position and Magnetization Reversal in Nanostructures Using the Magnon Contribution to the Resistivity. *Physical Review Letters* **107,** 136605 (Sept. 21, 2011).

178. Ito, K. *et al.* Magnetic domain walls in nanostrips of single-crystalline Fe $_4$ N(001) thin films with fourfold in-plane magnetic anisotropy. *Journal of Applied Physics* **121,** 243904 (June 28, 2017).

179. Gehanno, V., Samson, Y., Marty, A., Gilles, B. & Chamberod, A. Magnetic susceptibility and magnetic domain configuration as a function of the layer thickness in epitaxial FePd(0 0 1) thin films ordered in the L10 structure. *Journal of Magnetism and Magnetic Materials,* 26–40 (1997).

180. Attané, J. P. *et al.* Magnetic Domain Wall Propagation unto the Percolation Threshold across a Pseudorectangular Disordered Lattice. *Physical Review Letters* **93,** 257203 (Dec. 13, 2004).

181. Yamanouchi, M. *et al.* Domain Structure in CoFeB Thin Films With Perpendicular Magnetic Anisotropy. *IEEE Magnetics Letters* **2,** 3000304–3000304 (Dec. 2011).

182. Kaplan, B. & Gehring, G. The domain structure in ultrathin magnetic films. *Journal of Magnetism and Magnetic Materials* **128,** 111–116 (Nov. 1993).

183. Ando, F. *et al.* Modulation of the magnetic domain size induced by an electric field. *Applied Physics Letters* **109,** 022401 (July 11, 2016).

184. Gushi, T. *Mn4N thin films for spintronics applications based on current-induced domain wall motion* PhD thesis (2019).

185. Schneider, C. A., Rasband, W. S. & Eliceiri, K. W. NIH Image to ImageJ: 25 years of image analysis. *Nature Methods* **9,** 671–675 (July 2012).

186. Vernier, N., Allwood, D. A., Atkinson, D., Cooke, M. D. & Cowburn, R. P. Domain wall propagation in magnetic nanowires by spin-polarized current injection. *Europhysics Letters (EPL)* **65,** 526–532 (Feb. 2004).

187. Yamaguchi, A. *et al.* Effect of Joule heating in current-driven domain wall motion. *Applied Physics Letters* **86,** 012511 (Jan. 3, 2005).

188. Yamaguchi, A., Yano, K., Tanigawa, H., Kasai, S. & Ono, T. Reduction of Threshold Current Density for Current-Driven Domain Wall Motion using Shape Control. *Japanese Journal of Applied Physics* **45,** 3850–3853 (May 9, 2006).

189. Chiba, D. *et al.* Control of Multiple Magnetic Domain Walls by Current in a Co/Ni Nano-Wire. *Applied Physics Express* **3,** 073004 (July 2, 2010).

190. Miron, I. M. *et al.* Fast current-induced domain-wall motion controlled by the Rashba effect. *Nature Materials* **10,** 419–423 (June 2011).

191. Metaxas, P. J. *et al.* Creep and Flow Regimes of Magnetic Domain-Wall Motion in Ultrathin Pt / Co / Pt Films with Perpendicular Anisotropy. *Physical Review Letters* **99,** 217208 (Nov. 21, 2007).

192. Fert, A. & Levy, P. M. Role of Anisotropic Exchange Interactions in Determining the Properties of Spin-Glasses. *Physical Review Letters* **44,** 1538–1541 (June 9, 1980).

193. Fert, A., Cros, V. & Sampaio, J. Skyrmions on the track. *Nature Nanotechnology* **8,** 152–156 (Mar. 2013).

194. Fukami, S., Suzuki, T., Ohshima, N., Nagahara, K. & Ishiwata, N. Micromagnetic analysis of current driven domain wall motion in nanostrips with perpendicular magnetic anisotropy. *Journal of Applied Physics* **103,** 07E718 (Apr. 2008).

195. Szambolics, H., Toussaint, J.-C., Marty, A., Miron, I. & Buda-Prejbeanu, L. Domain wall motion in ferromagnetic systems with perpendicular magnetization. *Journal of Magnetism and Magnetic Materials* **321,** 1912–1918 (July 2009).

196. Ngo, D.-T., Ikeda, K. & Awano, H. Direct Observation of Domain Wall Motion Induced by Low-Current Density in TbFeCo Wires. *Applied Physics Express* **4,** 093002 (Aug. 9, 2011).

197. Ngo, D.-T., Ikeda, K. & Awano, H. Modulation of domain wall dynamics in TbFeCo single layer nanowire. *Journal of Applied Physics* **111,** 083921 (Apr. 15, 2012).

198. Freeman, M. R. & Smyth, J. F. Picosecond time-resolved magnetization dynamics of thin-film heads. *Journal of Applied Physics* **79,** 5898 (1996).

199. Miao, M. S., Herwadkar, A. & Lambrecht, W. R. L. Electronic structure and magnetic properties of Mn 3 Ga N precipitates in Ga 1 x Mn x N. *Physical Review B* **72,** 033204 (July 15, 2005).

200. Vansteenkiste, A. *et al.* The design and verification of MuMax3. *AIP Advances* **4,** 107133 (Oct. 2014).

201. Boulle, O., Malinowski, G. & Kläui, M. Current-induced domain wall motion in nanoscale ferromagnetic elements. *Materials Science and Engineering: R: Reports* **72,** 159–187 (Sept. 2011).

202. Adam, J.-P. *et al.* Nonadiabatic spin-transfer torque in (Ga,Mn)As with perpendicular anisotropy. *Physical Review B* **80,** 193204 (Nov. 17, 2009).

203. Curiale, J., Lemaître, A., Ulysse, C., Faini, G. & Jeudy, V. Spin Drift Velocity, Polarization, and Current-Driven Domain-Wall Motion in (Ga,Mn)(As,P). *Physical Review Letters* **108,** 076604 (Feb. 17, 2012).

204. Je, S.-G. *et al.* Asymmetric magnetic domain-wall motion by the Dzyaloshinskii-Moriya interaction. *Physical Review B* **88,** 214401 (Dec. 2, 2013).

205. Hrabec, A. *et al.* Measuring and tailoring the Dzyaloshinskii-Moriya interaction in perpendicularly magnetized thin films. *Physical Review B* **90,** 020402 (July 16, 2014).

206. Pizzini, S. *et al.* Chirality-Induced Asymmetric Magnetic Nucleation in Pt / Co / AlO x Ultrathin Microstructures. *Physical Review Letters* **113,** 047203 (July 23, 2014).

207. Juza, R. V., Deneke, K. & Puff, H. Ferrimagnetismus der Mischkristalle von Mn4N mit Chrom, Eisen und Nickel. *Z. Electrochem* **65,** 551 (Feb. 19, 1959).

208. Hirata, Y. *et al.* Correlation between compensation temperatures of magnetization and angular momentum in GdFeCo ferrimagnets. *Physical Review B* **97,** 220403 (June 12, 2018).

209. Margulies, D. T. *et al.* Origin of the Anomalous Magnetic Behavior in Single Crystal Fe 3 O 4 Films. *Physical Review Letters* **79,** 5162–5165 (Dec. 22, 1997).

210. Hibma, T. *et al.* Anti-phase domains and magnetism in epitaxial magnetite layers. *Journal of Applied Physics* **85,** 5291–5293 (Apr. 15, 1999).

211. Crandles, D. A., DesRoches, B. & Razavi, F. S. A search for defect related ferromagnetism in SrTiO3. *Journal of Applied Physics* **108,** 053908 (Sept. 2010).

212. Amemiya, K. *et al.* Fast polarization switching in the soft X-ray region at PF BL-16A. *Journal of Physics: Conference Series* **425,** 152015 (Mar. 22, 2013).

213. Stöhr, J. & König, H. Determination of Spin- and Orbital-Moment Anisotropies in Transition Metals by Angle-Dependent X-Ray Magnetic Circular Dichroism. *Physical Review Letters* **75,** 3748–3751 (Nov. 13, 1995).

214. Li, F., Yang, J., Xue, D. & Zhou, R. Mössbauer study of the (Fe $_{1\,x}$ Ni $_{x}$) $_{4}$ N compounds (0 x 0.6). *Applied Physics Letters* **66,** 2343–2345 (May 1995).

215. Kang, J.-S. *et al.* Soft x-ray absorption spectroscopy and magnetic circular dichroism study of the valence and spin states in spinel Mn Fe 2 O 4. *Physical Review B* **77,** 035121 (Jan. 17, 2008).

216. Ma, X. *et al.* Structural stability and magnetism of -Fe4N and CoFe3N compounds. *Journal of Alloys and Compounds* **480,** 475–480 (July 2009).

217. Awano, H. Investigation of domain wall motion in RE-TM magnetic wire towards a current driven memory and logic. *Journal of Magnetism and Magnetic Materials* **383,** 50–55 (June 2015).

218. Kresse, G. & Hafner, J. *Ab initio* molecular dynamics for liquid metals. *Physical Review B* **47,** 558–561 (Jan. 1, 1993).

219. Kresse, G. & Furthmüller, J. Efficiency of ab-initio total energy calculations for metals and semiconductors using a plane-wave basis set. *Computational Materials Science* **6,** 15–50 (July 1996).

220. Kresse, G. & Furthmüller, J. Efficient iterative schemes for *ab initio* total-energy calculations using a plane-wave basis set. *Physical Review B* **54,** 11169–11186 (Oct. 15, 1996).

221. Blöchl, P. E. Projector augmented-wave method. *Physical Review B* **50,** 17953–17979 (Dec. 15, 1994).

222. Perdew, J. P., Burke, K. & Ernzerhof, M. Generalized Gradient Approximation Made Simple. *Physical Review Letters* **77,** 3865–3868 (Oct. 28, 1996).

223. Kresse, G. & Joubert, D. From ultrasoft pseudopotentials to the projector augmented-wave method. *Physical Review B* **59,** 1758–1775 (Jan. 15, 1999).

224. Ebert, H., Ködderitzsch, D. & Minár, J. Calculating condensed matter properties using the KKR-Green's function methodrecent developments and applications. *Reports on Progress in Physics* **74,** 096501 (Sept. 1, 2011).

225. Ebert, H., Braun, J., Ködderitzsch, D. & Mankovsky, S. Fully relativistic multiple scattering calculations for general potentials. *Physical Review B* **93,** 075145 (Feb. 23, 2016).

226. Ebert, H. *The Munich SPR-KKR package*

227. Meinert, M. Exchange interactions and Curie temperatures of the tetrametal nitrides Cr $_4$ N, Mn $_4$ N, Fe $_4$ N, Co $_4$ N, and Ni $_4$ N. *Journal of Physics: Condensed Matter* **28,** 056006 (Feb. 10, 2016).

228. Mazurenko, V. V., Kvashnin, Y. O., Lichtenstein, A. I. & Katsnelson, M. I. A DMI Guide to Magnets Micro-World. *Journal of Experimental and Theoretical Physics* **132,** 506–516 (Apr. 2021).

229. Yu, X. Z. *et al.* Transformation between meron and skyrmion topological spin textures in a chiral magnet. *Nature* **564,** 95–98 (Dec. 2018).

230. Miron, I. M. *et al.* Perpendicular switching of a single ferromagnetic layer induced by in-plane current injection. *Nature* **476,** 189–193 (Aug. 2011).

231. Liu, L. *et al.* Spin-Torque Switching with the Giant Spin Hall Effect of Tantalum. *Science* **336,** 555–558 (May 4, 2012).

232. Garello, K. *et al. SOT-MRAM 300MM Integration for Low Power and Ultrafast Embedded Memories* in *2018 IEEE Symposium on VLSI Circuits* 2018 IEEE Symposium on VLSI Circuits (IEEE, Honolulu, HI, June 2018), 81–82.

233. Garello, K. *et al.* Symmetry and magnitude of spinorbit torques in ferromagnetic heterostructures. *Nature Nanotechnology* **8,** 587–593 (Aug. 2013).

234. Zheng, Z. *et al.* Field-free spin-orbit torque-induced switching of perpendicular magnetization in a ferrimagnetic layer with a vertical composition gradient. *Nature Communications* **12,** 4555 (Dec. 2021).

235. Nishikawa, S. & Kikuchi, S. Diffraction of cathode rays by mica. *Nature* **121,** 1019–1020 (June 30, 1928).

236. Williams, D. B. & Carter, C. B. *Transmission electron microscopy: a textbook for materials science* 2nd ed. 4 pp. (Springer, New York, 2008).

237. Nguyen, M.-H., Ralph, D. C. & Buhrman, R. A. Spin Torque Study of the Spin Hall Conductivity and Spin Diffusion Length in Platinum Thin Films with Varying Resistivity. *Physical Review Letters* **116,** 126601 (Mar. 24, 2016).

238. Dutta, S. *et al.* Thickness dependence of the resistivity of platinum-group metal thin films. *Journal of Applied Physics* **122,** 025107 (July 14, 2017).

239. Nguyen, V. D. *et al.* Asymmetric magnetoresistance of nanowires with perpendicular anisotropy seen as a contribution from the contacts. *Journal of Applied Physics* **113,** 183906 (May 14, 2013).

240. McGuire, T. & Potter, R. Anisotropic magnetoresistance in ferromagnetic 3d alloys. *IEEE Transactions on Magnetics* **11,** 1018–1038 (Apr. 7, 1975).

241. Viret, M. *et al.* Spin scattering in ferromagnetic thin films. *Physical Review B* **53,** 8464–8468 (Apr. 1, 1996).

242. Marrows, C. H. & Dalton, B. C. Spin Mixing and Spin-Current Asymmetry Measured by Domain Wall Magnetoresistance. *Physical Review Letters* **92,** 097206 (Mar. 4, 2004).

243. Pai, C.-F. *et al.* Spin transfer torque devices utilizing the giant spin Hall effect of tungsten. *Applied Physics Letters* **101,** 122404 (Sept. 17, 2012).

244. Vudya Sethu, K. K. *et al.* Optimization of Tungsten -Phase Window for Spin-Orbit-Torque Magnetic Random-Access Memory. *Physical Review Applied* **16,** 064009 (Dec. 3, 2021).

245. Onur Avci, C. *et al.* Magnetization switching of an MgO/Co/Pt layer by in-plane current injection. *Applied Physics Letters* **100,** 212404 (May 21, 2012).

246. Yang, Y. *et al.* Ultrafast magnetization reversal by picosecond electrical pulses. *Science Advances* **3,** e1603117 (Nov. 3, 2017).

247. Roschewsky, N. *et al.* Spin-orbit torques in ferrimagnetic GdFeCo alloys. *Applied Physics Letters* **109,** 112403 (Sept. 12, 2016).

248. Bai, H., Xu, T., Dong, Y., Zhou, H.-A. & Jiang, W. SpinTorque Switching in RareEarthFree Compensated Ferrimagnet Mn4N Films. *Advanced Electronic Materials* (Nov. 12, 2021).

249. Yu, J. *et al.* Long spin coherence length and bulk-like spinorbit torque in ferrimagnetic multilayers. *Nature Materials* **18,** 29–34 (Jan. 2019).

250. Nikonov, D. E., Bourianoff, G. I. & Ghani, T. Proposal of a Spin Torque Majority Gate Logic. *IEEE Electron Device Letters* **32,** 1128–1130 (Aug. 2011).

251. Murapaka, C., Sethi, P., Goolaup, S. & Lew, W. S. Reconfigurable logic via gate controlled domain wall trajectory in magnetic network structure. *Scientific Reports* **6,** 20130 (Apr. 2016).

252. Raymenants, E. *et al. Scaled spintronic logic device based on domain wall motion in magnetically interconnected tunnel junctions* in *2018 IEEE International Electron Devices Meeting (IEDM)* 2018 IEEE International Electron Devices Meeting (IEDM) (IEEE, San Francisco, CA, Dec. 2018), 36.4.1–36.4.4.

253. Raymenants, E. *et al.* Nanoscale domain wall devices with magnetic tunnel junction read and write. *Nature Electronics* **4,** 392–398 (June 2021).

254. Luo, Z. *et al.* Field- and Current-Driven Magnetic Domain-Wall Inverter and Diode. *Physical Review Applied* **15,** 034077 (Mar. 26, 2021).

255. Raymenants, E. *et al.* Magnetic domain walls: from physics to devices. *2021 IEEE International Electron Devices Meeting (IEDM),* 32.3.1–32.3.4 (2021).

256. Vaysset, A. *et al.* Toward error-free scaled spin torque majority gates. *AIP Advances* **6,** 065304 (June 2016).

257. Ravelosona, D. *et al.* Domain Wall Creation in Nanostructures Driven by a Spin-Polarized Current. *Physical Review Letters* **96,** 186604 (May 10, 2006).

258. Akers, S. B. *Synthesis of combinational logic using three-input majority gates* in *3rd Annual Symposium on Switching Circuit Theory and Logical Design (SWCT 1962)* 3rd Annual Symposium on Switching Circuit Theory and Logical Design (SWCT 1962) (IEEE, Chicago, IL, USA, 1962), 149–158.

259. Kim, S. K. *et al.* Ferrimagnetic spintronics. *Nature Materials* **21,** 24–34 (Jan. 2022).

260. Kaiser, C. & Parkin, S. S. P. High negative tunneling magnetoresistance in magnetic tunnel junctions with a ferrimagnetic CoFeGd electrode and a CoFe interface layer. *Applied Physics Letters* **88,** 112511 (Mar. 13, 2006).

261. Tsunegi, S., Yakushiji, K., Fukushima, A., Yuasa, S. & Kubota, H. Microwave emission power exceeding 10 W in spin torque vortex oscillator. *Applied Physics Letters* **109,** 252402 (Dec. 19, 2016).

262. Tsunegi, S. *et al.* Spin torque diode effect of the magnetic tunnel junction with MnGa free layer. *Applied Physics Letters* **112,** 262408 (June 25, 2018).

263. Mizukami, S., Suzuki, K. Z. & Miura, Y. All-optical probe of sub-THz spin precession in a $L\,1_0$ MnGa nanolayer. *Applied Physics Express* **12,** 043003 (Apr. 1, 2019).

264. Maksym, P. A. & Beeby, J. L. A THEORY of RHEED. *Surface Science,* 423–438 (1981).

265. Hasegawa, S. *Characterization of Materials* (Wiley, Oct. 15, 2002).

266. Yasaka, M. X-ray thin lm measurement techniques, 9 (2010).

267. Bragg, W. H. & Bragg, W. L. The reflection of X-rays by crystals. *Proceedings of the Royal Society A* **88,** 11 (Jan. 7, 1913).

268. Foner, S. Versatile and Sensitive Vibrating Sample Magnetometer. *Review of Scientific Instruments* **30,** 548–557 (July 1959).

269. Fagaly, R. L. Superconducting quantum interference device instruments and applications. *Review of Scientific Instruments* **77,** 101101 (Oct. 2006).

270. Josephson, B. D. Coupled Superconductors. *Reviews of Modern Physics* **36,** 216–220 (Jan. 1, 1964).

271. Kerr, J. XLIII. *On rotation of the plane of polarization by reflection from the pole of a magnet. The London, Edinburgh, and Dublin Philosophical Magazine and Journal of Science* **3,** 321–343 (May 1877).

272. Nederpel, P. Q. J. & Martens, J. W. D. Magnetooptical ellipsometer. *Review of Scientific Instruments* **56,** 687–690 (May 1985).

273. Van der Pauw, L. A method of measuring the resistivity and Hall coefficient on lamellae of arbitrary shape. *Philips Technical Review* **20,** 220–224 (1958).

274. Van der Pauw, L. A Method of Measuring Specific Resistivity and Hall Effect of Discs of Arbitary Shapes. *Philips Res. Repts* **13,** 1–9 (Feb. 1958).

275. Okamoto, K. A new method for analysis of magnetic anisotropy in films using the spontaneous hall effect. *Journal of Magnetism and Magnetic Materials* **35,** 353–355 (Mar. 1983).

276. Nagaosa, N., Sinova, J., Onoda, S., MacDonald, A. H. & Ong, N. P. Anomalous Hall effect. *Reviews of Modern Physics* **82,** 1539–1592 (May 13, 2010).

277. You, C.-Y., Sung, I. M. & Joe, B.-K. Analytic expression for the temperature of the current-heated nanowire for the current-induced domain wall motion. *Applied Physics Letters* **89,** 222513 (Nov. 27, 2006).

278. Fangohr, H., Chernyshenko, D. S., Franchin, M., Fischbacher, T. & Meier, G. Joule heating in nanowires. *Physical Review B* **84,** 054437 (Aug. 11, 2011).

279. Jacob, K. & Rajitha, G. Thermodynamic properties of strontium titanates: Sr2TiO4, Sr3Ti2O7, Sr4Ti3O10, and SrTiO3. *The Journal of Chemical Thermodynamics* **43,** 51–57 (Jan. 2011).

280. Muta, H., Kurosaki, K. & Yamanaka, S. Thermoelectric properties of reduced and La-doped single-crystalline SrTiO3. *Journal of Alloys and Compounds* **392,** 306–309 (Apr. 2005).

281. Popuri, S. R. *et al.* Glass-like thermal conductivity in $SrTiO_3$ thermoelectrics induced by A-site vacancies. *RSC Adv.* **4,** 33720–33723 (2014).

282. Martelli, V., Jiménez, J. L., Continentino, M., Baggio-Saitovitch, E. & Behnia, K. Thermal Transport and Phonon Hydrodynamics in Strontium Titanate. *Physical Review Letters* **120,** 125901 (Mar. 22, 2018).

Appendices

Chapter

Growth and Characterization Techniques

A

A.1 Growth

In this section, we will present the crystal growth of our thin films using MBE. More details about this growth process can be found in references[117, 122].

A.1.1 MBE growth of Mn_4N and $Mn_{4-x}Ni_xN$ thin films

The schematic of the MBE system used for the growth is shown in Fig.A.1. The MBE system is divided into two chambers, the load lock chamber and the growth chamber. These chambers are equipped with ultra high vacuum pumps: rotary pumps, an ion pump and a turbo molecular pump. The growth chamber includes a Reflection High Energy Electron Diffraction (RHEED) system, 3 Knudsen cells (K-cells) for the deposit of Mn, Ni and other metal, a sputtering source for capping layers such as SiO_2 or Ta, a RF-plasma gun with gas lines of N_2 and Ar. The base pressure in the growth chamber, of the order of 10^{-7} Pa, which is monitored by a nude ion gauge and an inverted magnetron gauge. The growth procedure is also shown in Fig. A.1.

A.1.2 Substrates preparation

Two kinds of substrates have been used for this work, MgO(001) and $SrTiO_3$(001) which were bought from Furuuchi Chemicals, Japan. The dimensions of the substrates were 10×10×0.3 mm. The substrates were cleaned with acetone and methanol in an ultrasonic bath. The $SrTiO_3$ substrates were also cleaned in de-ionized H_2O after cleaning with acetone and methanol, however the MgO substrates were not cleaned with water to prevent damaging them. The MgO substrates were also annealed in the growth chamber before the growth at 600°C, to remove any remaining organic impurities and also to improve the surface sites. $SrTiO_3$ substrates were also subjected to an acid treatment, to etch the top layer in order to obtain a Ti-terminated surface. A buffer HF solution with a composition of 5% HF and 35%NH_4F in weight ratio was used for the etching. Some of the $SrTiO_3$ substrates were also annealed for 30 minutes at 300°C in the growth chamber before the growth.

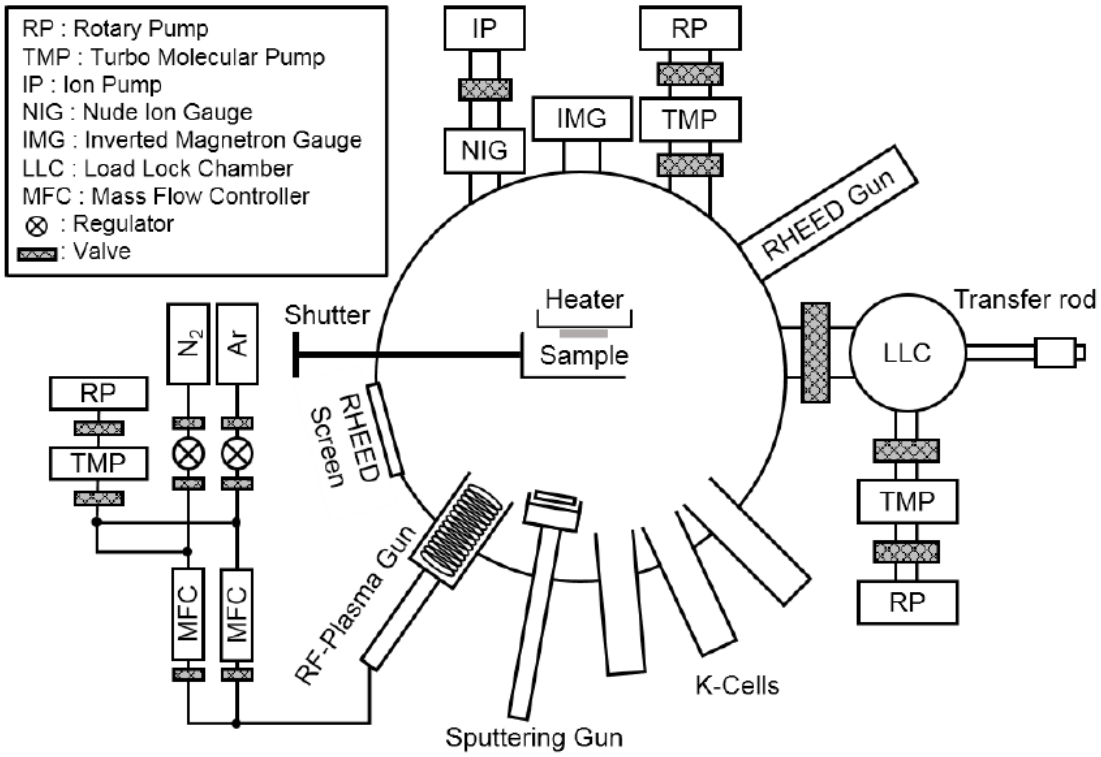

Figure A.1: *Schematic of the Molecular Beam Epitaxy set-up*

A.1.3 Deposition techniques

3 growth parameters are optimised before the deposition process: the nitrogen-flow condition, the Mn and Ni deposition rates and the substrate temperature T_s. The electrically neutral atoms of Nitrogen were supplied through the supply line into the chamber, where the RF plasma gun excites the Nitrogen into a N_2 plasma. The pressure and mass flow was optimized to 0.1 MPa and 1 sccm using the regulator and mass flow controller, respectively. An ion trapper set at 300 V is used to remove both the cations and anions, and the intensity of light emission in an optical spectrometer is used to monitor the magnitude of the plasma in the chamber. The RF input power, gas pressure at the nude ion gauge and the intensity of the light emission at 336 nm wavelength are usually set at 105 W, 4.5 mPa and 2.3×10^3 counts per 3 ms, respectively.

The second set of parameters consists in the deposition rates of Mn and Ni, which are controlled by the heating of the K-cells. To measure these rates, both Mn and Ni are grown in a first step on Si substrates, after which their thickness is measured using XRR measurements. For Mn, the cell temperature was kept around 835°C, which corresponds to a Mn rate of deposition between 1 - 1.3 nm per minute. The temperature of the Ni cell was varied depending on the chosen Ni concentration, starting from 1090°C for a Ni concentration of x = 0.05 to 1209°C for a Ni concentration of x = 0.3. The third parameter, the substrate temperature, was maintained at 450°C for all the samples, this growth temperature allows the diffusion of the nitrogen into the lattice and the ordering of the crystal structure. In order to have an efficient heating of the substrate, the substrates were kept on top of a Molybdenum sheet.

After the growth of the magnetic thin films, they were capped with SiO_2 in-situ to prevent oxidation. During the sputtering, Ar gas coming from a parallel gas line is let into the growth chamber with a pressure of 0.095 Pa, monitored by an inverted magnetron gauge. The sput-

tering gun excites the Ar^+ plasma and sputters the target source to deposit SiO_2 on top of the grown layer.

A.2 Crystallographic Characterization Techniques

In this section, we will introduce the RHEED and XRD techniques which were used for the crystallographic characterizations.

A.2.1 Reflection High Energy Electron Diffraction

In order to characterize the crystalline structure of the thin films in situ, a RHEED equipment[264] is used inside the growth chamber of the MBE setup shown in Fig. A.1. It is based on an electron beam of 10-100 kV to obtain an ultrashort wavelength and thus a high resolution. This electron beam is directed towards the sample surface with a grazing incident angle of 0.2-0.3°, which is used to obtain a forward scattered diffraction patterns on a screen. The focus, brightness and the contrast of the diffraction pattern are optimized by tuning the x-y direction of the electron beam. The RHEED pattern and its shapes depend on the orientation of the crystalline structure, of the quality of the crystalline structure and on the surface flatness. RHEED patterns obtained in this work were taken by setting the accelerating voltage of the electron beam at 20 kV. The electron beam is placed both along the $SrTiO_3$[100] and $SrTiO_3$[111] direction by rotating the sample inside the growth chamber.

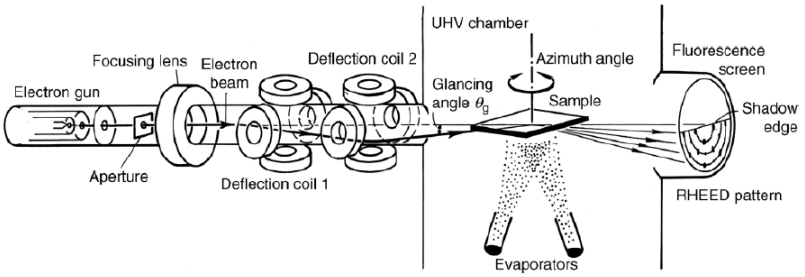

Figure A.2: *Schematic of the RHEED. Taken from Ref.[265]*

A.2.2 X-Ray Diffractometry

A Rigaku SmartLab setup has been used for the characterization of the samples used in this thesis[266]. The incident X-rays are diffracted by the different layers of the crystalline structure, in different directions that can be understood by considering Bragg's law[267].

$$2d_{hkl}sin\theta = n\lambda \tag{A.1}$$

where d_{hkl} is the distance between the each hkl plane in the crystal, θ is the incident angle of the X-rays, n is the diffraction order, and λ is the wavelength of the incoming X-rays. In this work, n-th diffraction peaks from the plane crystal(hkl) are denoted as crystal $nh\ nk\ nl$, independently of the name of the plane. For example, the second diffraction peak from Mn_4N(001) phase is denoted as "Mn_4N 002". By changing the relative angle between the substrate and the X-ray detector, different orientation axis can be selected, such as the perpendicular to plane ($2\theta/\omega$) and the in-plane ($2\theta_\psi/\phi$) axis. Mn_4N[001], [100] and [110] axis were usually chosen as they correspond to the fundamental crystalline orientations. From these

measurements, the diffraction peaks, the crystalline quality and crystal type are identified. To evaluate the orientation quality of the epitaxial films, ω rocking curve measurements were also performed. By scanning the ω angle by tilting the sample at a fixed 2θ (corresponding to diffraction peak such as Mn_4N 002), the distribution of the crystalline orientations can be qualitatively evaluated.

A.3 Magnetic Characterization Techniques

In this section, we will describe the main magnetization characterization used in this thesis: VSM, SQUID and MOKE microscopy.

A.3.1 Vibrating Sample Magnetometer

A VSM setup has been used to measure quantitatively the magnetic properties of the samples, such as their hysteresis curves and their saturation magnetizations[268]. In this setup, the magnetic field is swept in both the out-of-plane and in-plane orientations using an electromagnet. The external magnetic field changes the orientation of the magnetization of the sample based on the direction of the applied field. The sample is placed in a quartz sample holder, which is kept in the electromagnet. The sample holder is connected to a piezoelectric transducer, which converts a sinusoidal electrical signal into sinusoidal motion, thereby inducing a vibration of the sample holder. The working principle of VSM is based on Faraday's law of induction, where an electromotive force is generated whenever there is a change in the magnetic flux in a coil. Here, as the sample vibrates, it induces a change of flux and thus an e.m.f. in nearby pick up coils. The voltages generated are captured using lock-in techniques. The induced e.m.f. is directly proportional to the saturation magnetization of the sample. It is then converted into magnetization values, a Ni sample is generally used as a reference for calibration.

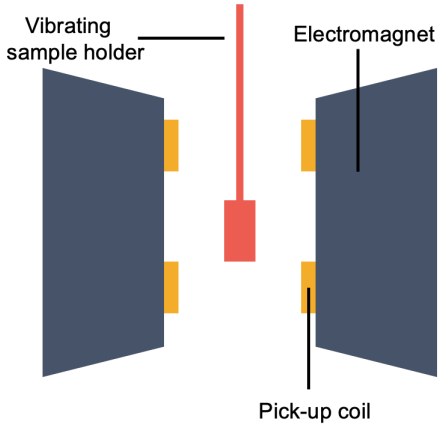

Figure A.3: *Schematic of the VSM setup.*

A.3.2 Superconducting Quantum Interference Device

In a SQUID setup, the Josephson effect of superconductors is used to measure the magnetic properties of the sample[269]. The Josephson effect is observed in superconductor/insulator/superconductor junctions, also known as Josephson junctions. It was predicted by Josephson in 1962 that not only electrons but also cooper pairs can tunnel through the insulating junction[270]. The superconductors are separated by an insulating layer so that they have a "weak

link". For thicknesses around 2 nm, which are shorter than the coherence length of the superconductors, and current lower than a critical current I_c (which depends on the weak link), these Cooper pairs can tunnel through the insulating layer without any voltage drop. This leads to a current called the Josephson current, and a circuit containing one or more Josephson junctions is very sensitive to the magnetic flux.

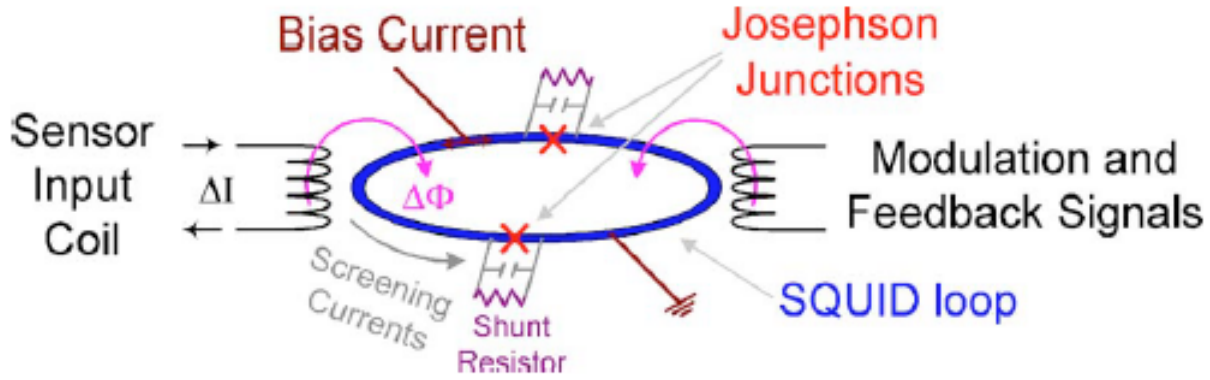

Figure A.4: *Illustration of the Josephson junction and SQUID working principle. Taken from Ref.[269]*

Such a circuit can be made like a ring, with two Josephson junctions as shown in the figureA.4 to form a SQUID. This system can be used to sense very small magnetic fields. By applying a bias current I_b larger than I_c, a voltage drop across the loop I_{loop} can be detected. When the sample is placed in the ring, its magnetic field penetrates the ring, resulting in a screening current due to the Meissner effect, which tries to cancel the magnetic flux. The current in the loop changes ($I_{loop} = \Phi_{loop}/L_{loop}$), thereby enabling to measure the strength of the magnetic field. Using this technique, very small magnetic field can be detected. Therefore, the SQUID setup is perfectly suitable to measure ferrimagnetic samples with a small magnetization, especially close to the compensation point.

A.3.3 Magneto-optic Kerr Effect microscopy

The Kerr effect was discovered in 1877[271]. This effect is used here to image the magnetic domain structures. When a linearly polarized light is pointed towards a magnetic surface, the reflected light is transformed in an elliptically polarized light. This rotation is of the polarization of light is known as the Kerr rotation, and it depends on the direction of the magnetization of the film[272]. Hence, this technique can be utilized to detect the changes in the magnetization direction and obtain a hysteresis loop, or to obtain the 2D-domain configuration using optical microscopy techniques. Depending on the relative direction of the magnetization with respect to the incident light, we can distinguish between 3 types of configurations, which are shown in the figure below.

The polar MOKE is generally used for perpendicularly magnetized films, while the longitudinal and transverse MOKE are used for films with in-plane magnetization. The resolution of the microscope is limited by the light wavelength (630 nm in our equipment) and has been estimated to be around 500 nm. By using different objectives, the field of view can be changed from several millimeters down to around 100 µm. Hence, this effect can then be used to image large domains, or smaller stripe patterns, and it is widely used for domain wall motion measurements.

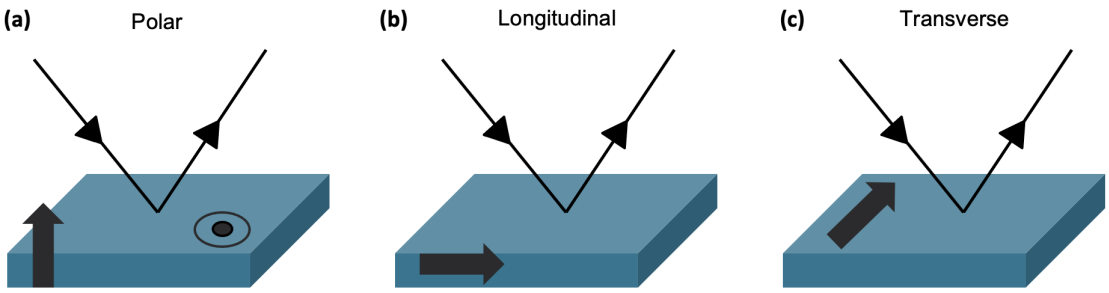

Figure A.5: *Three types of MOKE configurations*

A.3.4 Physical Property Measurement System

A PPMS is a setup which is used to measure the magnetic and electrical transport properties of magnetic materials. The PPMS setup used in this work is a commercial setup from Quantum Design. The maximum magnetic field which can obtained is ± 9 T, using a superconducting magnet. The sample temperature could be varied from 1.8 K to 400 K. This system is equipped with internal lockin-in amplifiers to perform resistivity measurements.

A.3.5 Anomalous Hall Effect

Magnetotransport measurements using AHE have been used in this thesis to obtain an accurate switching of the magnetization for the different rare-earth free ferrimagnetic nitrides. The resistivity (ρ_{xx}) and the AHE resitivtity (ρ_{xy}) have been obtained using both Van der pauw method[273, 274] and also from patterned hall crosses using nanofabrication (cf. Appendix B).

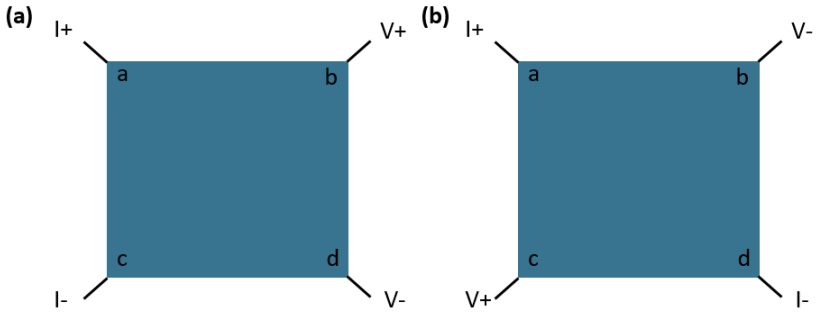

Figure A.6: *Van der pauw configurations for (a) Resistivity measurements (b) AHE measurements*

Fig.A.6 shows the Van der Pauw configurations for A.6 (a) resistivity and (b) transverse AHE measurements. The four corners of the thin films are connected in the circuit by wire-bonding. For the resistivity measurements, a current is injected into the thin films from point **a** to **b** as shown in Fig.A.6 (a). while the voltage is measured from point **c** to **d**. The resistance is calculated using taking the ratio of the V_{cd} and the current I_{ab} which is defined as $R_{ab,cd} = Vcd/I_{ab}$. The other contacts combination $R_{ac,bd}$ is also measured to account for the asymmetries. To extract the resistivity (ρ_{xx}) from the measured resistances, the following relationship is used in the case of a roughly square sample.

$$e^{(-\pi t R_{ab,cd}/\rho_{xx})} + e^{(-\pi t R_{ac,bd}/\rho_{xx})} = 1 \tag{A.2}$$

Here, t is the thickness of the thin film. The circuit for the Hall configuration is shown in Fig.A.6(b) in the case of Van der pauw and in Fig.A.7 for Hall cross. For Van der pauw setup, a current is applied diagonally from one to the end of the sample while the voltage is measured on the other diagonal points in the presence of external magnetic field. Fig.A.7 shows the hall cross of measurement configuration where the magnetization M interacts with the external magnetic field B and changes the direction of the magnetization.

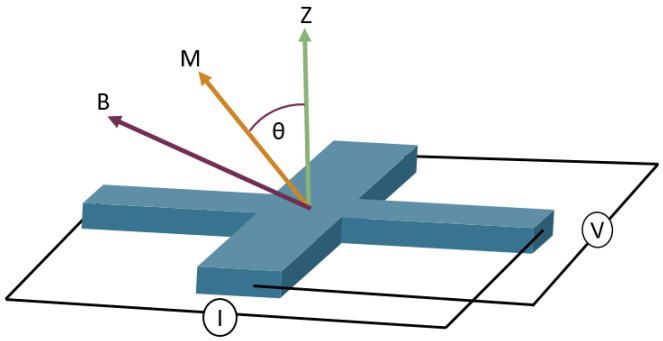

Figure A.7: *Illustration of a Hall cross showing the interaction of the external field (B) with the magnetization of the thin film (M). The current is applied along the bar while the transverse voltage is measured in the arms.*

The transverse voltage in the case of Mn_4N mainly depends on the Hall effect[275] and the AHE[276]. The transverse voltage is then given as

$$V_{xy} = (R_0 + R_H \frac{B_z}{t} + R_{AHE0} cos\theta) I_x \tag{A.3}$$

Where, R_0 is the longitudinal resistive offset, R_H is the hall coefficient and R_{AHE0} is the coefficient of AHE. The AHE has a $cos\theta$ dependence with the highest AHE value when the magnetization is perpendicular to the sample surface and and lowest when the magnetization is in-plane of the sample surface. The second term of the equation is coming from the ordinary hall effect which is proportional to the external magnetic field. However in the case of metals like Mn_4N, the ordinary hall effect is very low due to high carrier density. This contribution has to be subtracted from the signal but in the case of Mn_4N, it was found to be negligible as compared to the high AHE.

Chapter

B

Nanofabrication

In order to study domain wall motion in the studied thin films, and to perform magneto-transport measurements, it is necessary to pattern the films into micro and nanostructures. In this section, we will sum up the techniques and procedure for the fabrication of such devices.

B.1 Electron beam lithography

E-beam lithography is one of the most useful techniques in nanofabrication, with a resolution possibly as low as ten of nanometers. A thin layer of electron sensitive resist is deposited on top of the thin films. An electron beam of particular energy and current is then scanned on top of the resist. This leads to a change in the solubility of the resist. The pattern is then developed using a developer solvent. Depending on the type of resist used, the part where the e-beam has been exposed either becomes more soluble (positive resist) to the developer or become harder (negative resist). For the development of the microwires and hall bars used in this thesis, a positive resist of PMMA is spin-coated onto the sample at 4000 rpm for 60s, followed by baking at 180°C for 5 minutes. The electron beam insolation is then performed using a Jeol 6300 FS e-beam nano-writer which works at a acceleration voltage of 100 keV. The developer solvent of MIBK:IPA with a 1:3 ratio is used to remove the resist from exposed areas. A layer of Al around 30 nm is then deposited on top of the sample. It is then followed by removal of the resist by lift-off process in acetone overnight. After this process, a 30 nm layer is left on top of thin film with the shape of the devices.

B.2 Ion Beam Etching

Ion beam etching (or ion milling) is a physical etching process, in which an excited Ar^+ plasma is created in the etching chamber and accelerated towards the sample using a bias voltage. This creates a bombardment of the Ar ions onto the sample surface, thereby removing the atoms from the thin film surface. It decreases the thin film thickness gradually. The etching process often leaves a wall of material at the edge of the fabricated structure. Therefore, during the etching process, the sample is usually tilted and then rotated to achieve an uniform etching. The ion beam etching machine used here also has a secondary ion mass spectrometer(SIMS)

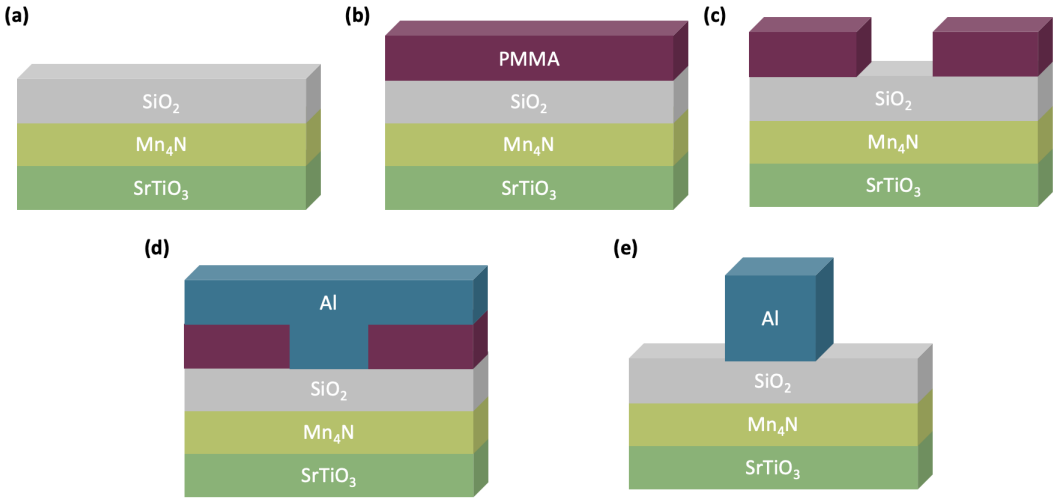

Figure B.1: *Schematic of the E-beam lithography process. (a) Mn_4N thin film capped with SiO_2 (b) Positive resist PMMA spin coated and baked at 180° for 5 minutes (c) E-Beam lithography after development (d) Deposition of Al as the hard mask. (e) Removal of the PMMA resist using a lift-off process.*

in-situ, in order to monitor the etching. After this process, the magnetic film only remained under the Al layer, which acts a protective layer.

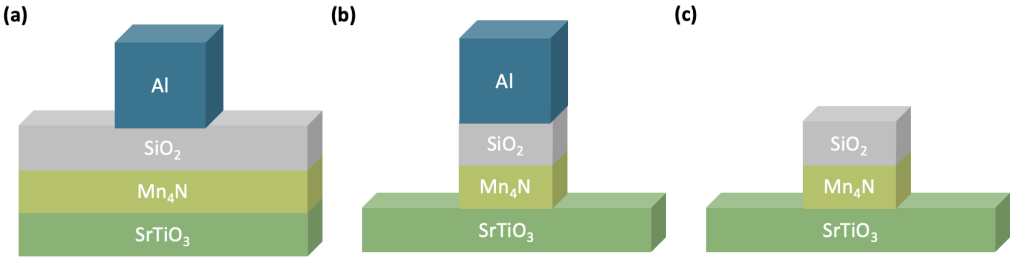

Figure B.2: *Schematic of the etching process. (a) Mn_4N thin film capped with SiO_2 with Al hard mask on top (b) Removal of the Mn_4N layer after the etching process with Mn_4N layer only under the Al (c) Removal of the Al hard mask*

B.3 Optical Lithography

After the ion beam etching, the Al is then removed from the top of the devices using a diluted solution of Tetramethylammonium Hydroxide which reacts only to the Al layer. After this, we are only left with the central part of the devices, made of Mn_4N with the SiO_2 capping. To connect the device electrically, gold pads are then made on top of the devices, using optical lithography. A positive resist (AZ5214) is spin coated on the sample at 4000 rpm for 60s, and baked for 90s at 100°C. A pre-made mask is placed between the UV light of a MJB4 UV photolithography tool and the sample. After UV exposure during 30s, the sample is developed in an AZ developer solution, to remove the exposed part of the resist. After this step, the contact pads are deposited by evaporation, usually of around 60 nm of Titanium and Gold. The metal is deposited on the whole sample, and followed by a lift-off in acetone overnight. After this step, the contact metal is only left on the part where the UV light was exposed to.

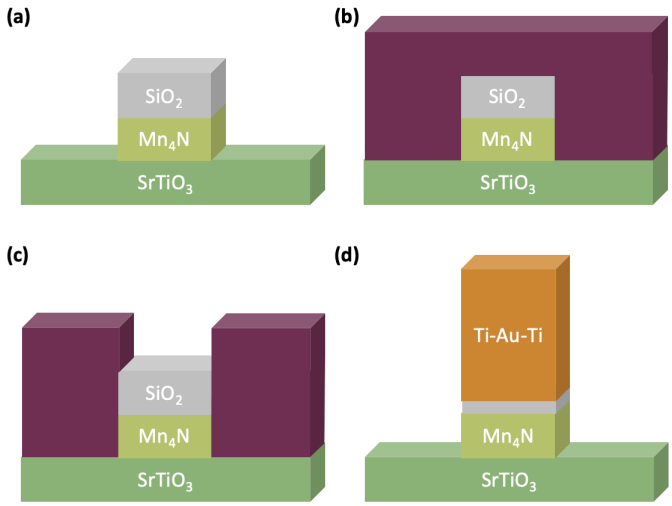

Figure B.3: *Schematic of the optical lithography process. (a) Mn_4N devices capped with SiO_2 (b) Spin coating of positive resist (c) Exposure of UV light and development (d) Deposition of the Ti-Au-Ti contacts and lift off process to remove the resist.*

Chapter

C

Analytical modeling of Joule Heating in Nanowires

In this section, we will model the Joule heating effect in the nanowires by applying current pulses. The purpose of this study is to have an idea about the temperature of the nanowires and whether they reach the Curie temperature with the current density and pulse widths we have used in our experiments. We have used a simple analytical expression given by You et al.[277, 278]. This model takes into account that the nanowire is being heated by the current pulses, and the heat is then dissipated by the substrate. The calculations are made using the following assumptions i) The length L of the wire is infinite with respect to its thickness. ii) The temperature of the wire is uniform throughout the wire. iii) Seen from the substrate, the heat source is at the surface with the nanowire (z=0), as shown in Fig. C.1, and the heat can only flow through the substrate. iv) the temperature of the wire is homogeneous, and equal to that of the interface.

The Joule heating for a current density J is given as $= RI^2 = \mathrm{L}(whJ)^2/\sigma_W \mathrm{wh} = \mathrm{L(wh)}J^2/\sigma_W$. Here, σ_W, w and h are the electrical conductivity, width and height of the nanowire. Considering the previously mentioned assumptions, the overall temperature profile can be given as :-

$$T(t) = \frac{whJ^2}{\pi\mu_s\sigma_W\rho_S C_S}\left(arcsinh\left(\frac{2\sqrt{\mu_S t}}{w_G}\right) - \theta(t-t_P)arcsinh\left(\frac{2\sqrt{\mu_S(t-t_P)}}{w_G}\right)\right) \tag{C.1}$$

Here, μ_S is the diffusivity of the substrate given as $\mu_S = K_S/\rho_S$ with K_S the thermal conductivity and ρ_S the density of the substrate. t is the time, t_P is the pulse width, C_S is the specific heat capacity of the substrate and w_G is the Gaussian width of the nanowire. The width of the nanowire has been reduced to the Gaussian width as shown in Fig.C.1 (c). The reason for the use of the Gaussian profile is the ease of calculation. $w_G = \alpha w$, here w is the width of the nanowire while α is an adjustable parameter. The α parameter is estimated to be ~ 0.5 when the t $\ll w/\mu_S$ [277]. Now, if we take $t = t_P$, we can further reduce the equation down to:

$$T(t) = \frac{whJ^2}{\pi\mu_s\sigma_W\rho_S C_S}\left(arcsinh\left(\frac{2\sqrt{\mu_S t}}{w_G}\right)\right) \tag{C.2}$$

Here, we will use the above equation to calculate the Joule heating effect and compare

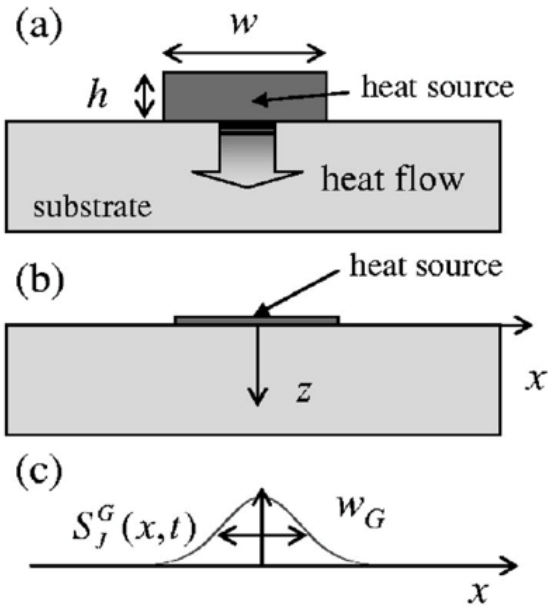

Figure C.1: *(a) Illustration of the nanowires showing the nanowire on top of the substrate, w being the width and h the height of the nanowire. The nanowire is treated as the heat source, the heat flowing towards the substrate. (b) Illustration showing the approximate scale of the thin film with the substrate (c) Power density Gaussian profile of the nanowire. Figure taken from You et al.[277]*

$Mn_4N/SrTiO_3$ and $Mn_{4-x}Ni_xN/SrTiO_3$ systems. For these calculations, the properties of $SrTiO_3$ were taken as (Specific heat capacity) C_S = 536.31 J/K kg at 300 K[279], (Density) ρ_S = 5120 kg/m^3 and (Thermal Conductivity) K_S = 11 W/mK at 300 K[280–282]. For Mn_4N, the resistivity is taken as 180 $\mu\Omega$cm (which is then converted into the conductivity)[86] and the width of the wire is taken as $w_G = \alpha\ w$ with $\alpha = 0.5$ and $w = 1\mu$m.

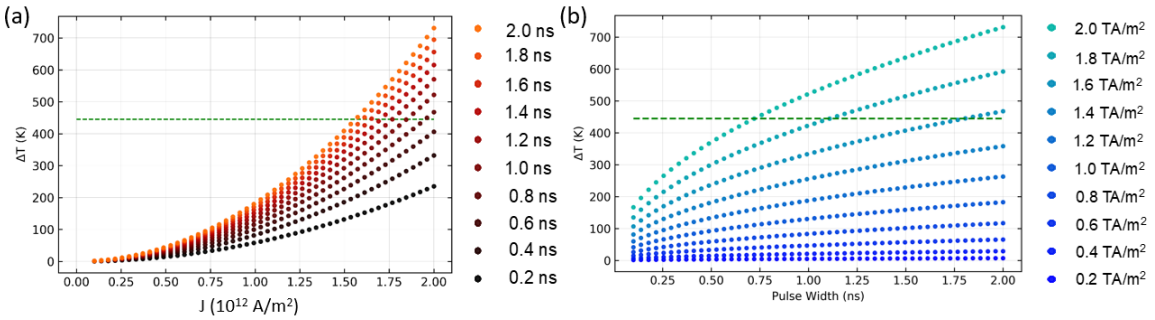

Figure C.2: *Mn_4N temperature variations (a) Change in temperature plotted against current density. Different curves indicate the current pulse widths (b) Change in temperature plotted against the current pulse width, the different curves indicating the different current densities. The green line represents the Curie temperature of Mn_4N.*

Fig.C.2 shows the variation of the temperature in $Mn_4N/SrTiO_3$ with Fig.C.2 (a) showing the change in temperature plotted against current density due to the Joule heating and subsequent heat flow into the $SrTiO_3$. The different coloured curves demonstrates different pulse width times from 0.2 ns to 2 ns. The green horizontal dotted line shows the Curie temperature of Mn_4N at 450 K. The 0 K here is taken as 300 K. In a similar way, Fig.C.2 (b) shows the change in temperature against the current pulse width with the curves showing the different

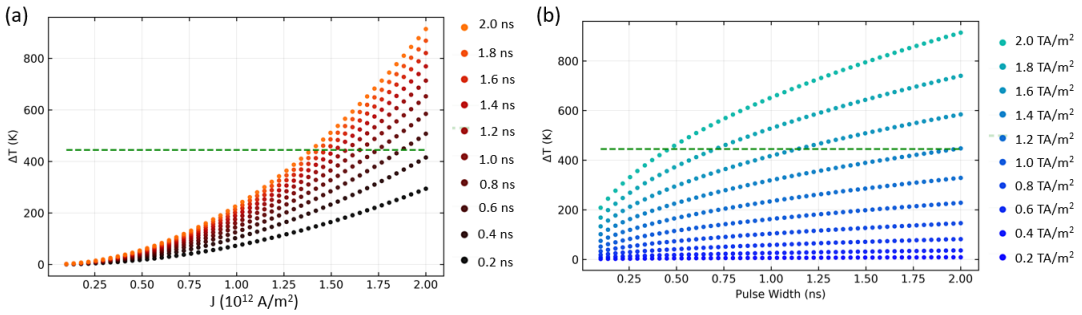

Figure C.3: *$Mn_{4-x}Ni_xN$ temperature variations (a) Change in temperature plotted against current density. Different curves indicate the current pulse widths (b) Change in temperature plotted against the current pulse width, the different curves indicating the different current densities. The green line represents the Curie temperature of Mn_4N.*

current densities from 0.2×10^{12} A/m^2 to 2×10^{12} A/m^2. The curves obtained here suggests that in our experiments of CIDWM in Mn_4N, the Joule heating of the nanowires does not reach the Curie temperature.

Fig. C.3 shows the temperature variations in $Mn_{4-x}Ni_xN$. For these calculations, we have taken the resistivity of $Mn_{3.85}Ni_{0.15}N$ thin film of 225 $\mu\Omega$cm while keeping the other parameters the same. As the resistivity increases with Ni substitution, the Joule heating increases as well. This in turn leads to reaching the Curie temperature with less current density and smaller pulse widths.

Overall, these calculations are in inline with our experimental results and suggests that heating of the nanowires does not reach the Curie temperature for the current densities and the pulse widths used in $Mn_{4-x}Ni_xN$ thin films as well. Even though we have not taken into account the convection effect, heat dissipation from the atmosphere and an increase in the resistivity due to Joule heating. Heat dissipation through the atmosphere should not be negligible and hence, our results maybe an overestimation. Also, considering that the resistivity increases with the heating, would result in less current to flow through the wire, which should in principle decrease the heating.

We have used these calculations for the estimation of the Joule Heating in the nanowires. However, we can also use these calculations to design new wires in order to reduce Joule Heating so that higher current density pulses could be applied to the wires to reach even higher DW velocities.

Fig.C.4 shows the temperature variations in Mn_4N and $Mn_{3.85}Ni_{0.15}N$ when the widths of the nanowires are varied with 1.5 ns pulse widths (a) and (c); current density of 1.5×10^{12} A/m^2 (b) and (d). For these calculations, only the width and the resistivity were varied while keeping all of the other parameters the same. A pulse width of 1.5 ns and a current density of 1.5×10^{12} A/m^2 were chosen as they are very high so we can estimate the heating for extreme conditions. These curves indicate that the heating in the case of Mn_4N is less than that of $Mn_{3.85}Ni_{0.15}N$ as the resistivity of Mn_4N is lower. The more important observation here is that the width of the wire does not play a key role in changing or reducing the heating effect. The heating changed only marginally when the width is decreased from 1 μm to 300 nm. Only at 100 nm, we observe a big change in the heating. Next, we will look into how the thickness of the wires affects the heating in Mn_4N and $Mn_{3.85}Ni_{0.15}N$.

Fig.C.5 shows the comparison of the thickness on the temperature profile with similar parameters as before, with $w = 1$ μm and $\alpha = 0.5$. From these graphs, we see big dependence of the temperature with the thickness. As the thickness decreases the Joule heating is hugely reduced for both Mn_4N and $Mn_{3.85}Ni_{0.15}N$ nanowires. From the study of Joule heating, we have

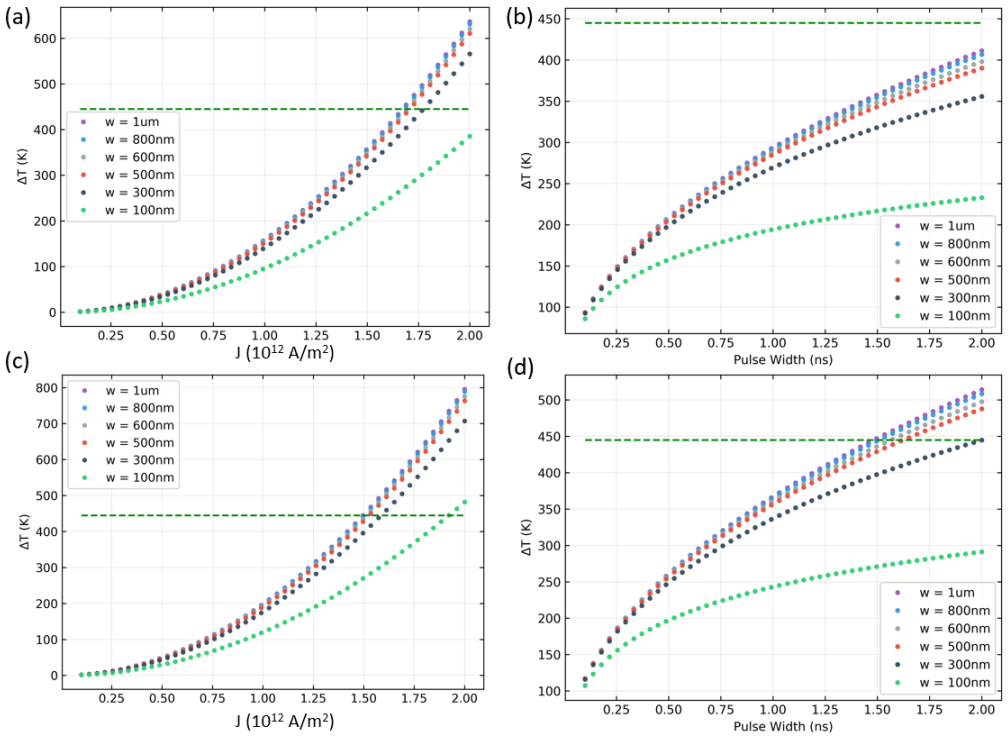

Figure C.4: *Comparison of width on the temperature profile; Current density against change in temperature with 1.5 ns pulse width for Mn_4N (a) and $Mn_{3.85}Ni_{0.15}N$ (c) Pulse width against change in temperature with 1.5 × 10^{12} A/m^2 current density for Mn_4N. (b) and $Mn_{3.85}Ni_{0.15}N$ (d). The green line represents Curie temperature of Mn_4N.*

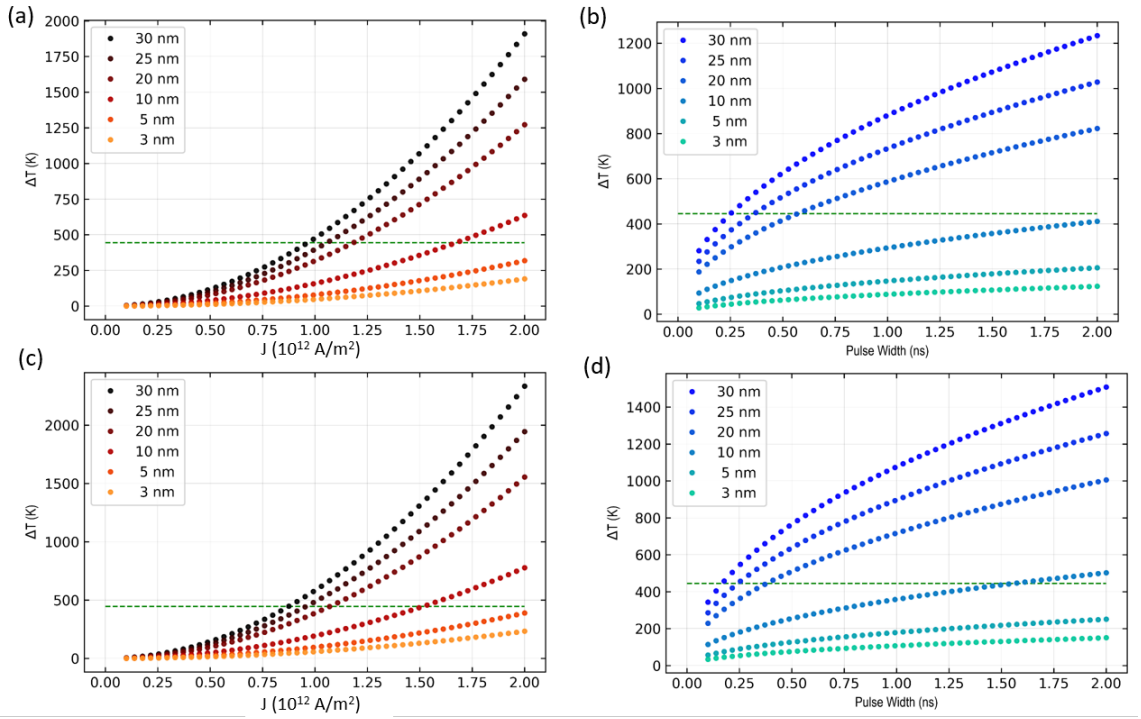

Figure C.5: *Temperature variation as a function of the thickness; Change in temperature plotted against current density with 1.5 ns pulse width for Mn_4N (a) and $Mn_{3.85}Ni_{0.15}N$ (c) Change in temperature plotted against pulse width with 1.5 × 10^{12} A/m^2 current density for Mn_4N. (b) and $Mn_{3.85}Ni_{0.15}N$ (d). The green line represents the Curie temperature of Mn_4N.*

shown that the heating does not exceed the Curie temperature while being in the experimental parameters. It has also shown ways to reduce the heating effect in these systems with varying the thickness of thin films. Therefore, in order to increase the current density to reach an even high domain wall velocities, the thickness of the thin films could be reduced. Another way to achieve the same is to decrease the width of the nanowires to 100 nm. However it would also make it very difficult to observe the domains using MOKE microscopy.

Summary

The boundaries between magnetic domains are known as domain walls. The motion of these domain walls using magnetic fields or spin polarized currents has been one of the main focus of spintronics research in the last two decades. One mechanism leading to current induced domain wall motion is the spin transfer torque, where the spin polarized current is generated within the ferromagnetic layer and exerts a torque on the local magnetic moments of the domain walls. The other mechanism is the spin orbit torque, which is now widely used for the domain wall motion experiments, and where the spin polarized current is generated by an adjacent heavy metal layer.

Recently, current-induced magnetization dynamics in ferrimagnets has become an active field of research. The magnetic and/or the angular momentum compensation can be achieved by either changing the temperature or by changing the composition of the materials. As the magnetization or the angular momentum that has to be reversed is small close to these points, previous reports on ferrimagnets have evidenced large domain wall velocities under action of spin orbit torques. In this manuscript we will focus on current-driven domain wall dynamics in an epitaxial rare-earth free ferrimagnetic nitride, Manganese Nitride (Mn4N), using spin transfer torques.

We show that epitaxially grown Mn_4N thin films grown on $SrTiO_3$ substrate have a very low magnetization and mm-scale domains with very low pinning. On this system, domain wall motion was studied by fabricating nanowires by standard e-beam lithography. Using magneto optic kerr measurements, we measured a high domain wall velocity of more than 900 m/s in Mn_4N at $J = 1.3 \times 10^{12}$ A/m^2, at room temperature, with only spin transfer torque.

In order to reach the compensation point, different samples were grown epitaxially while increasing the doping Ni concentration. X-ray magnetic circular dichroism measurements showed that the Ni atoms preferentially occupy the site of Mn(I). Since the magnetic moment carried by the Ni atoms is anti-parallel to that of Mn(I), increasing the Ni content decreases the net magnetic moment. Beyond a critical Ni concentration, the net magnetization is then expected to be reversed. Using the values from neutron diffraction measurements, the expected magnetic compensation point lies around Ni atomic concentration of x = 0.18 which corresponds to 3.6% of Ni. The presence of the magnetic compensation point around this concentration is confirmed by x-ray magnetic circular dichroism and Anomalous Hall effect measurements.
The domain wall velocity is found to increase as the Ni concentration gets closer to the angular momentum compensation point, with a velocity up to 2000 m/s before the compensation point and approaching 3000 m/s after crossing the compensation point. Interestingly it was also observed that the domain wall motion direction is reversed beyond the compensation point. In order to explain these results, we used the q–ϕ model, expanded to a ferrimagnetic system consisting of two sub-lattices, and using effective magnetic parameters for the two sub-lattices. If one assumes that the spin polarization does not change after the angular momentum compensation point, the domain wall motion reversal is therefore due to a relative change of orientation of the net spin polarization with respect to global magnetization.

To confirm the validity of these assumptions, ab-initio calculations were performed, showing that the net magnetization is reversed at the Ni concentration x = 0.15, which match well with our experimental results. The simulations confirms that the conduction occurs through the Mn(II), and that the spin polarization remains in the same direction(Mn(I)) while the net magnetization direction is reversed.
The studied materials, composed of abundant elements, and free of critical elements such as rare-earths and heavy metals, are thus promising candidates for sustainable spintronics applications. These results underline that despite the spintronics community has been focusing mostly on SOTs in the past decade, the STT remains an efficient way to drive domain walls.

Résumé

Les frontières entre les domaines magnétiques sont appelées parois de domaine. Le mouvement de ces parois à l'aide de champs magnétiques ou de courants polarisés en spin a été l'un des principaux axes de recherche en spintronique des deux dernières décennies. Un mécanisme conduisant au mouvement de paroi sous courant est le couple de transfert de spin, où le courant polarisé en spin est généré dans la couche ferromagnétique. L'autre mécanisme est le couple spin-orbite, aujourd'hui largement utilisé, et où le courant polarisé en spin est généré par une couche adjacente de matériau spin-orbite.
Récemment, le contrôle de l'aimantation par injection de courant dans les matériaux ferrimagnétiques est devenu un important domaine de recherche. La compensation magnétique et/ou de moment cinétique peut être obtenue en modifiant la température ou en modifiant la composition des matériaux. Comme l'aimantation qui doit être renversée est faible près de ces points, des études récentes ont mis en évidence de grandes vitesses de paroi de domaine sous l'action de couples spin-orbite. Dans ce manuscrit, nous traitons de la propagation des parois de domaine sous l'effet d'un couple de transfert de spin dans un nitrure ferrimagnétique épitaxié, le nitrure de manganèse (Mn_4N).
Nous montrons que les couches minces de Mn_4N développées par épitaxie sur un substrat de SrTiO3 ont une très faible aimantation, et des domaines à l'échelle millimétrique avec un ancrage très faible. Dans ce système, le mouvement des parois de domaine a été étudié en fabriquant des nanofils par lithographie. En utilisant des mesures d'effet Kerr magnéto-optiques, nous avons mesuré des vitesses de paroi de plus de 900 m/s dans Mn_4N à $J = 1.3 \times 10^{12}$ A/m^2, à température ambiante, et avec seulement un couple de transfert de spin.
Afin d'atteindre le point de compensation, différents échantillons ont été épitaxiés en les dopant par du Ni. Des mesures de dichroïsme circulaire magnétique aux rayons X ont montré que les atomes de Ni occupent préférentiellement le site de Mn(I). Puisque le moment magnétique porté par les atomes de Ni est anti-parallèle à celui de Mn(I), l'augmentation de la teneur en Ni diminue le moment magnétique net. Au-delà d'une concentration critique en Ni, l'aimantation nette devrait alors s'inverser. En utilisant les valeurs des mesures de diffraction des neutrons, le point de compensation magnétique attendu se situe autour de 3.6 % de Ni. La présence du point de compensation magnétique autour de cette concentration est confirmée par des mesures de dichroïsme circulaire magnétique aux rayons X et d'effet Hall anormal.
Les vitesses de la paroi augmentent à mesure que la concentration de Ni se rapproche du point de compensation, avec une vitesse allant jusqu'à 2000 m/s avant le point de

compensation et approchant 3000 m/s après avoir traversé le point de compensation. Nous avons également observé une inversion de la direction du mouvement de la paroi au-delà du point de compensation. Afin d'expliquer ces résultats, nous avons utilisé le modèle q – ϕ. Si l'on suppose que la polarisation de spin ne change pas après le point de compensation du moment cinétique, l'inversion du mouvement de la paroi du domaine est due à un changement relatif d'orientation de la polarisation de spin nette par rapport à l'aimantation globale.

Pour confirmer la validité de ces hypothèses, des calculs ab-initio ont été effectués, montrant que l'aimantation nette est inversée à la concentration de Ni x = 0.15, ce qui correspond bien à nos

résultats expérimentaux. Les simulations confirment que la conduction se produit à travers le Mn(II), et qu'à la transition la polarisation du spin reste dans la même direction (Mn(I)) alors que la direction de l'aimantation nette est inversée.

Les matériaux étudiés, composés d'éléments abondants, et exempts d'éléments critiques comme les terres rares et les métaux lourds, sont ainsi des candidats prometteurs pour des applications de spintronique durable.

Bien que la communauté de la spintronique se soit principalement concentrée sur les SOT au cours de la dernière décennie, ces résultats soulignent que le STT reste un moyen efficace de contrôle des parois.